

This is to certify that the

dissertation entitled

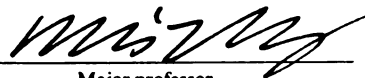
**MATHEMATICAL MODELING AND NUMERICAL
SIMULATIONS OF AUTOMOTIVE CATALYTIC
CONVERTERS**

presented by

Figen Lacin

has been accepted towards fulfillment
of the requirements for

Ph.D. degree in Mechanical Engineering



Major professor

Date Dec. 6, 2002

LIBRARY
Michigan State
University

PLACE IN RETURN BOX to remove this checkout from your record.
TO AVOID FINES return on or before date due.
MAY BE RECALLED with earlier due date if requested.

DATE DUE	DATE DUE	DATE DUE

**MATHEMATICAL MODELING AND NUMERICAL SIMULATIONS OF
AUTOMOTIVE CATALYTIC CONVERTERS**

By

Figen Lacin

A DISSERTATION

**Submitted to
Michigan State University
in partial fulfillment of the requirements
for the degree of**

DOCTOR OF PHILOSOPHY

Department of Mechanical Engineering

2002

ABSTRACT

MATHEMATICAL MODELING AND NUMERICAL SIMULATIONS OF AUTOMOTIVE CATALYTIC CONVERTERS

By

Figen Lacin

The major undesirable chemical species that constitute the main exhaust emissions produced by spark ignition engines are hydrocarbons (*HC*), carbon monoxide (*CO*) and nitrogen oxides (*NOx*). The catalytic converter is one of the important devices for the control of emission from spark-ignition engines. Several concurrent physical processes such as convective heat transfer, gas phase chemical reactions, surface reactions, flow oscillations, water vapor condensation and diffusion mechanisms add to the system's complexity. Under cold-start conditions, the catalytic converter does not become fully active during the first two minutes of the operation, allowing a significant fraction of the overall pollutants to be emitted. In the present study, a one-dimensional mathematical model that physically represents a single channel of the honeycomb structure has been developed. The effects of the geometrical parameters are investigated for the cold start regime. A multi-dimensional model has been developed to study the effect of the converter insulation. The results of the computations suggest new material-dependent designs to improve the conversion efficiency of the device and the cold-start performance. Moreover, from our model calculations, we have observed that the monolith's temperature and therefore the light-off time are greatly affected by the noble-metal distribution over the honeycomb walls of

the monolith. We have demonstrated that the light-off time is significantly shortened, by approximately 35%, using a suitable step-function for the noble-metal distribution. Hence, the emissions of the exhaust gas are reduced without increasing the cost of noble-metal materials used in the converter. For a given converter geometry and an amount of noble metal, an optimum noble metal distribution is being investigated with the understanding that the optimum noble-metal distribution proposed has to be practical in the area of manufacturing. Since the main source of the exhaust emissions is during the warm-up period of converters from a cold-start, the reduction of emissions shown in our model calculations is quite substantial.

Dedicated to my father Ali Lacin

ACKNOWLEDGMENTS

I would like to acknowledge the Department of Mechanical Engineering and the Center to Sensor Materials (a NSF Materials Research Science and Engineering Center) at Michigan State University for their financial support during my graduate education.

I would like to express my thanks to the members of my committee: Dr. Somerton, Dr. Petty, Dr. Shi and Dr. Zhou for their efforts in bringing my Ph.D dissertation to completion. I would like to thank my advisor Dr. Mei Zhuang, who is a good friend as well as a wonderful mentor to me. Her loving and balancing support was with me during all stages of my PhD study, helping me continue even at times when it seemed impossible to finish.

I am very grateful to Dr. M.S. Kavsaoglu, my M.Sc. advisor at Middle East Technical University at the Department of Aeronautical Engineering, without whom I would not see the possibility of studying abroad.

I want to thank my beloved husband, a friend and an excellent scientist Bulent Buyukbozkirli without whom it would be impossible to complete this dissertation. Bulent has been a source of love, encouragement and a challenging guide.

The prayers of the elders of my family, of my mother Fatma, and her unconditional love, were with me all the time. I feel very lucky and I am grateful to their presence.

TABLE OF CONTENTS

LIST OF TABLES	ix
LIST OF FIGURES	x
NOMENCLATURE.....	xiv

Chapter 1

INTRODUCTION.....	1
1.1 Problem Definition and Objective of the Study	1
1.2 Outline of the Present Study	4
1.3 Literature Survey	6

Chapter 2

PHYSICAL MODEL.....	18
2.1 Important Parameters for Catalytic Converters	18
2.1.1 Geometric Parameters.....	18
2.1.2 Chemical Kinetics Data.....	20
2.2 Single Channel Model	21
2.3 Multi Channel Model.....	22

Chapter 3

MATHEMATICAL MODEL.....	25
Equations and Boundary Conditions	25
3.1 Fundamental Equations for One-Dimensional Single Channel Model	25
3.1.1 Dimensionless Form of The Balance Equations	27

3.1.2	Initial and Boundary Conditions	31
3.2	Fundamental Equations for The Multi-Channel Model, 3D-Study.....	33
3.2.1	Dimensionless Form of Multi-Channel Model Equations.....	35
3.2.2	Initial and Boundary Conditions for Multi- Channel Model.....	37
Chapter 4		
	METHOD OF SOLUTION.....	41
4.1	One- Dimensional Model.....	42
4.2	Multi-Dimensional Model	45
Chapter 5		
	RESULTS AND DISCUSSION	49
5.1	Nominal Values of the Parameters.....	50
5.2	The Reference Case and Performance Criteria	51
5.3	Effect of Transient Terms in the Gas Phase Conservation Equations	54
5.3.1	Effect of the Transient Term in Energy Balance Equation for the Gas Phase.....	54
5.3.2	Effect of the Transient Term in Mass Balance Equation for the Gas Phase.....	56
5.4	Effect of Geometrical Parameters	56
5.4.1	The Effect of Cell Density.....	57
5.4.2	The Effect of Wall Thickness.....	58
5.4.3	The Effect of Converter Length.....	60
5.5	The Effect of Noble Metal Distribution.....	61

5.5.1 Homogenous Noble Metal Distribution.....	62
5.5.2 Efficiency Analysis for Noble Metal Distribution	63
5.6 The Effect of Inflow Oscillations	70
5.7 Isothermal Study Results for Pressure Drop Calculations.....	71
5.8 Axisymmetric Model Analysis	73
 Chapter 6	
CONCLUSION	100
 APPENDIX A	
Chemistry Model	105
 APPENDIX B	
Balance equations.....	107
 BIBLIOGRAPHY.....	123

LIST OF TABLES

Table 4.1	Information flow diagram for calculation of each parameter, at a given time step n and spatial coordinate i	45
Table 4.2	Main flow-chart of the computations	48
Table 5.1	The numerical values of the parameters for <i>the reference case</i>	51
Table 5.2	Diffusivity coefficients for the exhaust gas species in cm^2 / s	51
Table 5.3	The values of the geometrical parameters and corresponding Reynolds numbers for different cell densities (constant wall thickness and void area.).....	57
Table 5.4	The values of the geometrical parameters for different cases, (constant void area and fraction.).....	59
Table 5.5	Three real-life driving cases.....	68
Table 5.6	Comparison of the <i>CO</i> -emissions of the reference case to the step-function noble metal distribution.	68
Table 5.7	Heat Transfer coefficients.....	75

LIST OF FIGURES

Figure 2.1	A simplified sketch of the catalytic converter substrate.....	20
Figure 2.2	Simple schematic of multi-dimensional model.....	24
Figure 5.1	The monolith temperature for various times. Solid line is taken from Oh <i>et al.</i> [1982].....	79
Figure 5.2	The CO-conversion efficiency for warm-up period. Solid line is taken from Oh <i>et al.</i> [1982].....	79
Figure 5.3	The CO-conversion for the reference case and the case with transient term.....	80
Figure 5.4	The gas temperature distribution along the monolith at 30 s.....	80
Figure 5.5	The surface temperature distribution along the monolith at 30 s.	81
Figure 5.6	The gas temperature distribution along the monolith at 40 s.....	81
Figure 5.7	The surface temperature distribution along the monolith at 40 s.	82
Figure 5.8	The CO-conversion curves for a converter with constant void area and different channel radius (different cell densities).....	82
Figure 5.9	The enlarged view of the first 30 s of the Figure 5.8.....	83

Figure 5.10	The wall temperature along the monolith at 15.7 s for different cell densities.	83
Figure 5.11	The wall temperature along the monolith at 47.2 s for different cell densities.	84
Figure 5.12	The wall temperature along the monolith at 71.8 s for different cell densities.	84
Figure 5.13	The <i>CO</i> -conversion curves for different wall thickness values.	85
Figure 5.14	The monolith wall temperature along the monolith at 15.7s for different wall thickness values.	85
Figure 5.15	The temperature along the monolith at 47.2 s for different wall thickness values.	86
Figure 5.16	The temperature along the monolith at 71.8 s for different wall thickness values.	86
Figure 5.17	The amount of <i>CO</i> -conversion curves for 200 cell/in ² (<i>E_v</i> represents the values of the void fraction).....	87
Figure 5.18	The amount of <i>CO</i> -conversion curves for 600 cell/in ²	87
Figure 5.19	The <i>CO</i> -conversion curves for different converter length, $a(x)L = 2689 \text{ cm}^2 / \text{cm}^3$	88
Figure 5.20	<i>CO</i> -conversion curves for a converter of length 10cm with different $a(x)$ (in $\text{cm}^2 \text{Pt} / \text{cm}^3$) values.	88
Figure 5.21	The light-off time values for a converter of length 10cm with different $a(x)$ values	89

Figure 5.22	Dimensionless <i>CO</i> -concentration along the converter for $a(x) = 268.39 \text{ cm}^2/\text{cm}^3$	89
Figure 5.23	Dimensionless <i>CO</i> -concentration along the converter for $a(x) = 537.68 \text{ cm}^2/\text{cm}^3$	90
Figure 5.24	The <i>CO</i> -conversion for step-function noble metal distribution for different high concentration lengths, $a(x)$ (in $\text{cm}^2 \text{Pt} / \text{cm}^3$)	90
Figure 5.25	The <i>CO</i> -conversion for the step-function noble metal distribution for different $a(x)_{low}$ (in $\text{cm}^2 \text{Pt} / \text{cm}^3$)	91
Figure 5.26	The <i>CO</i> -conversion for the (homogenous) reference case and the step-function noble metal distribution.....	91
Figure 5.27	The <i>HC</i> -conversion for the (homogenous) reference case and the step-function noble metal distribution.....	92
Figure 5.28	The hydrogen conversion for the (homogenous) reference case and the step-function noble metal distribution.	92
Figure 5.29	The <i>CO</i> -emission in g/s for the (homogenous) reference case and step-function noble metal distribution	93
Figure 5.30	Inlet surface temperature for the reference case and the step-function noble metal distribution.	93
Figure 5.31	The outlet temperature for the reference case and the step-function noble metal distribution.	94
Figure 5.32	The <i>CO</i> -conversion for the reference case and the step-function noble metal distribution.	94

Figure 5.33	The effect of inflow-oscillations on <i>CO</i> -conversion efficiency.....	95
Figure 5.34	<i>CO</i> -conversion efficiency for constant mass flux and time dependent mass flux cases.	95
Figure 5.35	Comparison of the monolith wall temperature at different times for the oscillatory and constant inlet mass flux cases.	96
Figure 5.36	Pressure loss for different mass flow rate cases.....	96
Figure 5.37	Temperature contours for different times of the (homogenous) reference case (left column) and the step-function noble metal distribution (right column).....	97
Figure 5.38	Temperature contours of the (homogenous) reference case (left column) and the step-function noble metal distribution (right column) at 240s.....	98
Figure 5.39	<i>CO</i> -conversion efficiency curves for step-function and (homogeneous) reference case noble metal distributions for axisymmetric model.....	99

NOMENCLATURE

h	: heat transfer coefficient, $J/(cm^2 \cdot s \cdot K)$.
v	: gas velocity, m/s .
ε	: void fraction of monolith
$k_{m,i}$: mass transfer coefficient of species " i ", cm/s .
D_i	: molecular diffusivity of species " i " in the reactive mixture, cm^2/s .
S	: geometric surface area p.u. reactor volume, cm^2/cm^3 .
T_s	: wall temperature, K .
T_g	: gas temperature, K .
$C_{g,i}$: gas state concentration of species " i ", mole fraction.
$C_{s,i}$: solid state concentration of species " i ", mole fraction.
$a(x)$: catalytic surface area p.u. reactor volume, $cm^2 \cdot Pt/cm^3$.
$(\Delta H)_i$: heat of combustion of species " i ", J/mol .
$\tilde{R}_i(\bar{C}_s, T_s)$: specific reaction rate for species " i ", $mol/(Pt \cdot cm^2 \cdot s)$
λ_g	: thermal conductivity of gas, $J/(cm \cdot s \cdot K)$.
λ_s	: thermal conductivity of solid, $J/(cm \cdot s \cdot K)$.
P_{tot}	: atmospheric pressure.
Nu_∞	: limiting Nusselt Number.
Sh_∞	: limiting Sherwood Number.
C_{pg}	: Specific heat of gas, $J/(g \cdot K)$.
C_{ps}	: Specific heat of solid, $J/(g \cdot K)$.
\bar{R}	: General gas constant, $N \cdot cm /mol \cdot K$.

Chapter 1

INTRODUCTION

1.1 Problem Definition and Objective of the Study

The gasoline, that contains a mixture of paraffin and aromatic hydrocarbons, became an important part of our lives through the development of the spark-ignited combustion engine. First, it enabled us to have controlled power to operate automobiles. Then, like most of other inventions of human beings, it brought some other problems to solve.

The combustion of gasoline in an engine, in simplified form, can be described as the burning of hydrocarbons with the oxygen and producing the water and carbon dioxide. The ratio of air (source of oxygen) to fuel is an important parameter for combustion. The ideal combustion reaction in which there is enough oxygen (but not excess) to have complete combustion, is called a stoichiometric reaction. However, most of the time, this condition is not possible. The real combustion process is combined of many oxidation and reduction reactions taking place simultaneously. At the end, there are other products as well as water and carbon dioxide. Most of these additional products are pollutants. Depending on different engine operation conditions, the amount of

pollutants varies predominantly by the air to fuel ratio in the combustion chamber. It is known that, within the region of operation of a spark-ignited engine, significant amount of carbon monoxide (CO), unburned hydrocarbons (uHC), and nitrogen oxide components (NO_x) is emitted into the atmosphere. Basically, CO and uHC are the result of an incomplete combustion. Trapped fuel in engine manifolds is another source of uHC . The combustion at high pressure and temperature causes NO_x emission. CO is a direct poison to human beings. HC and NO_x undergo photochemical reactions in the sunlight, leading to generations of smog and ozone.

Air pollution caused by motor vehicle exhaust emissions was first recognized as a problem in the 1950s. The first legislation requiring the control of the automotive emissions was introduced in California in 1966. Since then, many countries have adopted more stringent emission regulations. Motor vehicles also make a major contribution to the atmospheric carbon dioxide levels, one of the main 'green house' effect gases.

There are different foci to control exhaust emissions. These can be classified in two basic groups: the first one is the engine calibration method that includes the modifications in spark timing, exhaust gas re-circulation or air to fuel ratio. All of these methods mainly serve to improve the combustion efficiency of the engine. The second group is the exhaust after treatments. The exhaust after treatments, unlike the engine calibration methods that improve the efficiency of the combustion, aim to reduce all unwanted combustion products.

One of the main important components of the automotive exhaust system that serves to control pollutants is the catalytic converter. The automotive catalytic converters are chemical reactors and work as an afterburner. A catalytic converter consists of a honeycomb structure called the *substrate* and an insulation layer surrounding the substrate. A typical substrate is coated with a gamma alumina wash-coat that supports the noble metals. The exhaust gas, rich with the pollutants, passes through the substrate channels, and diffuses to the walls of these channels. The surface chemical reactions with the effect of the noble metal catalysts are triggered. Unburned hydrocarbons and other combustion products diffused within the walls of the substrate are reduced to relatively non-harmful species by these surface chemical reactions.

There are many interesting physical processes taking place simultaneously in catalytic converters. Heat transfer by convection, conduction, radiation and chemical reactions in gas phase, diffusion mechanisms and surface chemical reactions and condensation of water vapor at the cold-start regime are among these processes. The flow oscillations and different inflow distribution at the inlet of converter depending on different header geometries are also some of the factors affecting the converter performance. Therefore the converter performance is a complicated function of many factors.

The effectiveness of the converter needs to be quantified. The converter efficiency parameters for the poisonous species are usually defined as the ratio of the amount of the converted species to the initial species in percentage. At steady state performance, it is expected that more than 90% of the poisonous

species be converted. Another performance criterion is the light-off time, i.e. the time when 50% of the emission conversion is achieved. It shows how quickly the converter responds to the poisonous species. These criteria are defined in detail in Chapter 5.2.

In the present study, the main objective is to improve the cold-start regime performance by decreasing the light-off time, without increasing the cost of the catalytic converter. One of the main contributions to the cost is due to the noble metal used over the substrate. The efficient use of the noble metal is one way of improving the catalytic converter performance without increasing the cost.

In order to get a better understanding of factors affecting the converter performance, the relative effects of the geometry, the noble metal distribution and the flow oscillations on the converter performance are systematically studied. The surrounding insulation is also studied, since very high temperatures (around 1500°C) might cause mal-functioning or total dysfunction of the converter. The criteria to optimize the converter efficiency are also searched.

1.2 Outline of the Present Study

In the introduction, Chapter 1, problem definition and objectives of the current study with corresponding research approaches and the literature survey are given. In Chapter 2, the physical model is defined. In Chapter 3, the corresponding mathematical model, boundary and initial conditions, including the dimensionless form of the governing equations are presented. The solution

algorithms and finite difference equations are described in Chapter 4. Chapter 5 contains the results of the present study. The nominal values for the problem are given in Section 5.1. In Section 5.2, the performance criterion and the reference case chosen for the study are given and also the result of the computations is compared with the related literature. After the result of the present model is verified with previous studies, the effects of the transient terms that are neglected in the initial model are investigated in Section 5.3. The effects of the different parameters on the converter performance are then investigated for the cold-start regime (i.e. for the period of time when the converter works starting from an initially cold substrate, around 27 °C, until it reaches the steady state) so that an improved catalytic converter performance can be achieved. In Section 5.4, the effect of the geometrical parameters such as channel density and monolith channel radius, wall thickness and converter length are investigated. The noble metal distribution is analyzed in detail, and an alternative noble metal distribution that improves the emission conversion significantly, is proposed in Section 5.5. The effect of the inflow oscillations is given in Section 5.6. In Section 5.7 the results of isothermal study are given in order to verify the constant pressure assumption along the monolith. Since the surface temperature distribution is a critical factor for the converter performance, the model is extended to two-dimensions so that the surrounding insulation can be studied. The results of the two-dimensional model are given in Section 5.8. The general conclusions of the present study are discussed in Chapter 6.

1.3 Literature Survey

The introduction of catalytic converters as emission control devices in the USA goes back to the early 1970's. A substantial amount of research into the parameters that might affect catalyst performance has been carried out. The light-off behavior, the post light-off conversion efficiency, steady state conversion efficiency (see section 5.2) and the pressure loss across the converter are the main parameters studied. The areas that have attracted interest to study the catalyst performance can be classified based on their focuses as follows:

- catalysts housing
- inlet diffuser design
- substrate materials & geometry
- variation in air/fuel ratio
- chemical kinetics data
- chemical poisoning
- 1-D thin film single channel models
- multi-dimensional single channel models
- multi-dimensional monolith models
- isothermal catalyst assembly models

A group of studies is mainly focused on the pressure loss across the monolith or the entire exhaust system, and the inflow velocity distribution. The main concern is to smooth out the velocity profile at inlet using different connection parts so that the pressure loss is reduced and therefore, low drag force is created. Most of

the studies in this area are isothermal and in steady state regime and therefore, they are not suitable to study the cold-start conversion efficiency.

The catalyst housing is the part added to the exhaust system to reduce the emissions. By its existence it creates a resistance to exhaust flow field and therefore increases the pressure loss. One way to decrease back the pressure loss is to use a converter with a shorter length. However, a sufficient amount of converter volume must be available to have good conversion efficiency. Since the diameter of the monolith section is larger than that of the exhaust pipe, an expansion cone or diffuser is used upstream of the monolith section. Because of the limited available space, these inlet diffusers have to be short and wide angled. Such diffusers are inefficient at spreading the exhaust gas uniformly across the catalytic converter. Lemme and Givens [1974] have done theoretical analysis of the effect of the flow mal-distribution on the catalytic converter life. They applied the basic assumption that the conversion efficiency decreases linearly with the amount of gas passing through a given segment of the catalytic converter. In addition, they found that a non-uniform flow distribution reduces durability. They investigated different types of inlet expansions, such as a conical diffuser, a spherical expansion and a 180° expansion. A conical flow deflector successfully flattened the velocity profile of the conical diffuser at the expense of an associated pressure loss.

Wendland and Matthes [1992] studied the steady state flow field that occurs inside a monolith catalytic converter by using water-flow visualization. They conducted tests with transparent, full-scale converter models with several

different header geometries. These headers were truncated or tapered with different lengths and offsets for outlet portion. Results showed that flow invariably separated from inlet header diffuser walls. Tapered inlets of reasonable length do not smooth the flow entering the monolith inlet. The inlet-jet expansion occurs at its impact with the monolith face and not in the inlet diffuser. The shape of this impact jet was found to be independent of the jet Reynolds number over a substantial range of the Reynolds number. They also reported that there is a small change caused by different headers on the steady state conversion efficiency and the light-off time. However, these variations delay the light-off time up to 8 seconds for truncated header cases, which is a very significant delay in our opinion.

Zhao *et al.* [1997] carried out an experimental study to characterize the exhaust flow structure inside a catalytic converter over different operating conditions using cycle-resolved laser doppler velocimetry (LDV) technique. Their conclusion is that the velocity highly fluctuates in the front plane of the catalytic monolith, due to the pulsating nature of the engine exhaust flow. Moreover, the pulsating flow is smoothed significantly after passing through the monolith.

At the beginning of the 1990's, the emission regulations in USA and Europe become tighter resulting in more research in the area of catalytic converters. Lai *et al.* [1991] simulated the three dimensional, non-reacting flow field inside a dual-monolith automotive catalytic converter using finite difference analysis. Fully developed laminar duct-flow pressure gradient with the entrance effect correction was used to formulate the monolith resistance. Their

calculations show that the flow distribution within monolith depends strongly on the diffuser performance, which is a complex function of the flow Reynolds number, the brick resistance, and the inlet exhaust pipe length and the bending angles. Their conclusion is that the smaller the Reynolds number, the straighter and shorter the inlet pipe and the larger the monolith resistance, the more uniform the velocity profile inside the monolith. A similar study by Kim *et al.* [1992] on the flow fields of axisymmetric catalytic converters concludes that small diffuser angles reduce the pressure loss across the system and the flow mal-distribution. The increased monolith resistance, through increasing the cell density or monolith length reduces the flow mal-distribution but increases the pressure loss.

Jeong and Kim [1997] used CFD to investigate three-dimensional unsteady, compressible, non-reacting flow in a catalytic converter system attached to 6-cylinder engine with junction pipes. They concluded that the level of the flow mal-distribution in the monolith heavily depends on the curvature and the angle of separation of mixing pipes.

Bella *et al.* [1991] used a commercial CFD code to predict the steady flow field in a racetrack catalytic converter assembly. Inserting concentric flow deflection vanes within the diffuser flattened the monolith velocity profile. The predicted velocity profiles were used as a boundary condition for a catalyst reaction model. The results confirmed the detrimental effect of the poor flow conditions on the post light-off conversion efficiency.

Another class of studies is focused on the substrate materials and geometry. The metallic substrates were considered as an alternate to ceramic substrates because of their several advantages over ceramic ones. Delieu *et al.* [1977] discussed two advantages of the metallic substrates over ceramic ones. The flexibility of design and the potential for thinner cells that leads to relatively higher cell density without reducing the open volume for exhaust gas flow and therefore resulting in a relatively lower pressure loss. The papers by Nonnemann [1985] and by Kaiser and Pelters [1991] respectively presented similar results on the strengths of the metallic converters. In addition, metallic converters are superior in terms of thermal and mechanical shock resistance, and have a higher thermal conductivity that allows dissipation of local hot spots into surrounding cooler areas. Another advantage of the metallic converters has been given by Bissett and Oh [1993] and by Whittenberger and Kubsh [1991] when using electrical resistance heater (EHC) to accelerate the warming process by reducing the light-off time.

On the other hand, Nishizawa *et al.* [1989] pointed out some of the weaknesses of metallic substrates such as large thermal expansion coefficients, their tendency to have permanent deformation when exposed to excessive thermal or mechanical stresses, their high cost and the poor adhesion between the substrate and wash-coat. The non-porous nature of the metal substrates brings additional cost and effort compared to highly porous ceramic ones.

A study by Japer *et al.* [1991] compared the light-off performance of metallic substrates with similar sized ceramic substrates. Under mal-distributed

flow conditions, ceramic monoliths' light-off time is faster than that of metallic monoliths. However, reverse characteristics may be observed for the uniform flow field case. In addition, the effects of the aspect ratio (constant volume and different length) and split bricks on the ceramic substrate's light-off time were studied. The conclusion is that the light-off time is shortened by using a longer and narrower monolith and split bricks. However, the conclusion can be a result of having different diffusers since the expansion of diffusers is more gradual for the narrower monoliths. With a similar study, Wedland *et al.* [1993] showed that the split bricks might increase the pressure loss ranging 0.7% to 4.1%. Since the combined volume of the substrate is 57% larger than the original monolith volume, there is no basis to compare their light-off performances.

Yamamoto *et al.* [1991] did experimental investigation of the effect of various geometrical parameters such as cell density and wall thickness on ceramic monolith light-off times. Their results on the influence of increased cell density were not conclusive with regard to the light-off time. However, they showed that the higher cell densities resulted in an improved post light-off time conversion efficiency.

There have been very significant developments in catalytic converter performance made by material scientists through improving the noble metal and wash-coat formulations. The noble metals, platinum (*Pt*), palladium (*Pd*), and rhodium (*Rh*), have been found as most effective catalysts for automotive applications. The main purpose of the wash-coat is to provide porous medium with a greatly enlarged surface area so that the noble metals can be easily

deposited. As expected, a larger contact area provides greater surface area available for reactions to take place and therefore improves the efficiency of catalytic converters.

Noble metals *Pt* and *Pd* are effective at oxidation of *CO* and *HCs* and *Rh* are effective at reduction of *NOx*, particularly at stoichiometric exhaust compositions. Three-way catalysts consist of the oxidation reactions of *CO* and *HCs*, and the reduction reactions of *NOx* simultaneously. Therefore, a three-way catalytic converter usually contains *Rh* and one or both of *Pt* and *Pd*. Additional components are also used to improve the effectiveness of these materials. Base metal ceria usually added to wash-coat to inhibit sintering of the noble metals. Moreover, it improves the oxygen storage, which improves the conversion efficiency. A review study by Church *et al.* [1989] explained the role of some of the important components involved in wash-coat and noble metal formulations. There are many other studies in this area of research by different scientists.

The chemical poisoning is another subject widely studied. A review by Kummer [1980] outlines the source of these poisons. Chemical poisoning refers to the deactivation of the catalysts through the absorption of foreign substances. Lead, phosphorus and sulphur are three main poisons. Source of lead is the engine fuel. It can reduce the conversion efficiency if introduced in relatively large amounts. There are two sources for phosphorus in exhaust gases, one is from lubrication oils and the other one is from the fuel. The one from lubrication oils has more detrimental effect than the other one. The sulphur present in the fuel

gets into exhaust gases as sulphur dioxide that suppresses the oxidation of some *HC*s. The short term poisoning by sulphur is reversible.

The overall betterment of the catalytic converter is a very delicate study. The improvement of one performance criterion may impair another one. Therefore, an optimization of these parameters is necessary to have a good design. There are not many studies along this line. A model that includes as many of the parameters mentioned previously as possible is necessary to study the overall effect of these parameters on the converter performance, the conversion efficiency and pressure loss.

The mathematical models of the complex physical and chemical phenomena inside catalytic converters are based on the fundamental transport and conservation equations. There are a number of different assumptions that can be made to simplify the computation, and the solution process. Based on these assumptions, there are different modeling approaches. As expected, increasing the number of assumptions reduces the amount of computation time and/or effort needed to solve the governing equations.

Kuo *et al.* [1971] developed a one-dimensional computational model to simulate the main catalyst phenomena in packed bed type catalytic converters. The authors pointed out that the model could also be applied to monolith type catalytic converters. Later on, Hawthorn *et al.* [1973] developed a one-dimensional single channel model of the monolith with the main assumption that each channel could be treated as an adiabatic system. Nusselt and Sherwood

numbers are used to calculate heat and mass transfer between the exhaust gas and the substrate. Another assumption was that the chemical reactions take place on the wash-coat surface within a thin film. This leads to a simplification of the governing equations that combines the interaction of mass diffusion, heat transfer and reactions within the wash-coat into an apparent reaction term.

Schweich and Leclerc [1990] showed the assumption that the species concentrations and the temperature through the wash-coat are uniform (so that the intrinsic reaction rate is taken as the apparent reaction rate), is not always valid. They pointed out that although the temperature distribution through the wash-coat can be taken as a constant, in case of fast reaction rates and high diffusion resistance of the wash-coat, the distribution of species concentration through the wash-coat is not uniform. They modeled this variation with an effectiveness factor.

There are other one-dimensional models. The main difference among them comes from the use of different Nu and Sh number relationships, different chemical kinetics rate expressions and other minor differences in the governing equations.

Oh and Cavandish [1982] used a transient one-dimensional model that does not include the effect of radiation heat transfer. Lee and Aris [1977] proposed one dimensional steady state model that includes the effect of radiation heat transfer. Psyllos and Phillippopoulos [1992] analyzed the catalytic converter transient behavior again with including radiation heat transfer. The conclusion of

these studies points out that the inclusion of radiation heat transfer flatten out axial temperature gradients, by increasing heat transfer from hot regions to cool regions resulting in a significant change in temperature. To simplify the model, Lee and Aris [1977] represent these effects with a radiation conductivity term.

Baruah *et al.* [1978] developed a one-dimensional model of unsteady flow through a four-cylinder engine and its exhaust system that included a catalytic converter. The motivation behind this study was to model the pulsed nature of engine exhaust flow that is unsteady. A simple, Arrhenius equation for the reaction rates are used. The predicted species concentrations entering the catalytic converter varied little with time compared with the gas temperature.

In multi-dimensional single channel models, the conjugate heat and mass transfer between the gas and substrate has been calculated. Therefore, they don't require heat and mass transfer coefficient expressions (Benjamin *et al.* [2000].) However, thin reacting film assumption was still in the models.

In multi-dimensional monolith models, three-dimensional nature of the inlet velocity fields is included and their effect on catalytic converter conversion and light-off times are investigated. Since modeling of entire monolith channels with exhaust system is not computationally practical, the representative channels are modeled (Chen *et al.* [1988].) Another method is using continuum approach and modeling the substrate as a porous medium. Again, to model heat and mass transfer, the relationship for Nu and Sh numbers are necessary. Bella *et al.* [1991] and Chen [1993] studied the multi-dimensional monolith models. All these

models assume that the flow distribution across the monolith remains constant. They have not compared the results with experimental study.

Clarkson [1995] carried out experimental study to investigate the flow field under isothermal conditions and used these results to study the computational model developed by a commercial CFD code. The study combines the prediction of catalytic converter assembly flow fields with the heat and mass transfer and chemical reactions that occur in the monolith. However, the flow distribution across the monolith is not predicted accurately. These deviations are based on monolith channel entrance effect as a possibility.

In all these models, while modeling the surface chemistry, the mathematical expressions describing the rate of reaction of the emission species are required. These chemistry models are themselves very complex and need specialized expertise. Voltz *et al.* [1973] have published the data of intrinsic rates per unit surface area of noble metal. There are other studies on apparent reaction rates as the rate per unit reactor volume or surface area. The most important point of these studies that differs from the actual monolith problem is they are based on steady state conditions. However, the flow field in catalytic converter is unsteady.

There has been a great improvement in the conversion emissions since 1980's as a result of the different and numerous studies and modeling for the catalytic converter and the exhaust system. However, as the emission

regulations in USA and Europe become tighter, more challenge is introduced to the researchers in this area.

Chapter 2

PHYSICAL MODEL

2.1 Important Parameters for Catalytic Converters

2.1.1 Geometric Parameters

A catalytic converter is made of a honeycomb like substrate. The substrate channels, i.e. *cells*, might have different cross sections. The square cross-section is the most common one. The number of cells per unit area is called *cell density*, typical values may change between 300–700 cells per square inch. The individual channel wall thickness (typical values 0.012–0.006 cm), and the monolith length are two other geometric parameters that are important for the calculations.

The monolith honeycomb of a catalytic converter can be considered as a porous medium, a solid structure with channels produced by void spaces in which the exhaust gas flows. The simplified sketch of the honeycomb structure of the catalytic converter is given in Figure 2.1. In the analysis of porous media, the geometry has important effects on the mechanism of transport. In the macroscopic level, a significant basic geometric parameter for the converter is the *porosity* or the *void fraction*. It is defined as

$$\varepsilon = \frac{V_{void}}{V_{bulk}}.$$

The parameter ε would take values between zero and one. The typical values of void fraction change between 0.6-0.9. Another geometric parameter, the *specific surface area* S , is defined as the total interstitial surface area of a catalytic converter per unit bulk volume of the monolith:

$$S = \frac{A_{surface}}{V_{bulk}} = \frac{2\varepsilon}{R_h},$$

where R_h is the hydraulic radius of the monolith channels.

The metallic or ceramic monolith does not have the quality of the surface to carry the catalyst metal. The carrier is usually a high surface area material containing a complex pore structure deposited on the monolith surfaces. The common carrier used in the automotive industry is Al_2O_3 . This substance helps to provide a surface to disperse the catalytic substance to maximize the catalytic surface area and plays a critical role in maintaining the activity, selectivity, and durability of a finished catalyst. The catalytic surface area per unit gram of substrate is an important catalytic converter specification along with the noble metal loading, which is expressed in terms of gram per unit volume. Typical catalyst compositions are *Pt* or *Rh* with *Pd* in a 2.5:1 or 5:1 ratio, ranging from 1.5-3.1 gram per vehicle.



Figure 2.1 A simplified sketch of a catalytic converter substrate.

2.1.2 Chemical Kinetics Data

The accurate predictions of the catalyst performance depend on proper mathematical descriptions of the rate of reaction of the emission species. The procedures for gaining such data are complex in their nature. The kinetics data published in this area can be classified into three groups. First is the intrinsic reaction rate, given as the rate per reactor unit surface area of noble metals. The values of this reaction rate are obtained from simplified laboratory reactors and noble metal single-crystal studies. The second and third groups consist of apparent reaction rates given, respectively, as the rate per unit reactor volume and the rate per unit reactor surface area. The first of these groups are derived from an actual monolith catalyst and are specific to the particular substrate geometry, wash coat, and noble metal formulation being tested. The second group is derived from simplified catalyst structures, and is specific to a given

wash-coat and a noble metal formulation but can be applied to different substrates. The kinetics data used in this study is the same as those used by Oh et al. [1982]. In their study, the specific reaction rate expressions are given as rates per unit *Pt* surface area and are obtained by calibrating the rate equations of Voltz et al. [1973] against the experimental data measured in their laboratory. The detailed formulation of the kinetic model used in this study is given in Appendix A.

2.2 Single Channel Model

In the single channel model, the physical and chemical phenomena within a single channel catalytic converter substrate are modeled. The monolith substrate that is usually made of ceramic is assumed to isolate the mass and the heat transfer in the gas phase between the channels. Therefore, the behavior of each channel is assumed to be the same, and instead of the entire monolith structure, a single channel is modeled with a given mass flow rate. A further simplification is done as an adiabatic flow.

In the single channel model, the flow within a channel is considered to be laminar and fully developed with known inlet mass flow rate. During the warm-up period, the flow parameters within catalytic converters are highly transient. Specially, the flow within the inlet cone of the catalytic converter is highly turbulent, which will result in different inlet condition for the substrate channels.

There are two different mediums where heat and mass transfer occur inside a catalytic converter. First medium is the exhaust gas within the channels, which has different components. The second one is the channel walls, called as the *solid phase*, by which the exhaust gas components are absorbed.

The main assumption for the chemical reactions taking place in the catalytic converter is that they are confined on the surface of the channel walls. The chemical reactions taking place in the exhaust gas flow are neglected. First, only the transient term in the solid phase energy equation is included to verify the model with existing studies. Later on, the neglected transient terms in the gas phase governing equations for the single channel model are included in the modified model to study their effects on the converter performance. As a result of the heat exchange between the wall and the exhaust gas, wall temperature increases and then the chemical reactions on the channel walls are triggered. Hence the heat released from the channel walls increases both the wall and the exhaust gas temperatures. Details of the equations and assumptions are given in Chapter 3.

2.3 Multi Channel Model

The inlet cone that connects the exhaust pipe to the catalytic converter has highly turbulent flow. Therefore, the flow variation in front of the substrate can be quite significant. To study the effect of the velocity variation in front of the substrate, a three-dimensional model is developed. In this model, the previous

one-dimensional model is extended to three-dimensional one. The channels are stacked on top of each other along the vertical directions normal to the axial flow direction. Since there is no mass transfer of the exhaust gas between the channels, the mass and the energy conservation equations for the gas phase are the same as those of the one-dimensional model. The heat is conducted in the monolith along three-dimensions. The surface chemistry is confined on the channel walls. The differences of the exhaust gas diffusion within the wall are neglected. Therefore, the one-dimensional model will be sufficient to express the solid phase mass conservation equation. Initially, in the vertical direction, the only main difference in our equations for the gas phase mass and the energy equations is from the inflow velocity variation. At later times, this initial difference in the inflow velocity will result in variations of the gas temperature distribution as well as the surface temperature.

There are two fundamentally different sections of the catalytic converter: The insulation layer, which consists of a mat and a steel shell, and the monolith honeycomb substrate. The converter is assumed to have a cylindrical cross section. Due to the similarity of the geometry and the structure of the honeycomb monolith in the vertical directions to the axial flow direction, the axisymmetric plane passing through the center of the substrate is modeled. The detailed form of the equations, as well as, the boundary and the initial conditions are given in Chapter 3. Derivation of these equations is given in Appendix B. The main difference of this model from the one-dimensional model is in the boundary conditions. The conduction heat transfer across the channels is taken into

account by including the heat transfer between channels. Since the inflow velocity varies along the vertical direction, the temperature distributions in gas and solid phase will differ, and therefore create a temperature gradient in the vertical direction.

The surrounding insulation layer is modeled by using only the energy equation for the solid phase since there is no flow through this insulation layer. The schematic for this model is given in Figure 2.2.

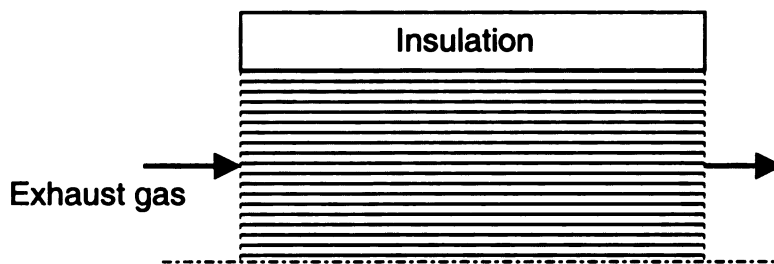


Figure 2.2 Simple schematic of multi-dimensional model

Chapter 3

MATHEMATICAL MODEL

Equations and Boundary Conditions

3.1 Fundamental Equations for One-Dimensional Single Channel Model

In this section, the fundamental equations for the single channel of a monolith converter are presented. The exhaust gas is considered as a multi-component mixture that consists of unburned hydrocarbons, combustion products, and air. There is no mass transfer through the walls of the channels of the monolith substrate. The exhaust gas diffuses through the wash-coat on the surface of the channel walls and is adsorbed over the wash-coat. The components of the exhaust gas in the adsorbed state are said to be in the *solid phase*, in the model. The mass and energy balance equations can be written for each component of the exhaust gas for both gas and solid phases. Four components of the exhaust gas are considered in this model: CO , HC , H_2 and O_2 , which are represented by the indices $k=1,2,3$ and 4 , respectively, in Equations (3.1) to (3.4). The detailed derivations of these equations are given in Appendix B. The NO_x component of the gas is not included in this model due to the lack of reliable chemical and kinetic data. In the one-dimensional model, for an individual channel of the

catalytic converter, the material balance equations for gas (represented by index g) and solid (represented by index s) phases are

$$\varepsilon \frac{\partial C_{g,k}}{\partial t} + \frac{\rho_p V_p}{\rho_g} \frac{\partial C_{g,k}}{\partial x} = k_{m,k} S (C_{s,k} - C_{g,k}) \quad \text{and} \quad (3.1)$$

$$a(x) \tilde{R}_k(\bar{C}_s, T_s) = \frac{\rho_g}{MW_g} k_{m,k} S (C_{g,k} - C_{s,k}) \quad . \quad (3.2)$$

The energy balance equations for the gas and solid phases are

$$\varepsilon \rho_g \frac{\partial T_g}{\partial t} + \rho_p V_p \frac{\partial T_g}{\partial x} = \frac{hS}{C_{p,g}} (T_g - T_s) \quad \text{and} \quad (3.3)$$

$$(1-\varepsilon) \rho_s C_{p,s}^m \frac{\partial T_s}{\partial t} = (1-\varepsilon) \lambda_x \frac{\partial^2 T_s}{\partial x^2} + hS (T_g - T_s) + a(x) \sum_{k=1}^3 (-\Delta H)_k \tilde{R}_k(\bar{C}_s, T_s) \quad (3.4)$$

In Equations (3.1) to (3.4), $C_{g,k}$ and $C_{s,k}$ are the molar fractions of the exhaust gas and the adsorbate component k . The terms ρ_g and ρ_s are densities for the exhaust gas and the substrate walls. MW_g is the molecular weight of the exhaust gas. The term $k_{m,k}$ is the mass transfer coefficient (in m/s) for the component k . The term h ($J / cm^2 \cdot s \cdot K$) is the inter-phase heat transfer

coefficient. S is the geometric property defined as the specific surface area (in m^{-1}). The term $\rho_p V_p$ is the mass flow rate of the exhaust gas in the exhaust pipe. The term $(-\Delta H)_k$ (J/mole) is the reaction heat and the term $\tilde{R}_k(\bar{C}_s, T_s)$ (mol / cm² · Pt · s) is the specific reaction rate for the species k . Their values are given in Appendix A. The amount of noble metal platinum, Pt , along the monolith is represented by the function $a(x)$, with unit (cm² · Pt / cm³), where x is the horizontal distance from the monolith inlet. In the energy-balance equations, T_g and T_s are the temperatures of the gas and solid phases in Kelvin, respectively. The parameter ε is the porosity of the substrate. The term $C_{p,g}$ is the specific heat for the gas. The specific heat for the solid state, $C_{p,s}$, is a function of the surface temperature and therefore a function of time. The term $C_{p,s}^m$ is defined as

$$C_{p,s}^m = C_{p,s} + T_s \frac{\partial C_{p,s}}{\partial T_s} . \quad (3.5)$$

3.1.1 Dimensionless Form of The Balance Equations

In this section, the dimensionless forms of the balance equations are derived. These forms of the equations are used for the model calculations.

The characteristic values used to obtain the non-dimensional form of the Equations (3.1) to (3.4) are as follows: The converter length along the inflow

direction, L ; the hydraulic radius for the channels, R_h ; the average exhaust pipe velocity at the inlet, v_{ave} ; the exhaust gas density at the inlet, ρ_g^{inlet} ; the characteristic time, $t_c = \frac{L}{v_{ave}}$; the gas concentration of the species k at the inlet, $C_{g,k}^{inlet}$; and the gas temperature at the inlet, T_g^{inlet} . The variable x represents the distance in the axial flow direction along the converter length and is measured starting from the monolith inlet.

Using the dimensionless parameters in Equation (3.6),

$$\begin{aligned} \tilde{t} &= \frac{t}{t_c}, & \tilde{v} &= \frac{v}{v_{ave}}, & \tilde{x} &= \frac{x}{L}, & \tilde{R}_h &= \frac{R_h}{L}, & \tilde{a}(x) &= a(x)L, \\ \tilde{D}_k &= \frac{D_k}{v_{ave}L}, & S &= \frac{2\varepsilon}{R_h}, & k_{m,k} &= \frac{Sh_\infty D_k}{2R_h}, & \tilde{\lambda}_x &= \frac{\lambda_x}{\lambda_g^{inlet}} \end{aligned} \quad (3.6)$$

the dimensionless form of the mass and energy balance equations for the gas and solid phase of species k becomes

$$\frac{\partial \tilde{C}_{g,k}}{\partial \tilde{t}} + \tilde{v} \frac{\partial \tilde{C}_{g,k}}{\partial \tilde{x}} = \frac{Sh_\infty \tilde{D}_k}{\tilde{R}_h^2} (\tilde{C}_{s,k} - \tilde{C}_{g,k}), \quad (3.7)$$

$$\tilde{a}(x) \tilde{R}_k(\bar{C}_s, T_s) = \frac{Sh_\infty \tilde{D}_k \varepsilon}{\tilde{D}_a \tilde{R}_h^2} C_{g,CO}^{inlet} \tilde{\rho}_g (\tilde{C}_{g,k} - \tilde{C}_{s,k}), \quad (3.8)$$

$$\varepsilon \check{\rho}_g \frac{\partial \check{T}_g}{\partial \check{t}} + \frac{\partial \check{T}_g}{\partial \check{x}} = \frac{Nu \varepsilon}{Pr Re \check{R}_h^2} \check{T}_g^{0.832} (\check{T}_g - \check{T}_s) \text{ and} \quad (3.9)$$

$$\begin{aligned} \check{\rho}_s \check{C}_{p,s}^m \frac{\partial \check{T}_s}{\partial \check{t}} = & \frac{\check{\lambda}_x \check{R}_h}{Pr Re} \frac{\partial^2 \check{T}_s}{\partial \check{x}^2} + \frac{Nu \varepsilon}{Pr Re \check{R}_h (1-\varepsilon)} (\check{T}_g - \check{T}_s) \\ & + \frac{\check{a}(x) He Da}{(1-\varepsilon)} \sum_{i=1}^3 (-\Delta \check{H})_k \check{R}_k(\check{C}_s, T_s) \end{aligned} \quad (3.10)$$

The common dimensionless numbers that appear in Equations (3.7) to (3.10) are the Prandtl number Pr , the Reynolds number Re , the dimensionless reaction rate $\check{R}_k(\check{C}_s, T_s)$, the Damkohler number Da , and the dimensionless enthalpy number He , which are defined as

$$\begin{aligned} Pr &= \frac{\mu C_{p,g}}{\lambda_g^{inlet}}, & Re &= \frac{\rho_g^{inlet} v_{ave} R_h}{\mu}, \\ \check{R}_k(\check{C}_s, T_s) &= \frac{\check{R}_k(\check{C}_s, T_s)}{\check{R}_{co}(\check{C}_s^{inlet}, T_{so})}, & \check{D}_a &= \frac{\check{R}_{co}(\check{C}_s^{inlet}, T_{so}) MW_g}{v_{ave} \rho_g^{inlet}}, \\ He &= \frac{(-\Delta H)_{co}}{MWC_{p,g} T_g^{inlet}}. \end{aligned} \quad (3.11)$$

The characteristic length used in the Reynolds number is the hydraulic radius. The Equations (3.7) and (3.9) are modified to obtain the Equations (3.7') and (3.9') of the quasi-transient model by omitting the time derivative terms.

$$\tilde{v} \frac{\partial \check{C}_{g,k}}{\partial \check{x}} = \frac{Sh_{\infty} \check{D}_k}{\check{R}_h^2} (\check{C}_{s,k} - \check{C}_{g,k}) \quad (3.7')$$

$$\frac{\partial \check{T}_g}{\partial \check{x}} = \frac{Nu\varepsilon}{PrRe\check{R}_h^2} \check{T}_g^{0.832} (\check{T}_g - \check{T}_s) \quad (3.9')$$

To complete the model, it is necessary to determine the pressure and the velocity distribution inside a channel of the monolith. A brief and compact discussion on how to complete the model is given by Byrne and Norbury [1994]. For the one-dimensional case, the pressure is assumed to be constant to the leading order and the velocity is related to the density of the exhaust gas by the equation

$$\rho_p V_p = \rho_g^{inlet} v_{ave} = \omega(t) , \quad (3.12)$$

where the mass flux, $\omega(t)$, of the exhaust gas along the monolith substrate is considered to be constant.

3.1.2 Initial and Boundary Conditions

The converter surface temperature is initially at the atmospheric temperature since we study the cold-start regime of catalytic converters. The values of the inlet gas temperature and the gas species concentrations used in our computations are based on the experimental measurements of cold start period. The initial gas temperature distribution for the rest of the converter is calculated using the energy-balance equation for the gas phase. Unless otherwise stated, the initial and boundary conditions are given as follows.

Initial condition, ($t = 0$):

$$T_s(x, 0) = T_{so} = \text{constant} \quad (3.13)$$

Boundary conditions:

At the inlet, ($x_{in} = 0$):

$$\begin{aligned} \frac{\partial T_s(x_{in}, t)}{\partial x} &= 0 \\ \omega(t)_{inlet} &= \text{constant} \\ C_{g,i}(x_{in}, t) &= C_{g,i}^{in} = \text{constant} \end{aligned} \quad (3.14)$$

At the outlet, ($x_{out} = L$):

$$\frac{\partial T_g(x_{out}, t)}{\partial x} = 0$$

$$\frac{\partial T_s(x_{out}, t)}{\partial x} = 0$$

(3.15)

The same initial and boundary conditions in the dimensionless form are

Initial condition, (t=0):

$$\tilde{T}_s(\tilde{x}, 0) = \frac{T_{so}}{T_g^{in}} = \text{constant}$$

(3.16)

Boundary conditions

At the inlet, ($\tilde{x}_{in} = 0$):

$$\frac{\partial \tilde{T}_s(\tilde{x}_{in}, \tilde{t})}{\partial \tilde{x}} = 0$$

$$\tilde{\omega}(t)_{inlet} = \text{constant}$$

$$\tilde{C}_{g,i}(\tilde{x}_{in}, \tilde{t}) = \frac{C_{g,i}^{in}}{C_{g,CO}^{in}} = \tilde{C}_{g,i}^{in} = \text{constant}$$

(3.17)

At the outlet, ($\tilde{x}_{out} = 1$):

$$\frac{\partial \tilde{T}_g(\tilde{x}_{out}, \tilde{t})}{\partial \tilde{x}} = 0$$

$$\frac{\partial \tilde{T}_s(\tilde{x}_{out}, \tilde{t})}{\partial \tilde{x}} = 0 \quad (3.18)$$

The time dependent mass flow rate at the inlet is also studied as a separate case and is defined as

$$\tilde{\rho}(\tilde{x}, \tilde{t}) v(\tilde{x}, \tilde{t}) = \tilde{\omega}(0)_{inlet} + \tilde{A} \sin\left(\frac{2\pi}{T} t\right), \quad (3.19)$$

where \tilde{A} and T are the amplitude and the period of the sinusoidal oscillation, respectively.

3.2 Fundamental Equations for the Multi-Channel Model, 3D-Study

In this part of the study, the equations for the three-dimensional model are given. There is no mass transfer between the channels. Therefore, the material balance equations of the solid and gas phases used here are the same as those of the one-dimensional model. Similarly, since once the gas enters the individual channel there is no cross flow, the one-dimensional form of the gas phase energy equation is used for the three-dimensional case. The solid phase energy equation is modified to three-dimensional case by including the heat conduction through the channel walls. In the directions y and z , the heat conduction coefficients are considered to be the same, due to axisymmetric nature of the

geometry. Using the same values of Δy and Δz as grid spacing along the

directions y and z , the term $\lambda_y \frac{\partial^2 T_s}{\partial y^2} + \lambda_z \frac{\partial^2 T_s}{\partial z^2}$, in equation (3.23) reduces to

term $\left(2 \cdot \lambda_y \frac{\partial^2 T_s}{\partial y^2} \right)$. The computation domain can be reduced to a two-

dimensional axisymmetric domain.

An insulation layer is modeled on top of the axisymmetric monolith substrate section. The schematic for the multi-channel model is given in Figure 2.2. The governing equations for the monolith substrate section and the insulation layer are as follows.

Monolith Substrate Section:

For the material balance of the gas and solid phase components, the equation set for the three-dimensional catalytic converter problem is

$$\varepsilon \frac{\partial C_{g,k}}{\partial t} + \frac{\rho_p V_p}{\rho_g} \nabla C_{g,k} = k_{m,k} S(C_{s,k} - C_{g,k}) \text{ and} \quad (3.20)$$

$$a(x) \tilde{R}_k(\bar{C}_s, T_s) = \frac{\rho_g}{MW_g} k_{m,k} S(C_{g,k} - C_{s,k}) ; \quad (3.21)$$

and for the energy balance of the gas and solid phase components we have

$$\varepsilon \rho_g \frac{\partial T_g}{\partial t} + \rho_p V_p \frac{\partial T_g}{\partial x} = \frac{hS}{C_{p,g}} (T_g - T_s) \text{ and} \quad (3.22)$$

$$(1-\varepsilon) \rho_s C_{p,s}^M \frac{\partial T_s}{\partial t} = (1-\varepsilon) \left(\lambda_x \frac{\partial^2 T_s}{\partial x^2} + \lambda_y \frac{\partial^2 T_s}{\partial y^2} + \lambda_z \frac{\partial^2 T_s}{\partial z^2} \right) + hS(T_g - T_s) + a(x) \sum_{k=1}^3 (-\Delta H)_k \tilde{R}_k(\bar{C}_s, T_s) \quad (3.23)$$

Insulation Layer:

Here the subscript and superscript / refer to the properties of the insulation layer. The basic heat transfer mechanism for this layer is the conduction and the governing equation is given as

$$(1-\varepsilon) \rho_I C_{p,I} \frac{\partial T_s}{\partial t} = (1-\varepsilon) \left(\lambda'_x \frac{\partial^2 T_s}{\partial x^2} + \lambda'_y \frac{\partial^2 T_s}{\partial y^2} + \lambda'_z \frac{\partial^2 T_s}{\partial z^2} \right) \quad (3.24)$$

3.2.1 Dimensionless Form of Multi-Channel Model Equations

Dimensionless forms of the balance equations are derived by a similar analysis as performed in Section 3.1.1. The characteristic values in Equation (3.6) are also used to obtain the non-dimensional form of multi-channel equations. In

addition, the length is scaled with the converter radius R_c , in the y and z directions.

Monolith Substrate Section:

The dimensionless form of the solid phase energy balance equation becomes

$$\begin{aligned} \check{\rho}_s \check{C}_{p,s}^M \frac{\partial \check{T}_s}{\partial \check{t}} = \frac{1}{PrRe} \left\{ \check{\lambda}_x \check{R}_h \frac{\partial^2 \check{T}_s}{\partial \check{x}^2} + \check{\lambda}_y \frac{\partial^2 \check{T}_s}{\partial \check{y}^2} + \check{\lambda}_z \frac{\partial^2 \check{T}_s}{\partial \check{z}^2} \right\} \\ + \frac{Nu \epsilon}{PrRe \check{R}_h (1-\epsilon)} (\check{T}_g - \check{T}_s) + \frac{\check{a}(x) He Da}{(1-\epsilon)} \sum_{k=1}^3 (-\Delta \check{H})_k \check{R}_k (\bar{C}_s, T_s) \end{aligned} \quad (3.25)$$

Insulation Layer:

The dimensionless form of the energy equation for the insulation layer is

$$\check{\rho}_I \check{C}_{p,I} \frac{\partial \check{T}_s}{\partial \check{t}} = \frac{1}{PrRe} \left\{ \check{\lambda}'_x \check{R}_h \frac{\partial^2 \check{T}_s}{\partial \check{x}^2} + \check{\lambda}'_y \frac{\partial^2 \check{T}_s}{\partial \check{y}^2} + \check{\lambda}'_z \frac{\partial^2 \check{T}_s}{\partial \check{z}^2} \right\}. \quad (3.26)$$

3.2.2 Initial and Boundary Conditions for Multi-Channel Model

The initial and boundary conditions for the multi-channel model are given to be consistent with the cold-start regime for the catalytic converter. The surface temperature is initially at atmospheric temperature. The temperature and species concentrations for the exhaust gas are given based on the experimental cold-start measurements. The initial exhaust gas temperature distribution for the rest of the converter is calculated using the gas phase energy balance equation. The inlet velocity profile used in our computations, are based on the cold-start velocity measurements at the inlet and are given in Chapter 5. Unless otherwise stated, the initial and the boundary conditions for the dimensionless form of multi-channel model are given as follows.

Initial condition, (t = 0):

$$\tilde{T}_s(\tilde{x}, \tilde{y}, \tilde{z}, 0) = \frac{T_{so}}{T_g^{in}} = \text{constant} \quad (3.27)$$

Boundary conditions:

At the inlet, ($\tilde{x}_{in} = 0$, $\tilde{y}_{in} = [0, 0.8]$, $\tilde{z}_{in} = [0, 0.8]$) :

$$\left. \frac{\partial \tilde{T}_s(\tilde{x}, \tilde{y}, \tilde{z}, \tilde{t})}{\partial \tilde{x}} \right|_{in} = 0$$
$$\tilde{v}(\tilde{x}, \tilde{y}, \tilde{z}, \tilde{t}) \Big|_{in} = \tilde{v}(\tilde{y})_{inlet}$$

$$\check{C}_{g,k}(\check{x}_{in}, \check{y}_{in}, \check{z}_{in}, \check{t}) = \frac{C_{g,k}^{in}}{C_{g,CO}^{in}} = \check{C}_{g,k}^{in} \quad (3.28)$$

At the outlet, ($\check{x}_{out} = 1$, $\check{y}_{out} = [0, 0.8]$, $\check{z}_{out} = [0, 0.8]$):

$$\left. \frac{\partial \check{T}_s(\check{x}, \check{y}, \check{z}, \check{t})}{\partial \check{x}} \right|_{out} = 0 \quad (3.29)$$

At the plane of symmetry, ($\check{y}_{sym} = 0$, $\check{x}_{sym} = [0, 1]$, $\check{z}_{sym} = [0, 1]$):

$$\left. \frac{\partial \check{T}_s(\check{x}, \check{y}, \check{z}, \check{t})}{\partial \check{y}} \right|_{sym} = 0 \quad (3.30)$$

At the upper plane, ($\check{y}_{up} = 0.8$, $\check{x}_{up} = [0, 1]$, $\check{z}_{up} = [0, 1]$):

$$\left. \frac{\partial \check{T}_s(\check{x}, \check{y}, \check{z}, \check{t})}{\partial \check{y}} \right|_{up} = 0 \quad (3.31)$$

The initial and boundary conditions for the insulation layer in the dimensionless form are

Initial condition, ($t = 0$):

$$\tilde{T}_s(\tilde{x}, \tilde{y}, \tilde{z}, 0) = \frac{T_{so}}{T_g^{in}} = \text{constant} \quad (3.32)$$

At the inlet, ($\tilde{x}_{in} = 0$, $\tilde{y}_{in} = [0.8, 1]$, $\tilde{z}_{in} = [0.8, 1]$) :

$$\left. \frac{\partial \tilde{T}_s(\tilde{x}, \tilde{y}, \tilde{z}, \tilde{t})}{\partial \tilde{x}} \right|_{in} = 0 \quad (3.33)$$

At the outlet, ($\tilde{x}_{out} = 1$, $\tilde{y}_{out} = [0.8, 1]$, $\tilde{z}_{out} = [0.8, 1]$) :

$$\left. \frac{\partial \tilde{T}_s(\tilde{x}, \tilde{y}, \tilde{z}, \tilde{t})}{\partial \tilde{x}} \right|_{out} = 0 \quad (3.34)$$

At the inner plane, ($\tilde{y}_{ip} = 0.8$, $\tilde{x}_{ip} = [0, 1]$, $\tilde{z}_{ip} = [0, 1]$) :

$$\left. \frac{\partial \tilde{T}_s(\tilde{x}, \tilde{y}, \tilde{z}, \tilde{t})}{\partial \tilde{y}} \right|_{ip} = 0 \quad (3.35)$$

At the external surface: ($\tilde{y}_{ext} = 1$, $\tilde{x}_{ext} = [0, 1]$, $\tilde{z}_{ext} = [0, 1]$) :

$$\left. \frac{\partial \tilde{T}_s(\tilde{x}, \tilde{y}, \tilde{z}, \tilde{t})}{\partial \tilde{y}} \right|_{ext} = \frac{h_c R_h}{\lambda_y^I} (\tilde{T}_s - \tilde{T}_{amb}) + \frac{h_r R_h}{\lambda_y^I} (T_g^{in})^3 (\tilde{T}_s^4 - \tilde{T}_{amb}^4), \quad (3.36)$$

where h_c, h_r are the convection and the radiation heat transfer coefficients for the outer surface of the catalytic converter.

Chapter 4

METHOD OF SOLUTION

In this chapter, the solution methods for previously described one-dimensional and multi-dimensional models are explained. We have four sets of equations due to four components (species) of the exhaust gas; and for each component, the equations are written for both gas and solid phases. The unknown parameters are concentrations in molar fraction (2×4 of them), and temperatures (2 of them) for gas and solid phases. The finite difference method is used to discretize the governing equations. For convenience, the following notations for the dimensionless parameters are introduced.

$$\tilde{T}_s(\tilde{x}, \tilde{t}) = T_{s,i}^n$$

$$\tilde{T}_g(\tilde{x}, \tilde{t}) = T_{g,i}^n$$

$$\tilde{C}_{s,k}(\tilde{x}, \tilde{t}) = C_{s,k,i}^n$$

$$\tilde{C}_{g,k}(\tilde{x}, \tilde{t}) = C_{g,k,i}^n \quad (4.1)$$

Here, i is the spatial index, n is the index for time, and k is the index for species.

We have used the mid-point rule between two neighboring points along axial direction in our equations. The mid-point rule is defined as

$$T_{g,i}^{n,m} = \frac{T_{g,i+1}^n + T_{g,i}^n}{2} \text{ and } C_{g,k,i}^{n,m} = \frac{C_{g,k,i+1}^n + C_{g,k,i}^n}{2} \quad k = 1,4 \quad (4.2)$$

and only used for the temperature and the concentration of the components in the gas phase.

The gas phase mass and energy equations (3.3) and (3.4) as well as the solid phase energy equation (3.1) are non-linear partial differential equations. The conservation of mass equation (3.2) written for the solid phase is an algebraic equation.

4.1 One- Dimensional Model

In the one-dimensional model, the computation domain consists of the spatial points along the monolith. The first order forward-difference scheme is used for the first-order spatial derivatives in Equations (3.1) and (3.3) with a mid-point rule applied. The second-order central difference scheme is used for the second-order spatial derivative in Equation (3.4). At the boundaries of the computational domain, which is the inlet and the outlet of the channel, the forward-and backward-difference schemes are used respectively. The resultant equations at the grid point, indexed by i , are

$$v_i \frac{(C_{g,k,i+1}^n - C_{g,k,i}^n)}{\Delta x} - \frac{Sh_\infty D_k}{R_h^2} (C_{s,k,i}^n - C_{g,k,i}^{n,m}) = 0 \quad , \quad (4.3)$$

$$\check{a}(x) \check{R}_{k,i} (\bar{C}_s, T_s) - \frac{Sh_\infty \check{D}_k \epsilon}{\check{D}_a \check{R}_h^2} C_{g,CO}^{inlet} \check{\rho}_g (C_{g,k,i}^n - C_{s,k,i}^n) = 0 \quad , \quad (4.4)$$

$$\frac{(T_{g,i+1}^n - T_{g,i}^n)}{\Delta x} - \frac{Nu \epsilon}{Pr Re \check{R}_h^2} \check{T}_g^{0.832} (T_{g,i}^{n,m} - T_{s,i}^n) = 0 \quad \text{and} \quad (4.5)$$

$$\begin{aligned} \check{\rho}_s \check{C}_{p,s}^M \frac{\partial T_{s,i}}{\partial t} = & \frac{\check{\lambda}_x \check{R}_h}{Pr Re} \frac{(T_{s,i+1}^n - 2T_{s,i}^n - T_{s,i-1}^n)}{\Delta x^2} + \frac{Nu \epsilon}{Pr Re \check{R}_h (1-\epsilon)} (T_{g,i}^n - T_{s,i}^n) \\ & + \frac{\check{a}(x) He \check{D}_a}{(1-\epsilon)} \sum_{k=1}^3 (-\Delta \check{H})_{k,i} \check{R}_{k,i} (\bar{C}_{s,i}, T_{s,i}) \end{aligned} \quad (4.6)$$

For each grid point along the monolith, we have ten equations to solve for ten unknown parameters.

The Equations (4.3) and (4.5) become non-linear algebraic equations after using the finite difference scheme for the spatial gradients. These equations along with Equation (4.4) are solved with Powell-hybrid method. The Equation (4.6) becomes a system of ordinary differential equations since we didn't use the finite difference scheme for the temporal derivative. This method of transforming

a partial differential equation to an ordinary differential equation is called the Method of Lines. An ordinary differential equation solver, which automatically switches between the stiff and the non-stiff methods, is used in our computations. The stiff problems are solved with backward differentiation formulas with the modified Newton iteration method. The non-stiff problems are solved with Adams method (Petzold [1983].)

At the start of the computations, the surface temperature distribution $T_s(x,0)$ along the monolith, the exhaust gas temperature $T_g(0,t)$, and the gas species concentration $C_{g,k,i}(0,t)$ at the inlet of the channel, are known. The gas phase energy balance equation, Equation (4.5), is solved to calculate the gas temperature, $T_g(x,0)$, along the converter channel. Then, using the gas and the solid phase temperature distributions with the initial gas concentration at the inlet, the coupled form of Equations (4.3) and (4.4) are solved for the gas and the solid phase concentrations at each spatial location. After the temperature and the species concentration of both gas and solid phases become known, the Equation (4.6) is then solved for the solid phase temperature distribution at the next time step. The information flow diagram for each parameter at each time level n and spatial index i is given in Table 4.1. The algorithm of the entire computation model for the one-dimensional model is given in Table 4.2.

Table 4.1 Information flow diagram for calculation of each parameter, at a given time step n and spatial coordinate i .

$$T_{g,i+1}^n \Leftarrow T_{g,i+1}^n \cup T_{g,i}^n \cup T_{s,i}^n$$

$$C_{g,k,i+1}^n, C_{s,k,i+1}^n \Leftarrow C_{g,k,i+1}^n \cup C_{g,k,i}^n \cup C_{s,k,i}^n \cup T_{g,i+1}^n \cup T_{s,i+1}^n$$

$$T_{s,i+1}^{n+1} \Leftarrow T_{s,i+1}^n \cup T_{s,i}^n \cup T_{s,i-1}^n \cup T_{g,i}^n$$

4.2 Multi-Dimensional Model

The assumptions and simplifications of the multi-dimensional model are given in Chapter 2. The energy balance equation for the solid phase is simplified based on the symmetry of the geometry of the substrate in the directions perpendicular to the flow direction. We carry out the computations for the gas and solid phase temperatures and species concentrations on the axisymmetry plane of the catalytic converter. The horizontal axis of this plane is the axial flow direction starting from the inlet of the catalytic converter. The vertical direction is the direction of the stacked channels starting from the center of the catalytic converter. The values of the calculation increments Δx and Δy in the directions of x and y , respectively, are taken as equal to each other. The value of Δy corresponds to the total thickness of the six channels on top of each other along the y direction. Therefore, one computational row represents six channels stacked together.

In the multi-dimensional model, Equation (3.23) for the monolith section and Equation (3.24) for the insulation layer have additional terms in the y -direction compared to the one-dimensional model. These additional second-order spatial gradient terms are written in terms of the second-order central finite difference schemes. The boundaries of the computational domain are the inlet and the outlet of the axisymmetric plane of the monolith, the symmetry line passing through the center of the monolith, and the upper boundary that corresponds to the steel shell surrounding the insulation layer of the monolith. The forward and the backward difference schemes are used at the boundaries of the computational domain. The resultant equations at each grid point (i,j) are given as follows:

Monolith Substrate Section :

$$\begin{aligned} \tilde{\rho}_s \tilde{C}_{p,s}^M \frac{\partial T_{s,(i,j)}}{\partial t} = & \frac{\tilde{\lambda}_x \tilde{R}_h}{PrRe} \frac{(T_{s,i+1}^n - 2T_{s,i}^n - T_{s,i-1}^n)_j}{\Delta x^2} + \frac{2 \cdot \tilde{\lambda}_y}{PrRe} \frac{(T_{s,j+1}^n - 2T_{s,j}^n - T_{s,j-1}^n)_i}{\Delta y^2} \\ & \frac{Nu \epsilon}{PrRe \tilde{R}_h (1-\epsilon)} (T_{g,(i,j)}^n - T_{s,(i,j)}^n) + \frac{\tilde{a}(x) He \tilde{D}_a}{(1-\epsilon)} \sum_{k=1}^3 (-\Delta \tilde{H})_{k,(i,j)} \tilde{R}_{k,(i,j)} (\tilde{C}_{s,(i,j)}, T_{s,(i,j)}) \end{aligned} \quad (4.7)$$

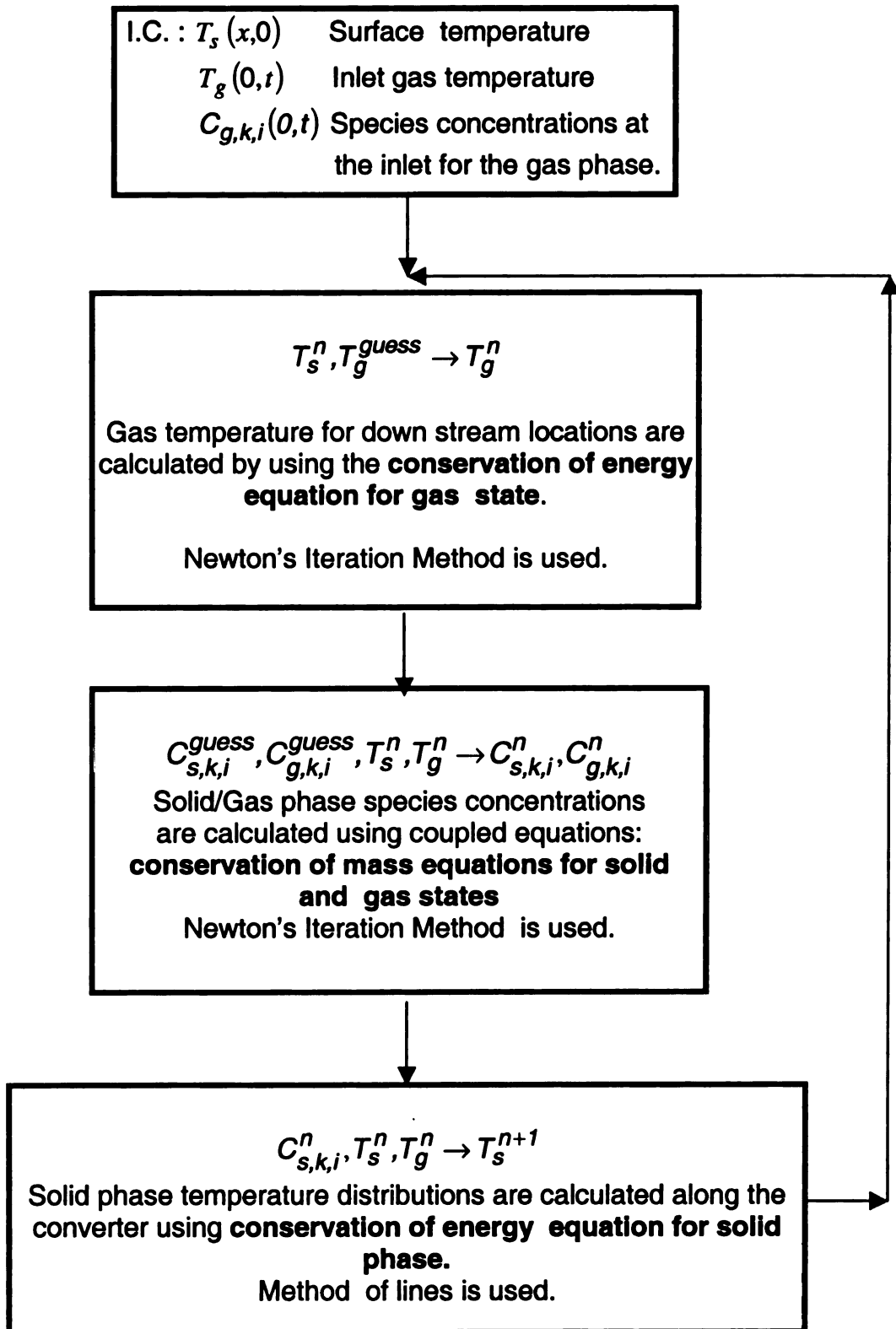
The Insulation Layer:

$$\tilde{\rho}_s \tilde{C}_{p,s}^M \frac{\partial T_{s,(i,j)}}{\partial t} = \frac{\tilde{\lambda}_x \tilde{R}_h}{PrRe} \frac{(T_{s,i+1}^n - 2T_{s,i}^n - T_{s,i-1}^n)_j}{\Delta x^2} + \frac{2 \cdot \tilde{\lambda}_y}{PrRe} \frac{(T_{s,j+1}^n - 2T_{s,j}^n - T_{s,j-1}^n)_i}{\Delta y^2} \quad (4.8)$$

The Equations (4.7) and (4.8) are ordinary differential equations. In our computations, the spatial index (i,j) is simplified to the single index $i_{modified} = (j-1) \times \max(i) + i$, so that we can use the same solver used in the one-dimensional model.

Initially, the surface temperature distribution, $T_s(x,y,0)$, on the computation domain and the exhaust gas temperature, $T_g(0,y,t)$, and the gas species concentration, $C_{g,k,i}(0,y,t)$, at the inlet of the monolith are known. The gas phase energy balance equation, Equation (4.5), is solved to calculate the gas temperature distribution along the substrate at each y location for a given time step. Since the inlet velocity is different at each y level, the gas temperature distribution differs along the y -direction. With the known gas and solid phase temperature distributions and the initial gas concentrations at the inlet, the procedure given in the Section 4.1, is then followed. The coupled form of Equations (4.3) and (4.4) are solved for the gas and solid phase concentrations at each spatial location, for a given time level. After this step of the computation is completed, for a given time at each location, solid and gas phase concentrations become known parameters. Then, Equation (4.7) for the monolith section and Equation (4.8) for the insulation and shell layer are solved for solid phase temperature distribution for the next time step.

Table 4.2 Main flow-chart of the computations



Chapter 5

RESULTS AND DISCUSSION

In this chapter, the results of the different study cases are given. The nominal values for the parameters of the study are given in Section 5.1. In Section 5.2, the performance criterion and the reference case chosen for the study are given and also the result of the computations is compared with that of the related literature. Once the result of the present model is verified with previous studies, the effects of the transient terms in the governing equations that are neglected in the initial model are investigated in Section 5.3. The effect of the geometrical parameters such as the channel density, the monolith channel radius, the wall thickness and the converter length are given for the cold-start regime in Section 5.4. The noble metal distribution is analyzed in detail, and an alternative noble metal distribution that improves the emission conversion significantly, is proposed in Section 5.5. The effect of the inflow oscillations is given in Section 5.6. In Section 5.7 the isothermal study results are given for the verification of the assumption of constant pressure along the converter. Because of the importance of the surface temperature distribution is, as described in Section 5.5, the model is modified to two-dimensional one to study the further effects of the surrounding insulation. The results of the two-dimensional model are given in Section 5.8.

5.1 Nominal Values of the Parameters

In this section, the nominal values for the parameters that affect the converter performance are presented. To verify the results of the current study, the reference case converter parameters are chosen based on the study given in Oh *et al.* [1982].

The geometric parameters are *the channel radius, R_h , the converter length, L , and the void fraction, ε* . The flow parameters are *the atmospheric pressure, P_{tot} and the average flow velocity at the inlet, v_{ave}* . The values of Nusselt Number and Sherwood Number are that of a laminar flow (Shah [1971]) and the viscosity coefficient is taken as that of air at 600K. The Reynolds number is calculated based on the channel radius. The thermodynamic properties involved are *the specific heat for the gas phase, $C_{p,g}$, and for the solid phase, $C_{p,s}$, the gas phase density, ρ_g^{inlet} , at the inlet and the wall density, ρ_s* . The heat transfer parameters are *the solid phase heat conduction coefficient, λ_s and the gas phase heat conduction coefficient, λ_g* , which is approximated by that of the nitrogen and given as a function of the gas temperature. The numerical values of these parameters are given in Table 5.1. The molecular diffusivity D_k of species k , is estimated based on the Slattery-Bird formula (Bird *et al.*[1960]) and is given in Table 5.2 .

Table 5.1 The numerical values of the parameters for *the reference case*.

$T_g^{inlet} = 600K$	$T_s^{initial} = 300K$
$C_{g,CO}^{inlet} = 0.02$	$C_{g,C_3H_8}^{inlet} = 0.00045$
$C_{g,H_2}^{inlet} = 0.00667$	$C_{g,O_2}^{inlet} = 0.04$
$\lambda_s = 0.01675 \text{ J/cm} \cdot \text{s} \cdot K$	$\lambda_g = 2.2695 \times 10^{-6} T_g^{0.832}$
$C_{p,s} = 1.071$	$C_{p,g} = 1.089 \text{ J/g} \cdot K$
$P_{tot} = 101.3 \text{ K} \cdot Pa$	$v_{ave} = 10 \text{ cm/s}$
$\rho_g^{inlet} = 0.000588 \text{ kg/m}^3$	$\rho_s = 2.5 \text{ g/cm}^3$
$A = 60 \text{ cm}^2$	$L = 10 \text{ cm}$
$R_h = 0.06062 \text{ cm}$	$a(x) = 268.39 \text{ cm}^2 \cdot Pt/\text{cm}^3$
$Nu_\infty = 3.608$	$\varepsilon = 0.6836$
$R_g = 28.67 \text{ N} \cdot \text{cm}/(\text{g} \cdot K)$	$Re = 115$

Table 5.2 Diffusivity coefficients for the exhaust gas species in cm^2 / s

$D_{CO} = 1.332$
$D_{C_3H_8} = 0.8095$
$D_{H_2} = 5.1863$
$D_{O_2} = 1.3541$

5.2 The Reference Case and Performance Criteria

There are three different operating conditions for the catalytic converters. These conditions are the converter warm-up (or cold-start), the sustained heavy load, and the engine misfiring. According to the Federal Test Procedure (FTP) for late-

model gasoline vehicles, 70-80% of the total hydrocarbon (*HC*) and carbon monoxide (*CO*) tailpipe emissions occur during the period of the converter warm-up (Hellman, *et al.* [1989]; Whittenberger and Kubsh [1990]). Therefore, it is important to understand the fundamental chemical/physical phenomena and the effects of the time dependent fluctuation of the inlet mass flow rate on the characteristics of converters during the converter warm-up.

In this section the mass flow rate is considered to be constant. The values of the parameters for the case that we use as a basis for comparison are given in Table 5.1. In the rest of the text, this case is referred as "*the reference case*", in which the equations (3.7'), (3.8), (3.9') and (3.10) are used as the mathematical model. The initial species concentrations given in Table 5.1 are from the exhaust gas test data during the warm-up period. The noble metal distribution for the *reference case* is taken to be a uniform distribution with the value, $a(x) = 268.95 \text{ cm}^2 \text{ Pt/cm}^3$. In addition, the mass flow rate and the pressure inside the monolith are considered as constants for the *reference case*.

The results from the simulations are compared with that of Oh *et al.* [1982] for *the reference case* in Figure 5.1 and Figure 5.2. Figure 5.1 shows the monolith temperature along the converter at different times. It can be seen from this figure that at earlier times (e.g. $t = 15.7 \text{ s}$), the hot exhaust gas heats up the upstream portion of the monolith primarily by the convective heat transfer since the converter temperature is not high enough to trigger the chemical reactions on the surface. Therefore, the temperature of the inlet zone is warmer than that of

the outlet zone. As the time goes on ($t=47.2\text{ s}$), the downstream of the monolith becomes warmer due to the heat generated by the exothermic reaction in the upstream section, which is convected to the downstream by the exhaust gas flow. Eventually the monolith temperature peak in the downstream moves slowly to the upstream ($t=71.8\text{ s}$ and $t=124.1\text{ s}$).

The conversion efficiency, CE_i for species i , which is one of the important parameters for the optimum design, is defined as

$$CE_i = \frac{(C_{inlet,i} - C_{outlet,i})}{C_{inlet,i}} \times 100\% ,$$

where $C_{inlet,i}$ and $C_{outlet,i}$ represent the inflow and the outflow exhaust gas concentration of species i , in molar fraction, respectively. The steady state value of the conversion efficiency should be as high as possible for better performance.

Another performance criterion is the light-off time, the time when 50% of emission conversion is achieved. It shows how quickly the converter responds to poisonous species.

In Figure 5.1, the monolith temperature distributions for different time levels are given for our study and study of Oh *et al.*[1982]. The comparison of the CO conversion efficiency CE_{CO} between our numerical results and that of Oh *et al.* are shown in Figure 5.2. In Figure 5.1 and Figure 5.2, we can see that our results are in good quantitative agreement with that of Oh *et al.*

5.3 Effect of Transient Terms in the Gas Phase Conservation Equations

The results that are used to verify the model in section 5.2 are computed with a mathematical model that doesn't include the transient terms for the energy and the material balance equations for the gas phase. In this section, the comparison between the quasi-transient model and the full-transient model, Equations (3.7)-(3.10), is made to show the effect of the neglected time derivative terms in the reference case model.

5.3.1 Effect of the Transient Term In Energy Balance Equation for the Gas Phase

In this section, we compare the quasi-transient, i.e. the reference case model, with the modified model, in which equations (3.7'), (3.8), (3.9), (3.10) are used together with the parameters in Table 5.1. The *CO*-conversion efficiency for each of the cases is shown in Figure 5.3. It shows that the time derivative term in the energy balance equation, referred as the modified case, for the gas phase has some effect in the warm up period. Initially, for time < 35s, the *CO*-conversion efficiency of the modified case is slightly less than that of the reference case. This is expected since initially the surface temperature is less than the gas temperature. Hence, the gas temperature warms up the wall of the converter. The surface chemistry is not activated over the entire monolith surface yet. Therefore, the gas temperature decreases toward the outlet. The effect of this decrease is observed to be quicker when the time derivative term is included in the gas phase energy equation. The gas and the surface temperatures of the

modified case at the outlet are less than that of the reference case (see Figure 5.4 and Figure 5.5.) It is noted from the figures that both the gas and the surface temperatures of the modified case are higher than that of the reference case near the inlet. This is again due to the transient term that helps to carry the effect of the initial activation of the surface chemistry faster. Additional energy, carried at the inlet to further time steps of the modified case, warms up both the surface and the gas. As time goes on, the cumulative effect of having higher temperatures around the inlet region for the modified case results in a better CO-conversion. The surface temperature of the converter warms up to initial gas temperature and becomes higher for the entire monolith surface, so the conversion efficiency becomes the same as the reference case around the light-off time. Because of the time derivative term, both the gas and the monolith surface get warmer relatively faster compared to that of the reference case (see Figure 5.6 and Figure 5.7) for the entire surface, and therefore improve the conversion efficiency just after the light-off time. Once the steady state value is reached, both the reference case and the modified cases have the same steady state value.

The temperature variations along the converter for the modified and *the reference case* are shown in Figure 5.4 to Figure 5.7. As we see in these figures that although the temperature variations along the converter differ from each other for the reference and the modified cases, the overall effect of the time derivative term is not significant with respect to the conversion efficiency, since the area under the conversion efficiency curves in Figure 5.3 are almost the

same. This means that the total *CO* emission calculated over the warm-up period for both cases are almost the same. The conclusion is that the quasi-transient approach to the model energy balance equation for the gas phase can give quite realistic results in terms of the integral quantities.

5.3.2 Effect of the Transient Term in Mass Balance Equation for the Gas Phase

The transient term in the mass balance equation, Equation (3.7), for the gas phase is included for each species. The values of the parameters in Table 5.1, the reference case parameters along with the initial and boundary conditions are applied. The computations show that the addition of the transient term in the mass balance equations for the gas phase does not bring any significant change in the computed parameters. There is no apparent difference in the graphical representation of the results. The difference in the numerical values is only at the range of 0.01%. Since the graphical representations of the results with the transient terms look exactly the same as those in Figure 5.3 to Figure 5.7, they are not shown separately in this section.

5.4 Effect of Geometrical Parameters

This section includes the investigation of the effect of geometrical parameters for the case with constant inlet mass flux. The inlet conditions and other parameter values used are the same as the reference case (see Table 5.1), unless otherwise stated. Three different cases of the geometrical parameters are

investigated. First one is for the case of a constant void area. In this case, different cell densities and hence different void fractions and channel radii, are tested. The monolith wall thickness is kept constant at $d=0.0254$ cm. In the second case, the void fraction has been kept constant. Here, the monolith wall thickness and the cell density vary in order to keep the void fraction constant. In the third case, different converter lengths are considered.

5.4.1 The Effect of Cell Density

In this section, the effect of changing the cell density on the conversion efficiency is studied. The geometrical parameters and the corresponding Reynolds numbers of the investigated cases are given in Table 5.3. The *CO*-conversion curves versus time for these different channel cell-density cases are given in Figure 5.8. Figure 5.8 shows that as the cell density decreases the conversion efficiency gets better and the light-off time gets shorter. However, an enlarged view of Figure 5.8 for the first 30 seconds shows the existence of a reverse pattern at very earlier times (Figure 5.9). This characteristic has an important effect at higher initial gas temperatures.

Table 5.3 The values of the geometrical parameters and corresponding Reynolds numbers for different cell densities (constant wall thickness and void area.)

Radius (cm)	Cell density	Re	Void fraction
0.08	200	165	0.7371
0.06	300	130	0.6836
0.04	600	84	0.5696

Figure 5.10 shows the monolith wall temperature at 15.7s for different cell density cases (different channel radii). It is seen that the inlet and the outlet temperature distribution patterns are different. At earlier times, the downstream temperature of the monolith wall is not high enough to activate the surface chemical reactions. The main heat transfer mechanism is the convection. However, around the inlet, the surface chemical reactions are active and therefore increase the surface temperature slightly higher than the gas temperature. At later time steps, the temperature of the monolith reaches its maximum at the exit, and then the temperature peak moves to the upstream (see Figure 5.11 and Figure 5.12). The monolith temperature distributions at 47.2 s and 71.8 s for different cell densities are shown. Both of them show that as the cell density decreases, the location of the temperature peak moves to the upstream and the magnitude of the temperature peak increases. Therefore, smaller cell density leads to a better overall conversion. One could argue that for a higher cell density case the conversion efficiency should be better since the contact surface is larger. However, since the void fraction decreases, the storage term of the energy balance for the gas phase gets smaller, which leads to a smaller increase in the surface temperature.

5.4.2 The Effect of Wall Thickness

In this section, the void fraction and the void area have been kept constant. Therefore, the change in the wall thickness leads to different channel radii and cell densities. The geometrical parameters examined here, are given in Table

5.4. Figure 5.13 shows the *CO*-conversion efficiency versus time for different wall thickness cases.

Table 5.4 The values of the geometrical parameters for different cases, (constant void area and fraction.)

Radius (cm)	Cell density	Re	Wall thickness (cm)
0.0742	200	160	0.0312
0.0606	300	130	0.0254
0.0428	600	92	0.0179
0.0303	1200	65	0.0127

As we can see in Figure 5.13, there are two regions with different conversion characteristics. The first region is for conversion efficiency lower than 50% and the second one is for the conversion efficiency higher than 50%. It is seen that as the wall thickness decreases, i.e. the cell density increases, the conversion efficiency improves at earlier times. However this pattern is not preserved for the latter times. Among the cases considered, the overall best conversion performance is of the case with the wall thickness $d = 0.0179$ cm. Moreover, we see that the smaller wall thickness leads to very poor steady state conversion efficiency at later times. Figure 5.14 shows the monolith wall temperature distribution at 15.7s for the cases examined. It is seen that the smaller the wall thickness, the higher the surface temperature. Figure 5.15 and Figure 5.16 show the surface temperature at times 47.2 s and 71.8 s, respectively. For these cases, we can see that the transition of the behavior of the converter characteristics from earlier to latter times is around 47 s. Moreover,

the smallest wall thickness does not give the best thermal characteristics as it does for the earlier time 15.7 s (see Figure 5.15).

From these results, we conclude that there is an optimum value for the wall thickness that gives the best conversion efficiency for a given void area and void fraction. These results are valid under the given model assumptions and during the warm-up period. The characteristics of the temperature and conversion curves may change at different times for other cases, e.g. the heavy loading case.

The results for the cases with constant void area and void fraction are presented together in Figure 5.17 and Figure 5.18. Both figures show that as the wall thickness decreases the conversion efficiency gets better for the cases tested.

5.4.3 The Effect of Converter Length

The effect of converter length on the converter performance is investigated in this section. The same boundary conditions as before are used for all cases examined in this section. The elements of the variable set are the length of the converter, L , and the noble metal density distribution, $a(x)$, for each case, while the product $a(x)L$, i.e. the total amount of the noble metal (Pt) used in the converter, is kept as constant at $2689 \text{ cm}^2 \text{ Pt} / \text{cm}^3$.

In Figure 5.19 we see the CO -conversion efficiency versus time for various converter lengths. For better conversion efficiencies, the steady state

value should be as high as possible, while the light-off time should be as short as possible. Having higher steady state conversion efficiency is more beneficial in the long term. Therefore, if we have to sacrifice the steady state conversion, the short light-off time is not desirable. For the converter with the length $L=2.5$ cm and $L=5$ cm, the light-off time is shortest among all four cases. However, it is obvious that the steady state conversion values are not as good as those of the longer converters. Among these four cases, the best overall conversion efficiency is found with the converter length of 10 cm. When the substrate is getting longer than 10 cm, the steady state value for the conversion efficiency is getting lower and the light-off time is getting longer. This result shows that for a given amount of noble metal, there is an optimum value of the converter length to achieve the best overall conversion efficiency.

5.5 The Effect of Noble Metal Distribution

In this section, the effect of the noble metal distribution is tested. The wash-coat deposition can shorten the channel radius in reality, depending on the amount. Therefore, the amount of wash-coat that can be deposited on a converter length is limited with the substrate channel radius. In case of higher catalyst concentrations, the available flow area can be decreased. However, in this part of the study, it is assumed that the increase in the amount of the noble metal doesn't change the volume of the wash-coat.

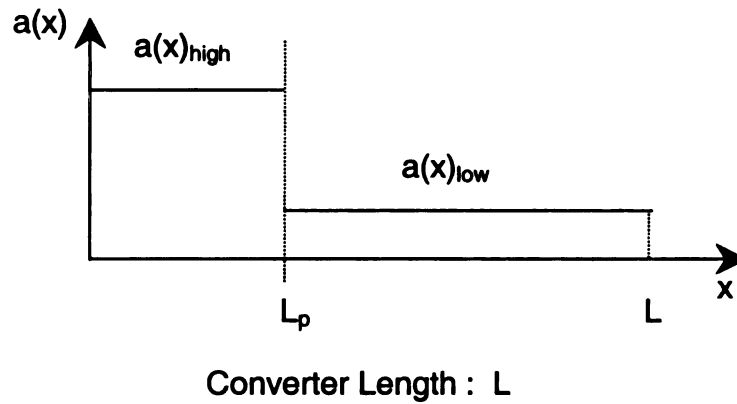
5.5.1 Homogenous Noble Metal Distribution

The CO -conversion efficiency curves for a converter of length 10 cm with different uniform noble metal concentrations are shown in Figure 5.20. It shows that the increase in catalyst, i.e. noble metal concentrations, affects the light-off time, the value of the steady state conversion efficiency and the time to reach this value, significantly. In Figure 5.21, the light-off time versus noble metal concentrations are given for five different cases. It is observed that after $a(x)$ value becomes larger than $700 \text{ cm}^2 \cdot \text{Pt/cm}^3$, the gain in the light-off time does not bring as much benefit as between values $268\text{-}700 \text{ cm}^2 \cdot \text{Pt/cm}^3$.

The dimensionless CO -concentration distributions along the converter for different times of *the reference case*, $a(x) = 268.39 \text{ cm}^2 \cdot \text{Pt/cm}^3$, are given in Figure 5.22. The distribution is almost a linear decrease at early times. As the time goes on a drastic conversion takes place towards the second half of the converter where the temperature reaches its maximum value (see Figure 5.1.) When we look at a similar profile in the case of higher noble metal distribution ($a(x) = 537.68 \text{ cm}^2 \cdot \text{Pt/cm}^3$), we see in Figure 5.23 that almost 90% of CO is already converted in the first 30 seconds at the middle of the converter. In other words, the larger portion of the conversion takes place in the first half of the converter. Since the catalysts are expensive noble metals, the important question that arises here is what would be the efficient usage of the noble metal catalysts. In the following section, several numerical examples are given to investigate the efficient usage of the noble metal catalysts.

5.5.2 Efficiency Analysis for Noble Metal Distribution

The step-function distribution for the noble metal catalysts is proposed here. The high concentration of the noble metal, referred as $a(x)_{high}$, is in the front section and the lower concentration of the noble metal, referred as $a(x)_{low}$, is in the back section of the converter. The location where the transition from high to low concentration takes place is called as L_p (see Schema 5.1).



Schema 5.1 The alternative noble metal distribution: The step-function distribution

The reason of choosing such a distribution is based on the results observed in the dimensionless CO -concentration distribution along the converter (Figure 5.22 and Figure 5.23). It is shown that most of the conversion takes place at the front 40% of the converter length during the first 30 seconds for a converter with the homogenous noble metal distribution of $a(x) = 537.68 \text{ cm}^2 \cdot \text{Pt/cm}^3$.

Figure 5.24 shows the CO-conversion efficiency curves for the cases with different transition lengths, $L_p = \frac{L}{2}$, $\frac{L}{3}$ and $\frac{L}{4}$, for a given step-function, $a(x)_{high} = 600 \text{ cm}^2 \cdot \text{Pt} / \text{cm}^3$ and $a(x)_{low} = 1 \text{ cm}^2 \cdot \text{Pt} / \text{cm}^3$. Here $a(x)_{low} = 1 \text{ cm}^2 \cdot \text{Pt} / \text{cm}^3$ can be thought of as having no noble metal at all since its value is very small. This small non-zero value is taken for computational reasons. As it is shown in Figure 5.24, the transition location L_p of the noble metal distribution slightly affects the light-off time, which is around 20 seconds. It is noted that in Figure 5.21, the light-off time of the homogeneous noble metal distribution with $a(x) = 600 \text{ cm}^2 \cdot \text{Pt} / \text{cm}^3$ is also about 20 seconds. The steady state values of the curves, however, are quite different for each case. As length L_p increases, the steady state conversion becomes better.

Since the light-off times are quite close to each other for all cases with different L_p 's, the transition length $L_p = L/4$ is chosen for the following test, so that the consumption of the noble metal catalysts is minimum. In the test, $L_p = L/4$ and $a(x)_{high} = 600 \text{ cm}^2 \cdot \text{Pt} / \text{cm}^3$ values are kept as constants while the value of $a(x)_{low}$ is changed. In Figure 5.25, CO-conversion efficiencies are shown for different $a(x)_{low}$ values of 1, 79, 158 and $300 \text{ cm}^2 \cdot \text{Pt} / \text{cm}^3$. The CO-conversion curves slightly differ from each other only in the region of 20-30 seconds for cases with $a(x)_{low} \geq 39$. Therefore, it might not worth to use higher

noble metal concentration for $a(x)_{low}$ just to gain a slight improvement in efficiency for these 10 seconds.

Motivated by the need to reduce the emissions at no additional cost of the noble metal catalysts, numerical test problems are then formulated in order to answer the following two questions. The first question is that how much emission reduction can be achieved when replacing a homogeneous noble metal distribution by a simple step-function while keeping the total amount of the noble metal catalysts as constant. The second question is that how much noble metal catalysts can be saved using a simple step-function noble metal distribution if the emissions are kept unchanged as that of the homogeneous distribution. In order to answer the first question, the *CO*-conversion efficiency is calculated and shown in Figure 5.26 for the *reference case* and the step-function case with $a(x)_{high} = 645 \text{ cm}^2 \cdot \text{Pt}/\text{cm}^3$, $a(x)_{low} = 80 \text{ cm}^2 \cdot \text{Pt}/\text{cm}^3$ and $L_p = L/3$. Although the amount of the noble metal catalysts used for the above two cases is the same, it is clearly seen from the figure that a significant reduction in the emissions is achieved as a result of a much shortened light-off time for the step-function case. The light-off time is reduced by approximately 35% (by about 14 seconds.) In addition, a similar reduction of the light-off time for the species H_2 and C_3H_6 , propylene, is achieved for the step-function distribution case. These results are shown in Figure 5.27 and Figure 5.28. Here, propylene is assumed to be a representative of *fast oxidizing hydrocarbon* in the automobile exhaust.

In order to quantify the reduction in the amount of the emissions (e.g. CO emission), three potential driving cases are considered. The conditions of these cases are given in Table 5.5. From the simulation result shown in Figure 5.26, the mass flow rate of CO at the outlet of the converter is calculated as a function of time and is shown in Figure 5.29. The averaged CO emission, in g/s , is then calculated and shown in Table 5.6, for the three trips with both the homogeneous and the step-function noble metal distributions, respectively. As we can see that significant CO emission reductions are achieved: about 32% for trip 1, 27% for trip 2 and 17% for trip 3. A higher CO emission reduction for short distance trips is expected due to the reduction in the light-off time as a result of using the step-function noble metal distribution.

To answer the second question raised above, another case of the step-function noble metal distribution is considered with $a(x)_{high} = 380 \text{ cm}^2 \cdot Pt/cm^3$, $a(x)_{low} = 75 \text{ cm}^2 \cdot Pt/cm^3$ and $L_p = L/3$. It is worth to mention that the amount of the CO -conversion for this step-function case is approximately the same as that for *the reference case*. This can also be seen from the conversion characteristics shown in Figure 5.32. The amount of the noble metal saved by using the step-function distribution is about 34%.

The results shown above demonstrate that the transient conversion characteristics are improved dramatically when using the step-function noble metal distributions. Since the overall performance of converters is also affected by the transient thermal characteristics, the inlet monolith temperature as a

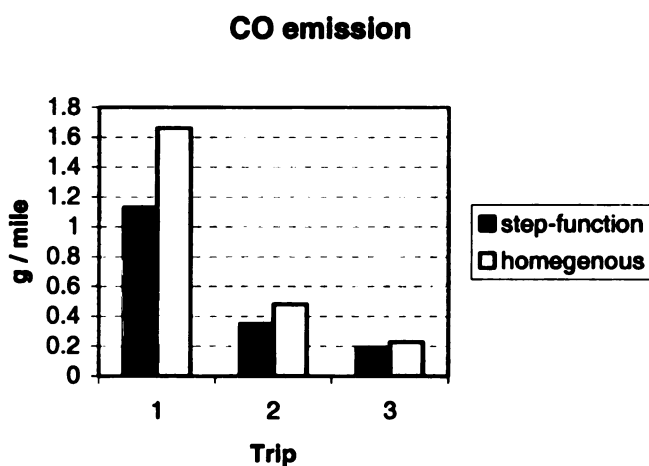
function of time is studied and compared with that of *the reference case* in Figure 5.30 and Figure 5.31 for the above two step-function cases. As we can see that there is a large temperature surge at the inlet for the case of $L_p = L/3$, $a(x)_{high} = 645 \text{ cm}^2 \cdot \text{Pt}/\text{cm}^3$, and $a(x)_{low} = 80 \text{ cm}^2 \cdot \text{Pt}/\text{cm}^3$.

Although catalytic converters are designed to withstand occasional high temperature operation, prolonged and repeated exposure to very high temperatures leads to loss of noble metal surface area and even deterioration of the catalysts support. The effects of the temperature surge on the converter performance, therefore, need to be further studied. The results from our preliminary study suggest that all the three parameters, $a(x)_{high}$, $a(x)_{low}$, L_p , affect the transient monolith temperature. Since the thermal durability of the catalysts and the substrate dictate much of the design of an exhaust system, it is important to choose optimum values for $a(x)_{high}$, $a(x)_{low}$ and L_p such that the conversion characteristics can be improved without further deterioration of the noble metal catalysts. The statistical information on the location of deterioration of catalysts can provide some insights for an optimum converter design via the step-function noble metal distributions. In addition, an optimum noble metal distribution needs to be investigated with the understanding that the optimum noble metal distribution proposed has to be practical for the manufacturing.

Table 5.5 Three real-life driving cases

Trips/Cases	Traveling Speed (miles/hour)	Traveling Distance (miles)
1	35	20
2	70	80
3	70	300

Table 5.6 Comparison of the CO -emissions of the reference case to the step-function noble metal distribution.



In summary, the study on the effect of noble metal, Pt , distribution shows that with higher amount of catalyst the surface chemistry is activated earlier. This has two important results: First, the conversion starts earlier around inlet region of monolith. Since the conversion reactions are exothermic, the excess heat transferred to downstream warms up the monolith surface temperature and activates the corresponding surface chemistry earlier. Our conclusion is that the early attainment of high surface temperature (high enough to activate the surface

chemistry around 650K) is necessary to have better conversion efficiency. The results of the simulations with different noble metal concentrations show that the light-off time is an exponentially decreasing function of the noble metal, *Pt*-concentration (Figure 5.21). Therefore, the amount of noble metal used in converter is better to be decided based on the percentage of improvement in the light-off time since the cost of the noble metal is high. The second important observation is that, once the surface temperature around inlet is high enough to activate the surface chemistry, the excess energy dissipates to the downstream and therefore the amount of the catalyst necessary in the downstream would be less than the inlet region on the monolith. Based on this observation, the step function noble metal distribution (Schema 5.1) that has high concentration around inlet and low concentration around outlet is proposed and tested as an alternative noble metal distribution. The simulations in which, the same amount of catalyst is used for the homogenous and the step function noble metal distribution, show that the light-off time is shortened by approximately 35%. Moreover, compared to the homogeneous noble metal distribution, the exhaust emissions are reduced significantly by using a simple step-function noble metal distribution. In addition, the cost of the noble metal catalysts used in the catalytic converters can be reduced when using the step-function noble metal distribution while keeping the emissions the same as that of the homogeneous distribution. It is critical to choose optimum values for high and low noble metal concentration of the step function. The high concentration value and the transition length, affect the light-off time. The value of the low noble metal concentration affects the

steady state conversion. The qualitative criterion based on noble metal concentration versus the light-off time could be used as a basis for choosing these variables (Figure 5.21).

5.6 The Effect of Inflow Oscillations

The inflow of the catalytic converter is time dependent due to the nature of the combustion that takes place in the engine. In this section of the study, our purpose is to find out if the oscillatory behavior of the exhaust gas affects the characteristics of the converters. The inlet mass flow rate is taken as a sinusoidal function for simplicity (see equation 3.19.)

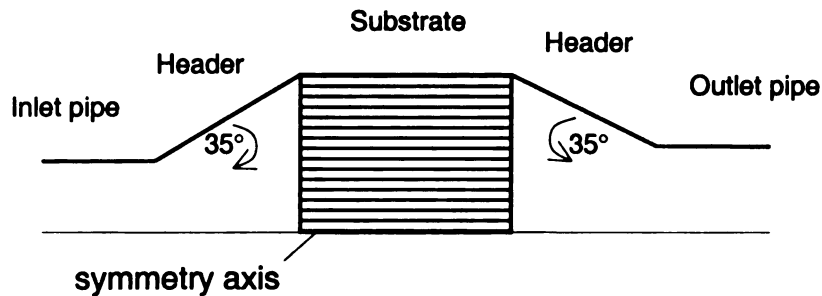
Although it is not realistic to have such regular fluctuations under normal operational conditions of the engine, it is useful to examine the effects of such fluctuations on the conversion efficiency. Various oscillation amplitudes and oscillation frequencies are considered in the simulations. In Figure 5.33a, the time fluctuation functions of the inlet mass flow rate in the warm-up region are seen for some period of time. In Figure 5.33b, the corresponding amount of *CO*-conversion at the converter exit for each fluctuation function of the inlet mass flow rate is shown for the same period of time. It can be seen from Figure 5.33a and b that the fluctuation of the mass flow rate at the inlet and the corresponding fluctuation of the conversion efficiency at the exit are not in phase. The patterns of the fluctuation, however, are preserved for the cases examined.

The results demonstrate that the inlet mass fluctuation affects the conversion efficiency at the exit during the warm-up period. Therefore, it is possible for us to control the exhaust gas oscillation so that better conversion characteristics could be achieved. Further study on the mechanism related to the oscillation of the mass flow rate at the inlet and the oscillation of the conversion efficiency at the exit is needed. In Figure 5.34, the overall effect of the time dependent inlet mass fluctuation on the conversion efficiency is seen. Figure 5.35 shows the comparison of the monolith wall temperature at different times for the oscillatory and the constant mass flow rate. A sine-function oscillation of the inlet mass flow rate is used for the comparison in Figure 5.35. It shows that the temperature peak is shifted to upstream in the case of oscillation. This shift might be the main reason to have better *CO*-conversions. The magnitudes of the temperature peak are slightly decreased due to oscillations. It is worth noting that it is not necessarily true that a time dependent oscillating mass flow rate at the inlet would always improve the conversion efficiency. However, it is clear that the inlet mass flow rate oscillation affects the conversion efficiency for earlier times during the warm-up period. This investigation shows the necessity of a further study in order to fully understand the mechanism relating the mass flux fluctuation and the conversion efficiency.

5.7 Isothermal Study Results for Pressure Drop Calculations

In section 5.2, we stated that in our study the constant pressure assumption is used inside the monolith. In this section, by isothermal model calculations, we

would like to verify the validity of this assumption. The CFX-4.3 software is used to simulate the axisymmetric two-dimensional model.



Schema 5.2 The geometry of the isothermal model.

The model includes the inlet pipe, headers with divergence angles 35° , the substrate section and the outlet pipe. The schematic of the model is given in Schema 5.2.

In the computational model, the substrate section is modeled as a porous medium. The relationship between the velocity and the pressure is defined with Darcy's Law. Based on the results of the experimental study of Kreucher *et al.* [1996] on different substrate lengths, inlet pipe lengths and headers, the necessary flow resistance coefficients for the substrate are calculated. Then using these coefficients, the pressure drop for the geometry is found. The computed results as well as the experimental results by Kreucher *et al.* [1996], are given in Figure 5.36. The overall pressure drop corresponds to the entire system from the beginning of the inlet pipe to the end of the outlet pipe. The pipe pressure drop corresponds to a pipe with the same length as the length of the

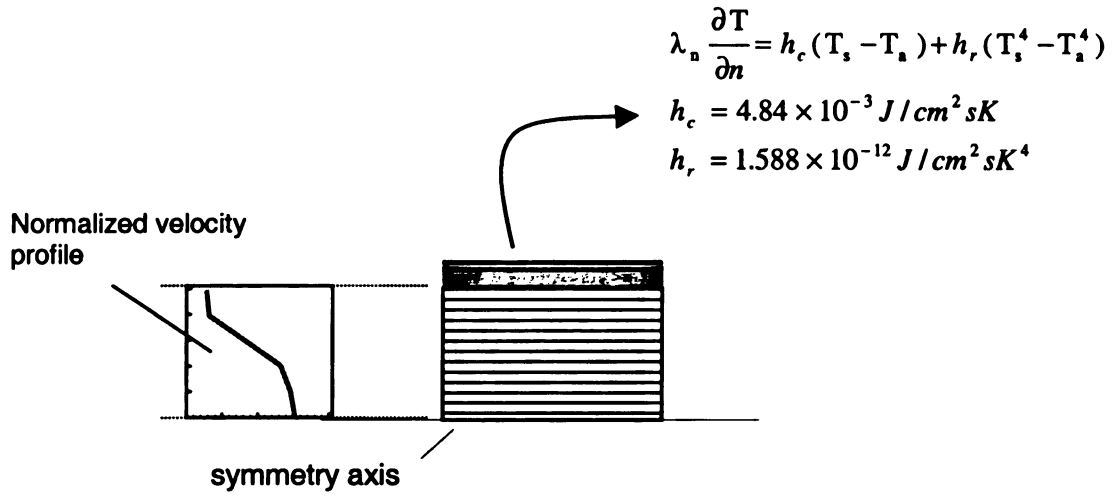
entire system and with a diameter the same as the diameter of the substrate section. The header pressure drop corresponds to a difference between these two pressure drops.

The substrate pressure drop, for the mass flow rate (40 g/s) of the *reference case*, is 0.2 kPa, as seen in the Figure 5.36(b). This result is in good agreement with the previous assumption of the constant pressure along the converter. In the previous model that includes the surface chemistry, the change in the gas density is caused by the abrupt change in the temperature rather than the gradual pressure drop along the converter.

5.8 Axisymmetric Model Analysis

In this section, our purpose is to investigate the magnitude and the location of the temperature peak due to the variation of the inflow velocity along the vertical direction. Moreover, differences of the temperature distribution between the reference case and the step-function noble metal distribution are studied. Finally, the overall conversion efficiency, that is the integral emission quantity over all the channels, is computed.

The axisymmetric model is developed based on the discussions in Section 2.3 and equations in Section 3.2. The geometry of the axisymmetric model and dimensionless inflow velocity profile are shown in Schema 5.3. The striped section is for the monolith, the gray area for the insulation mat and the black striped upper layer for the surrounding steel layer.



Schema 5.3 The geometry of the axisymmetric model

The parameters used in this part of the study for a channel is given in Table 5.1. In the vertical direction, every six-channel is grouped to be one computational row. Surrounding the monolith section, there is an insulation layer, and finally the steel metal covers the insulation layer. These two layers, as expected, have different heat transfer characteristics and conduction coefficients than the monolith part. These values are listed in Table 5.7 . The character λ represents the conduction coefficients and C represents the specific heat coefficients. The convective and the radiation heat transfer take place on the upper boundary. The value of the convective heat transfer coefficient is $h_c = 4.84 \times 10^{-3} \text{ J/cm}^2 \text{ sK}$ and the radiation heat transfer coefficient is $h_r = 1.588 \times 10^{-12} \text{ J/cm}^2 \text{ sK}^4$. The monolith layer has radius of $r = 4.64 \text{ cm}$, the

insulation mat has a thickness of $t_{mat} = 0.33 \text{ cm}$, and the steel layer cover has thickness of $t_{steel} = 0.145 \text{ cm}$.

Table 5.7 Heat Transfer coefficients

$$\lambda_{monolith} = 0.00265 \text{ J} / \text{cm} \cdot \text{s} \cdot \text{K}$$

$$\lambda_{mat} = 0.0018 \text{ J} / \text{cm} \cdot \text{s} \cdot \text{K}$$

$$\lambda_{steel} = 0.26 \text{ J} / \text{cm} \cdot \text{s} \cdot \text{K}$$

$$C_{monolith} = 1.071 + 1.56 \times 10^{-4} T_s - 3.435 \times 10^{-4} T_s^2 \text{ J} / \text{g} \cdot \text{K}$$

$$C_{mat} = 0.6 \text{ J} / \text{g} \cdot \text{K}$$

$$C_{steel} = 0.5023 \text{ J} / \text{g} \cdot \text{K}$$

$$\rho_{monolith} = 0.552 \text{ g} / \text{cm}^3$$

$$\rho_{mat} = 1 \text{ g} / \text{cm}^3$$

$$\rho_{steel} = 7.8 \text{ g} / \text{cm}^3$$

The temperature contours are given in the Figure 5.37 as two columns. The one on the left shows the result of *the reference case* (homogenous noble metal distribution) and the one on the right shows the result of the step-function noble metal distribution. Each row represents the temperature contours at different times. From top to bottom, time levels are 10, 20, 30, 40, 60 and 80 seconds. Each plot has the same color code varying from 350K to 1000K changing with 25K steps. The maximum temperature at the inlet might go up to 1300K, which is lower than that of one-dimensional model as expected. Temperatures that are higher than 1000K are shown in red color.

During the first 20s, the main heat transfer mechanism for *the reference case* is the heat conduction and the convection along the converter. The hot exhaust gas warms up the inlet region faster than the outlet region. The magnitude of the inflow velocity is higher near the symmetry line and gets lower along the vertical direction. Since the hot gas transport, due to a larger velocity, is more around the symmetry line, the relatively high temperatures around the inlet region of the symmetry plane are observed at the initial times. The temperature decreases along the vertical direction. This characteristic continues until the surface temperature gets as high as the exhaust gas temperature at the inlet (600K) to activate the surface chemistry. Once the surface chemistry is activated starting from the inlet, this energy is convected to the downstream faster for the channels with a higher velocity. Therefore, the higher surface temperature occurs around the outlet (see Figure 5.37 for times of 30 and 40s.) At these time slots, the heat transfer along vertical direction becomes significant. At the time of 50s, the temperature peak occurs around the fifth row. The channels with lower velocity have a tendency to warm up the surface locally since heat is not transported from the surface to the exhaust gas as quickly as the channels with higher flow velocity. Temperature peak at 80s is around 1/4 of the converter length from the inlet, at the fifth row in the vertical direction.

In the second column, the temperature contours are given at the same time level as *the reference case* so that we can compare the change in the temperature caused by the step-function noble metal distribution. All the phenomena that was observed during the first 60s of temperature contours of *the*

reference case, is observed during the first 30s of the step-function distribution. Temperature peak occurs at the fifth vertical station at the inlet. As time goes on, the surface temperature of the monolith reaches the highest value at the inlet.

We can further investigate whether the temperature contours become similar to each other at the steady state for these two cases. In Figure 5.38, temperature contours for both cases are given at 240s. They are quite similar to each other. Therefore, although the step-function noble metal speeds up the monolith warming, the value and the location of the temperature peak remain the same for the steady state conversions. The above results of the two-dimensional axisymmetric model are in a very good agreement with the results of the one-dimensional study. As time goes on from the start of the exhaust gas inflow, the local temperature peak moves from the symmetry line to the external levels, getting closer to the inlet at each level. At the steady state, the temperature peak is at the inlet and away from the center of the converter.

The *CO*-conversion curves from the two-dimensional calculations for both cases are shown in Figure 5.39. Since the inflow velocity differs along the vertical direction, the weighted average of the *CO*-conversion is used to calculate overall *CO*-conversion. The weighted average is defined as

$$CE_{CO}^{overall} = \sum \frac{V_i \times C_{CO,i}^*}{V_i} ,$$

where V_i is the inflow velocity at row i and $C_{CO,i}^*$ is the molar fraction of the emission of the carbon monoxide. The step-function distribution gives 31% better conversion compared to the reference case.

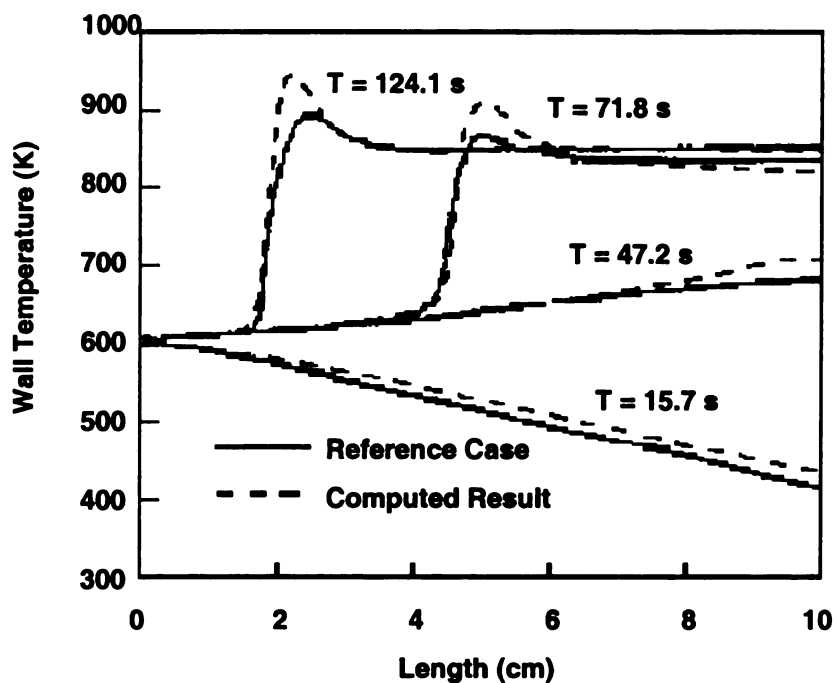


Figure 5.1 The monolith temperature for various times. Solid line result is taken from Oh *et al.*[1982]

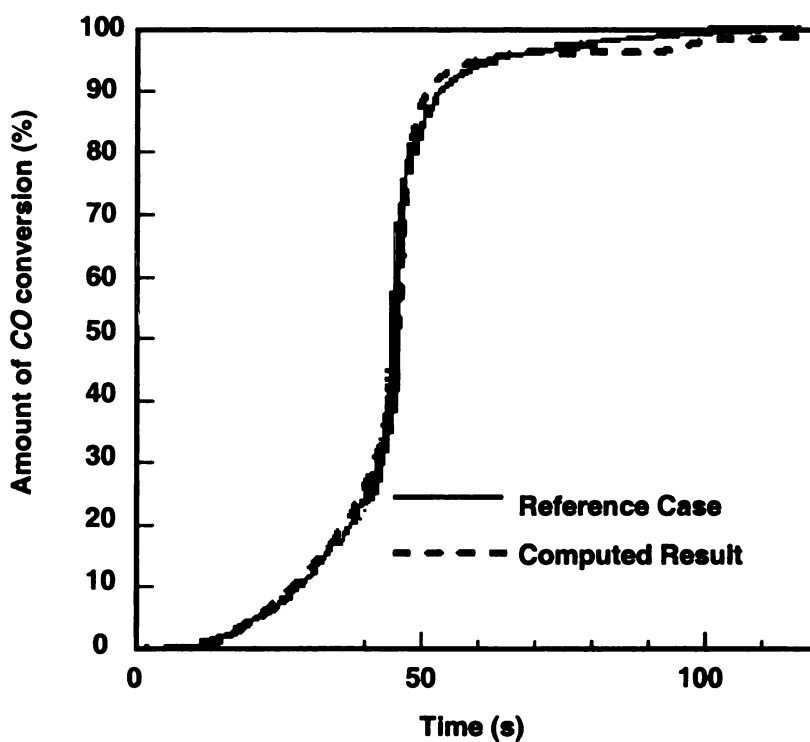


Figure 5.2 The CO-conversion efficiency for warm-up period. Solid line is taken from Oh *et al.*[1982]

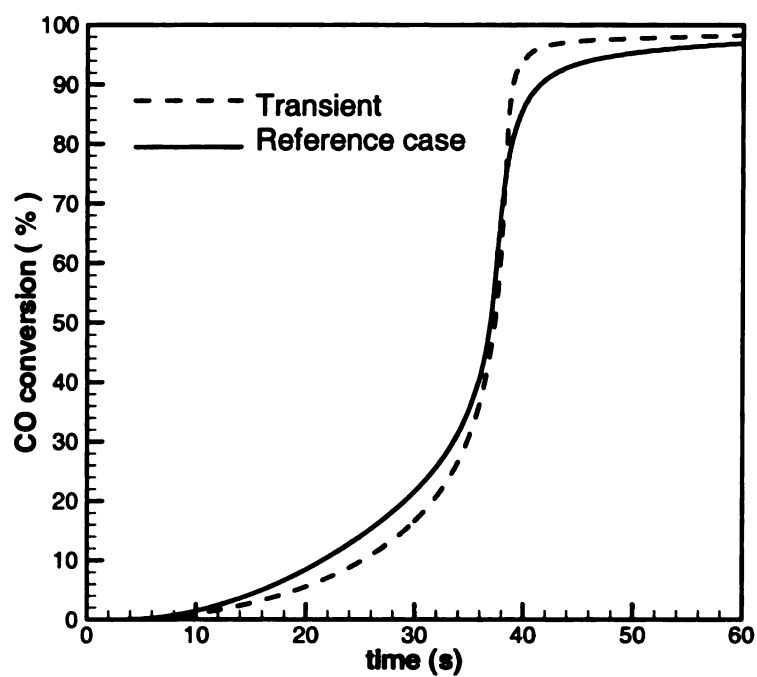


Figure 5.3 The CO -conversion for the reference case and the case with transient term.

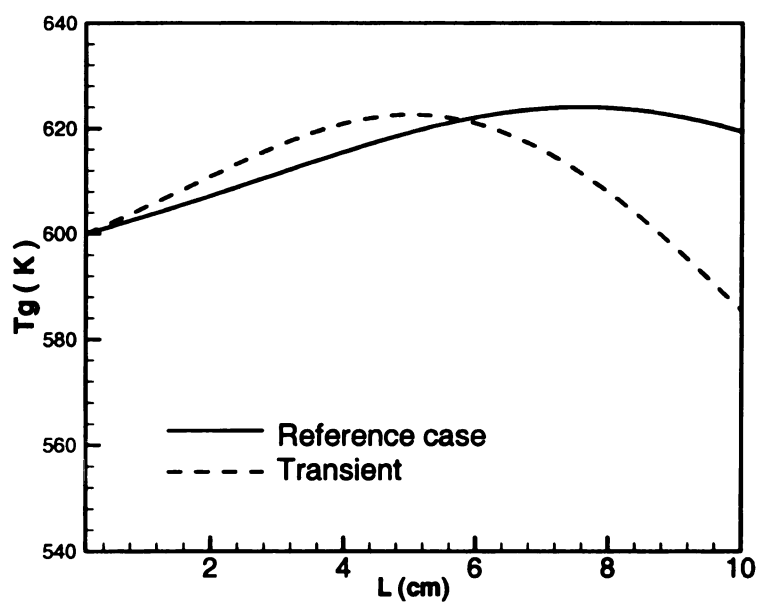


Figure 5.4 The gas temperature distribution along the monolith at 30s.

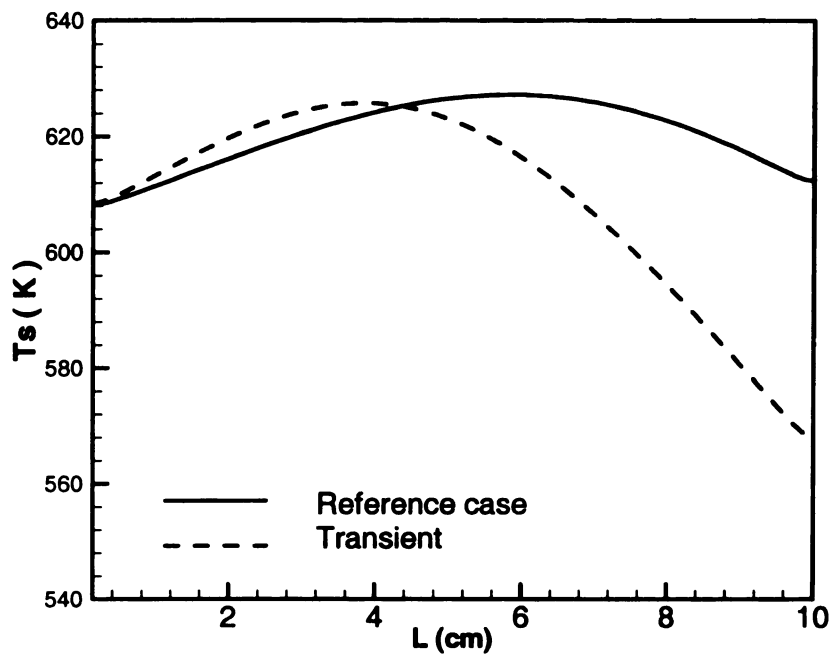


Figure 5.5 The surface temperature distribution along the monolith at 30s.

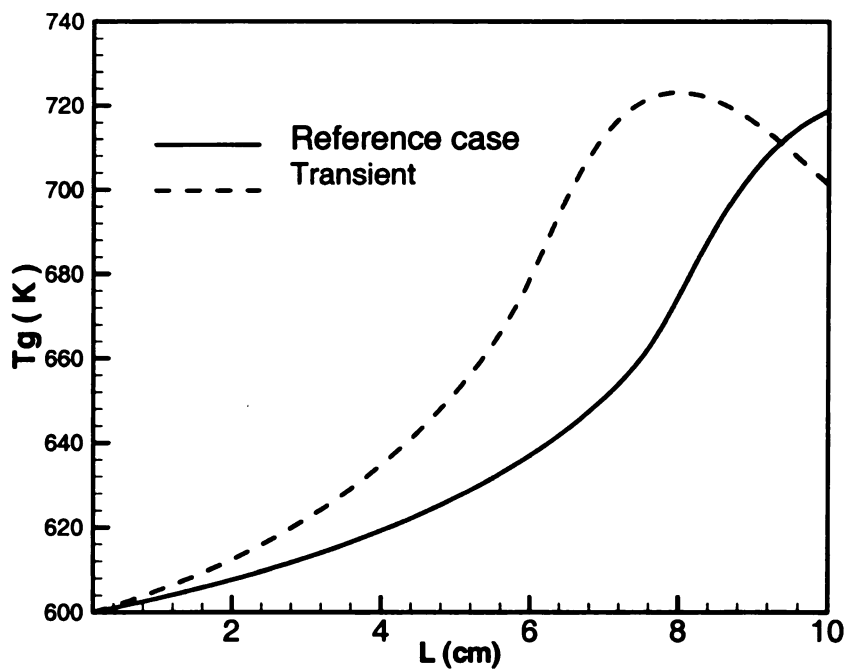


Figure 5.6 The gas temperature distribution along the monolith at 40s.

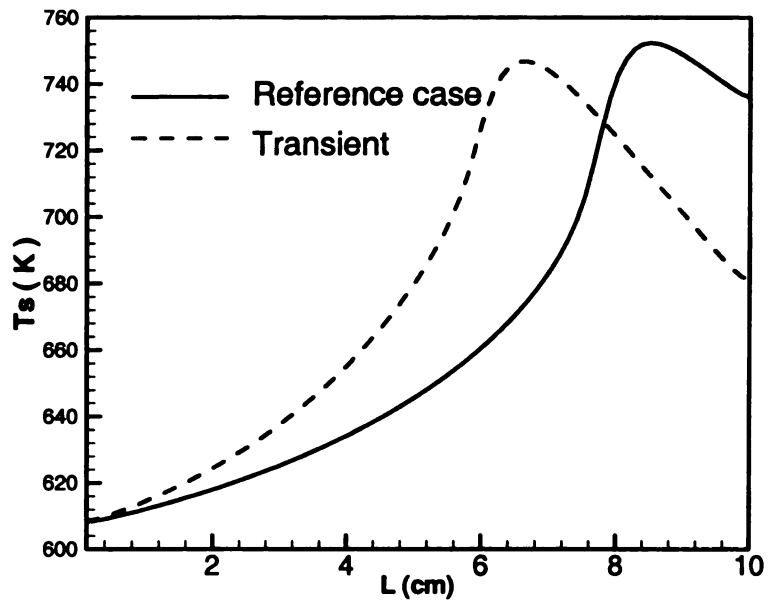


Figure 5.7 The surface temperature distribution along the monolith at 40s.

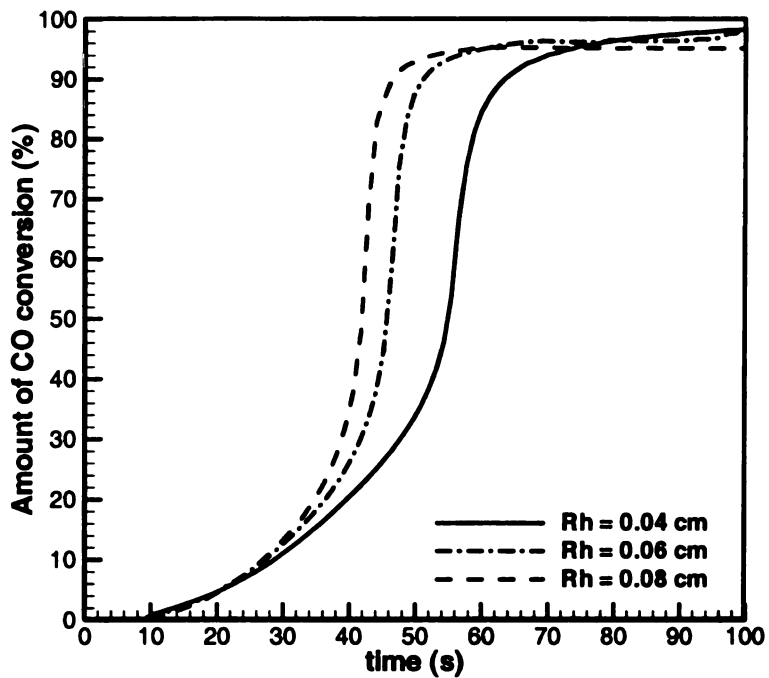


Figure 5.8 The CO-conversion curves for a converter with constant void area and different channel radius (different cell densities)

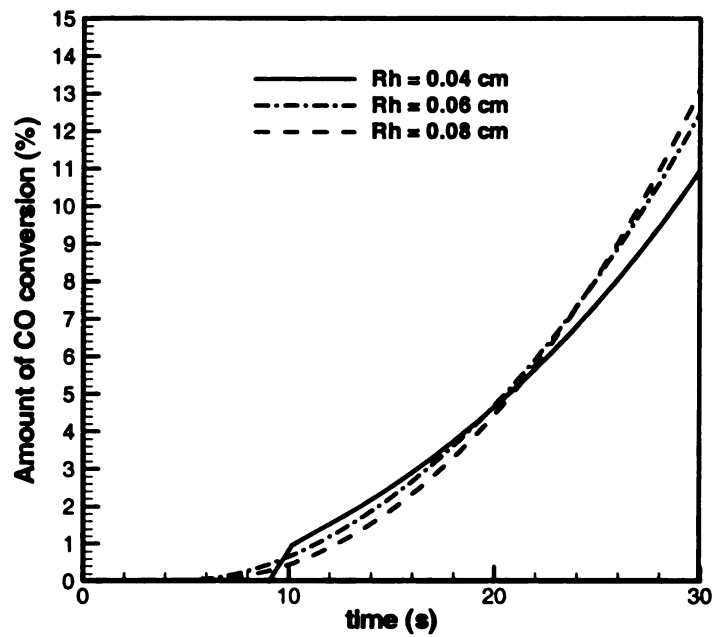


Figure 5.9 The enlarged view of the first 30s of the Figure 5.8.

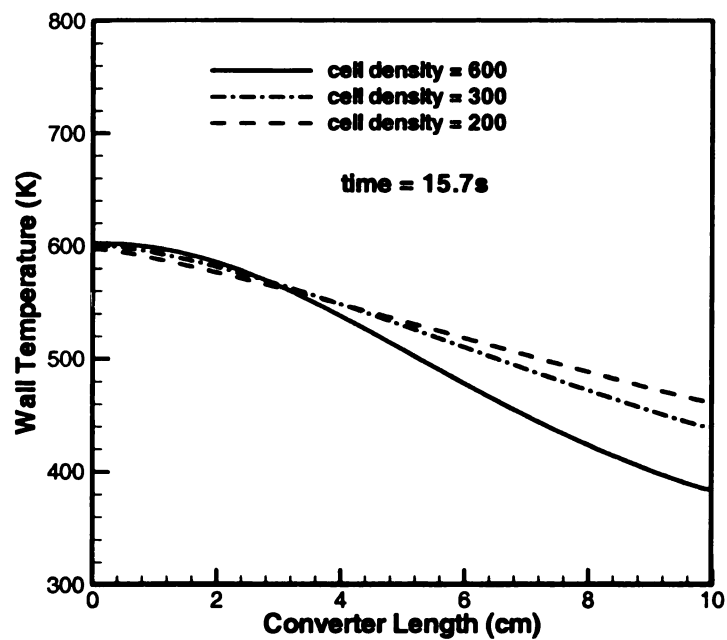


Figure 5.10 The wall temperature along the monolith at 15.7 s for different cell densities.

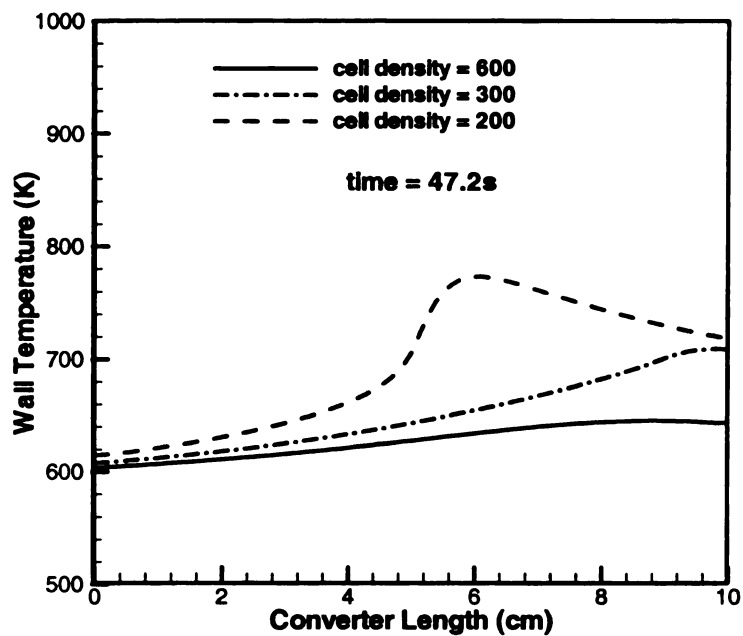


Figure 5.11 The wall temperature along the monolith at 47.2 s for different cell densities.

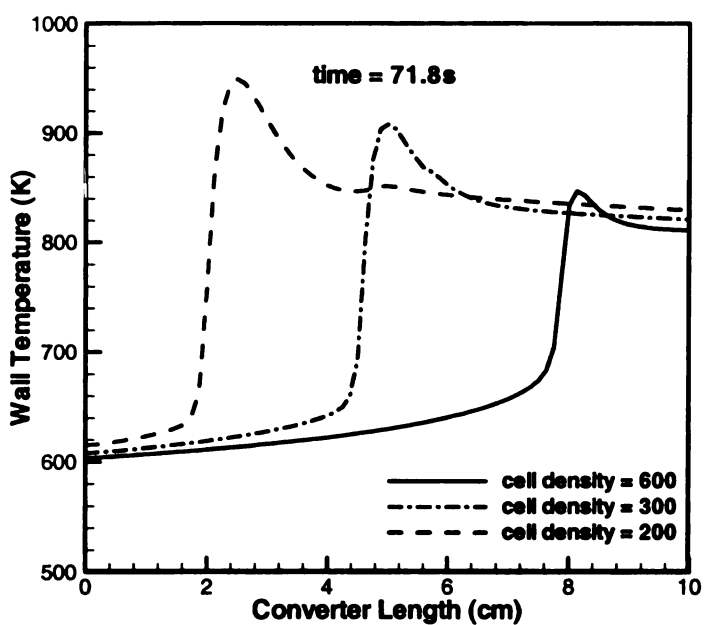


Figure 5.12 The wall temperature along the monolith at 71.8 s for different cell densities.

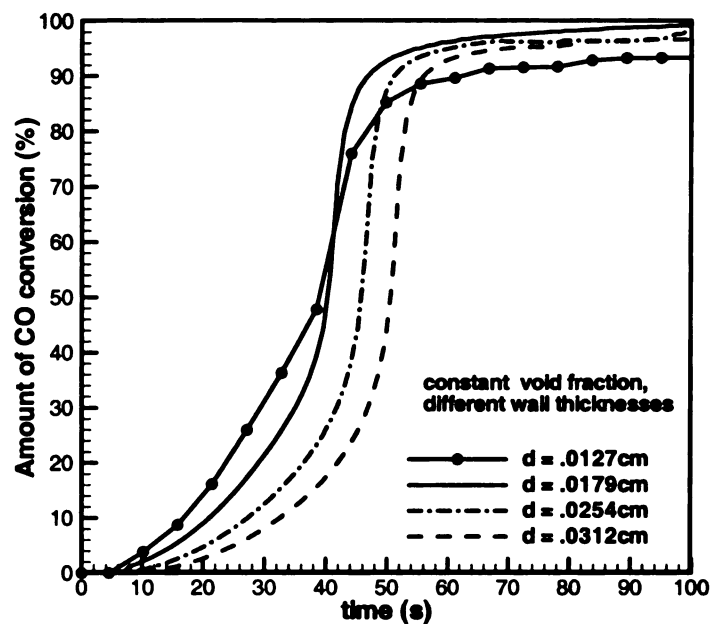


Figure 5.13 The CO-conversion curves for different wall thickness values.

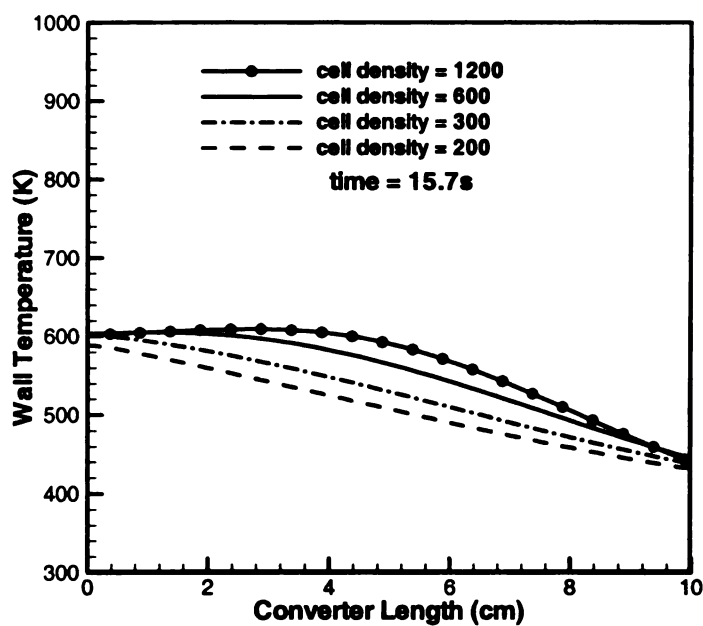


Figure 5.14 The monolith wall temperature along the monolith at 15.7 s for different wall thickness values.

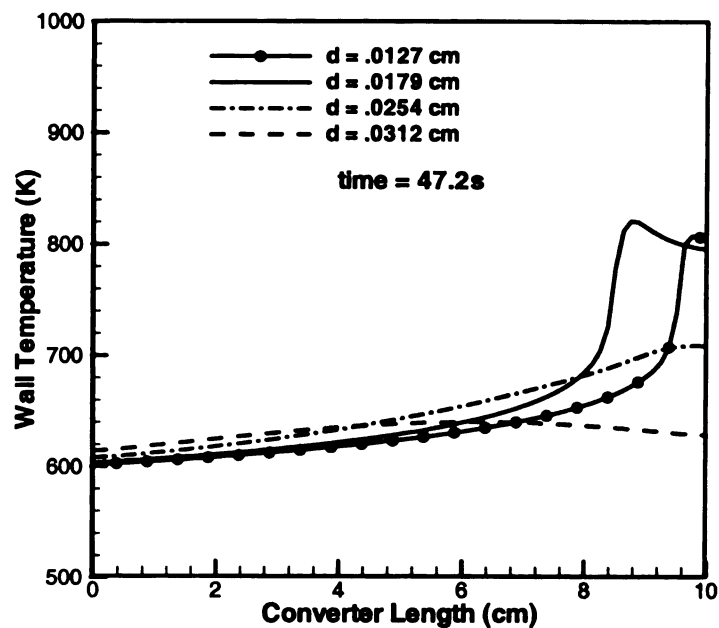


Figure 5.15 The temperature along the monolith at 47.2 s for different wall thickness values.

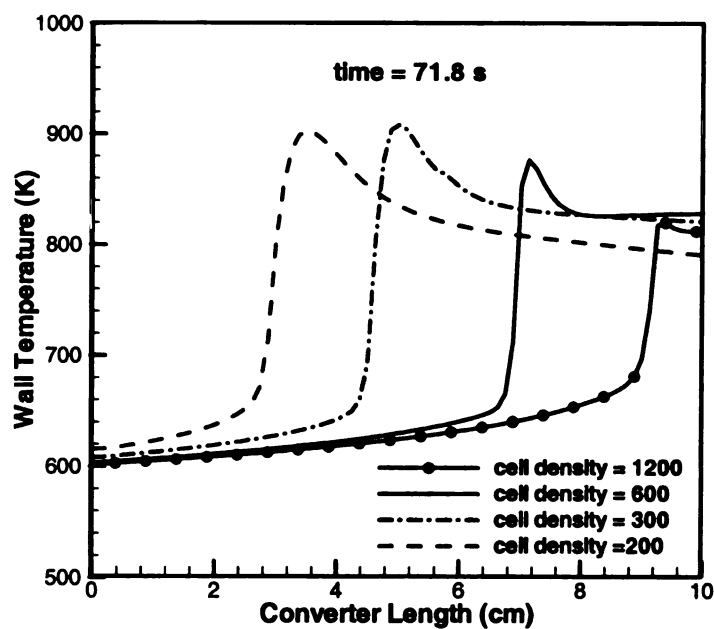


Figure 5.16 The temperature along the monolith at 71.8 s for different wall thickness values.

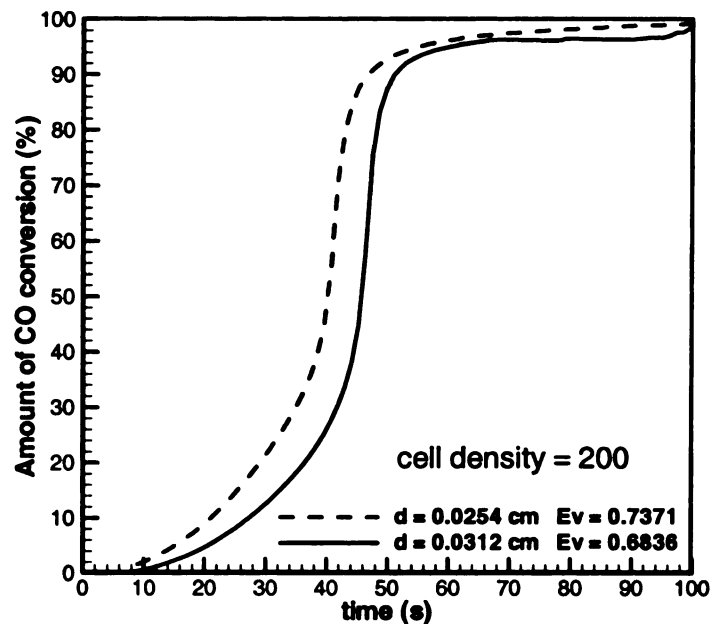


Figure 5.17 The amount of CO -conversion curves for 200 cell/in² (Ev represents the values of the void fraction).

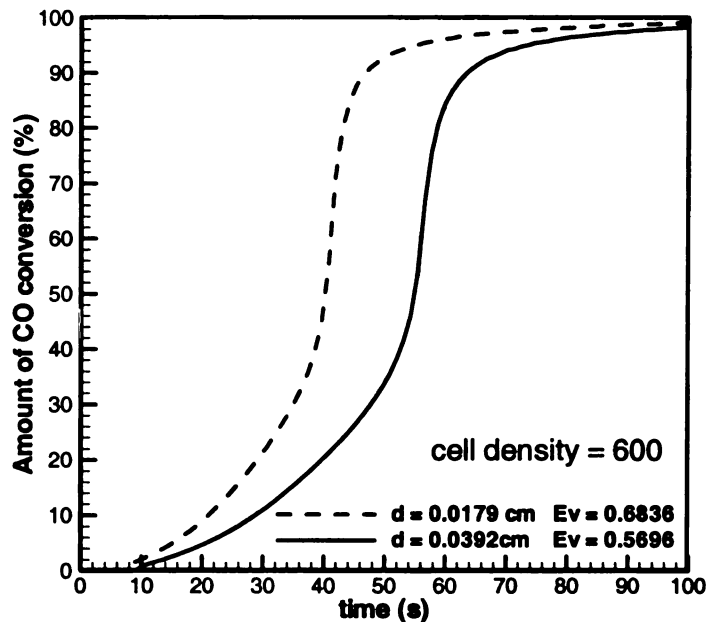


Figure 5.18 The amount of CO -conversion curves for 600 cell/in²

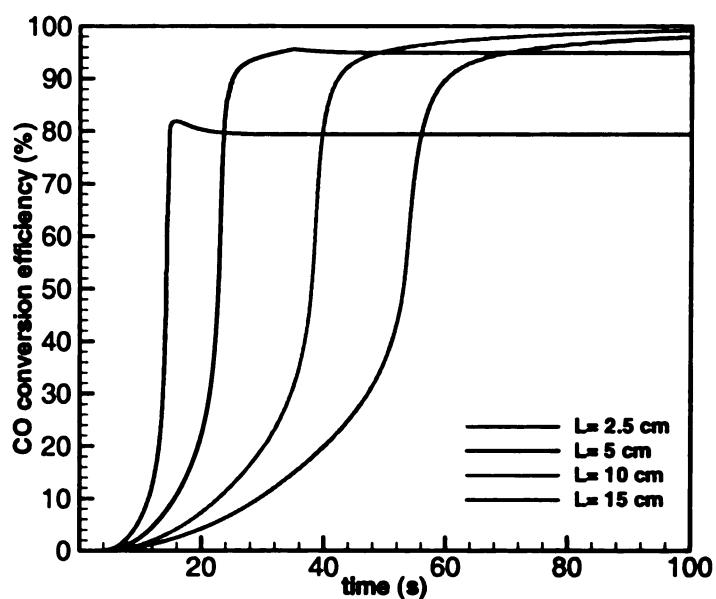


Figure 5.19 The CO-conversion curves for different converter length, $a(x)L = 2689 \text{ cm}^2 / \text{cm}^3$.

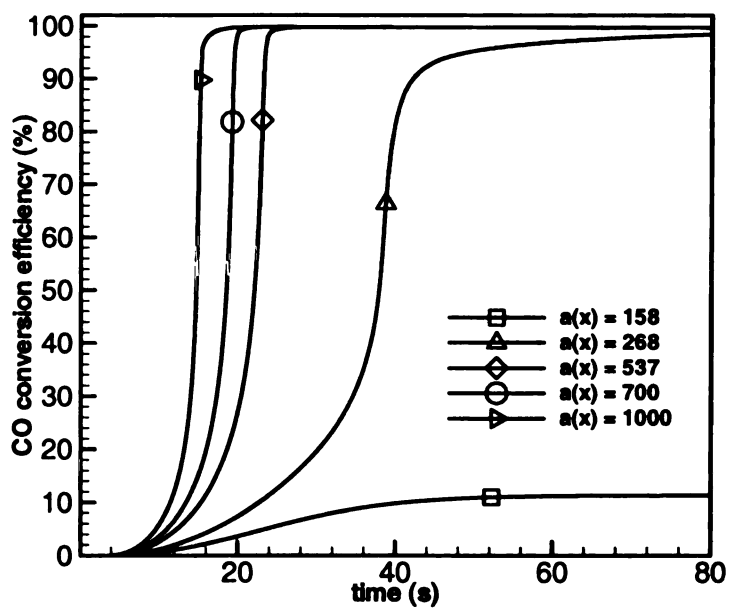


Figure 5.20 CO-conversion curves for a converter of length 10cm with different $a(x)$ (in $\text{cm}^2 \text{Pt} / \text{cm}^3$) values.

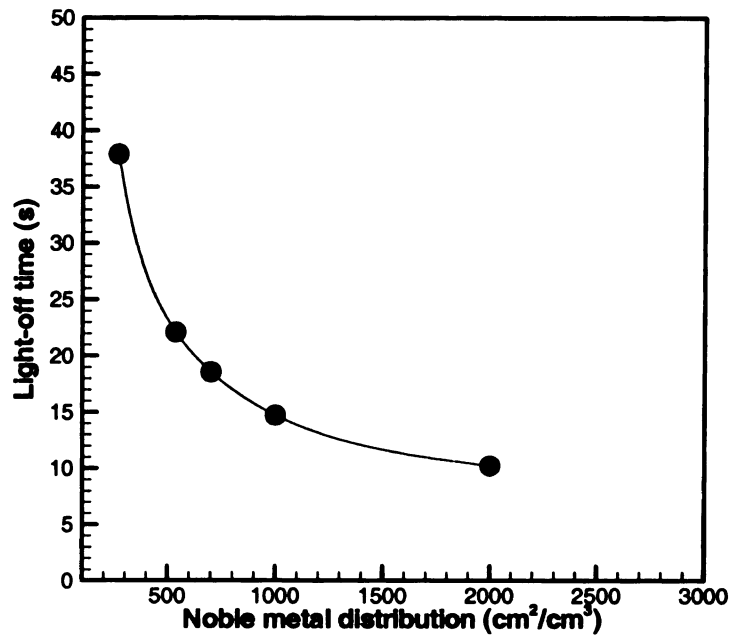


Figure 5.21 The light-off time values for a converter of length 10cm with different $a(x)$ values

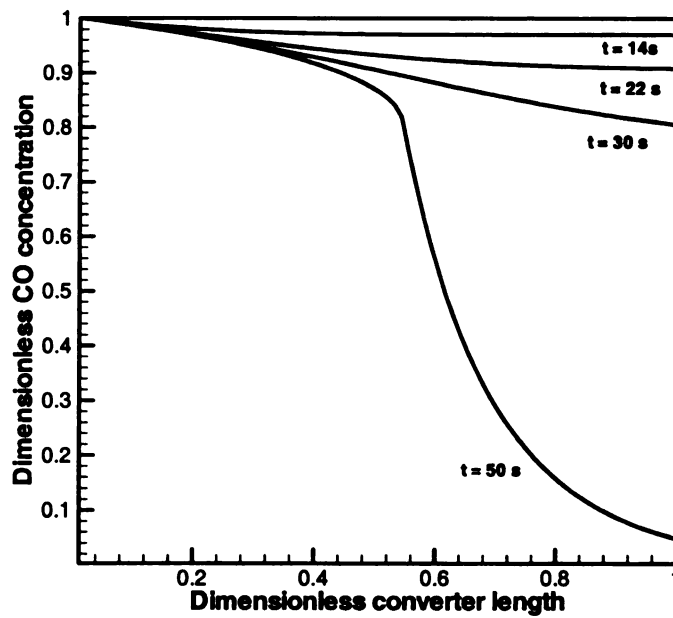


Figure 5.22 Dimensionless CO concentration along the converter for $a(x) = 268.39 \text{ cm}^2/\text{cm}^3$

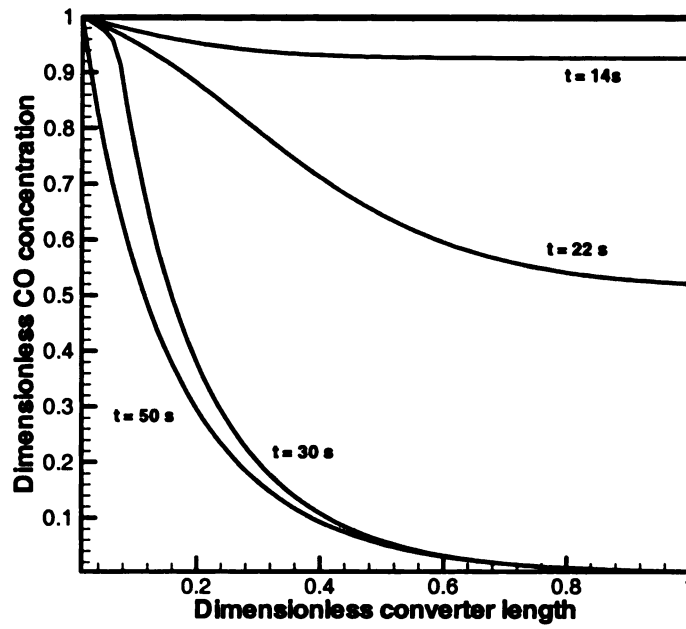


Figure 5.23 Dimensionless CO -concentration along the converter for $a(x) = 537.68 \text{ cm}^2 / \text{cm}^3$

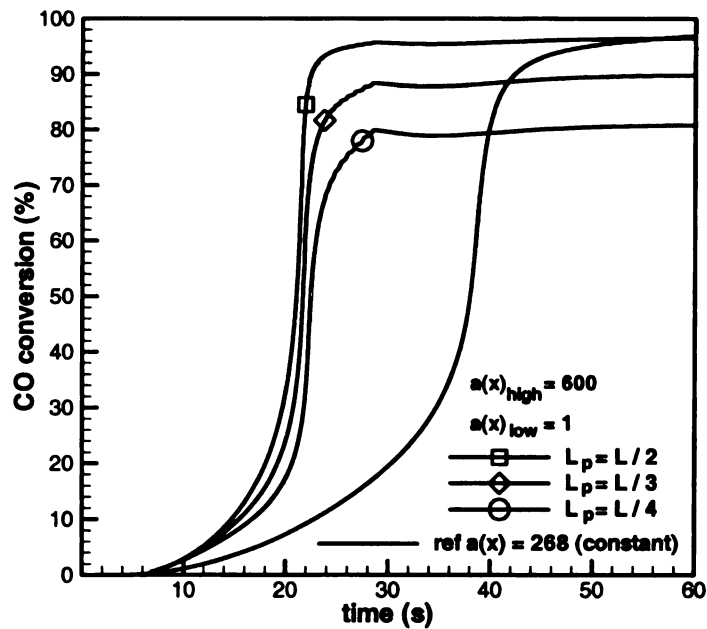


Figure 5.24 The CO -conversion for step-function noble metal distribution for different high concentration lengths, $a(x)$ (in $\text{cm}^2 \text{Pt} / \text{cm}^3$)

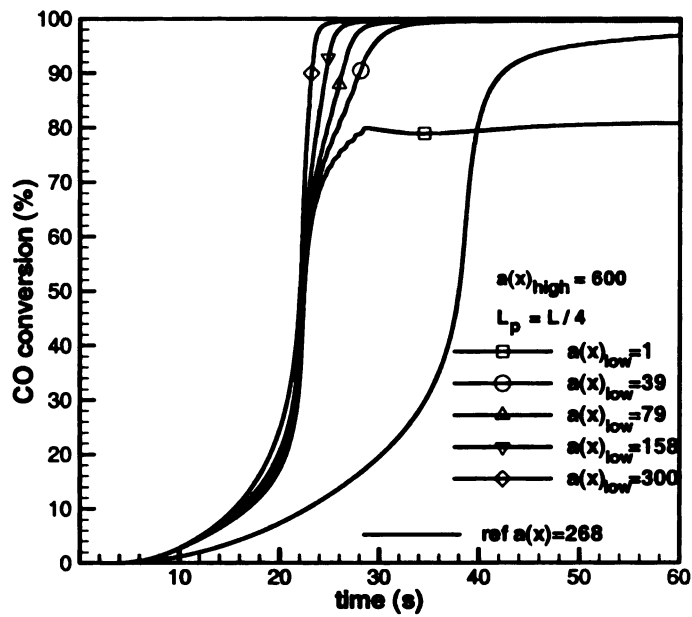


Figure 5.25 The CO-conversion for the step-function noble metal distribution for different $a(x)_{low}$ (in $\text{cm}^2 \text{Pt} / \text{cm}^3$)

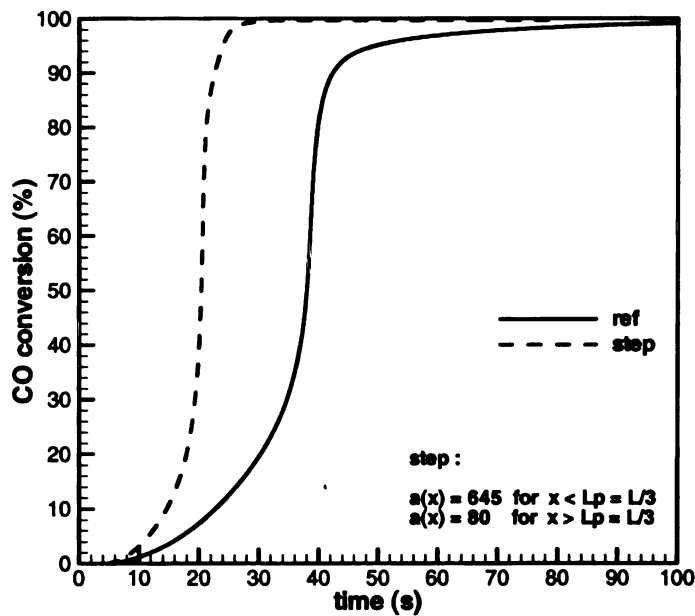


Figure 5.26 The CO-conversion for the (homogenous) reference case and the step-function noble metal distribution.

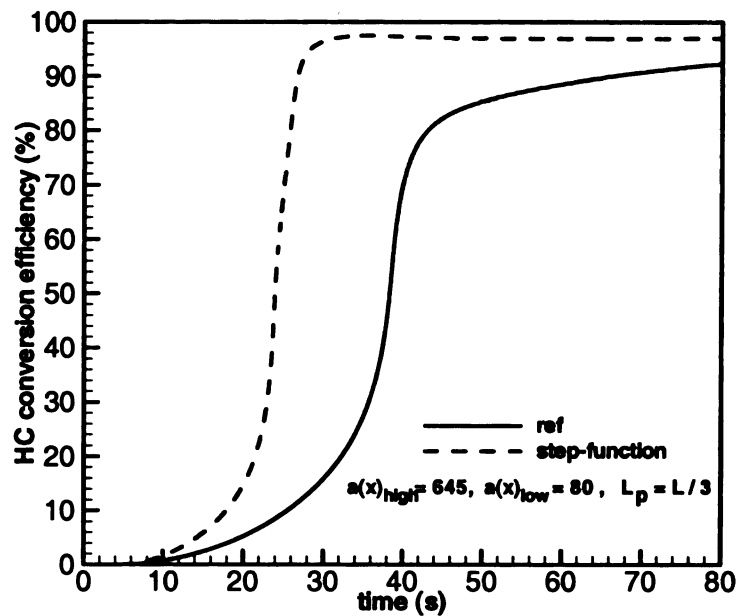


Figure 5.27 The *HC* conversion for the (homogenous) reference case and the step-function noble metal distribution.

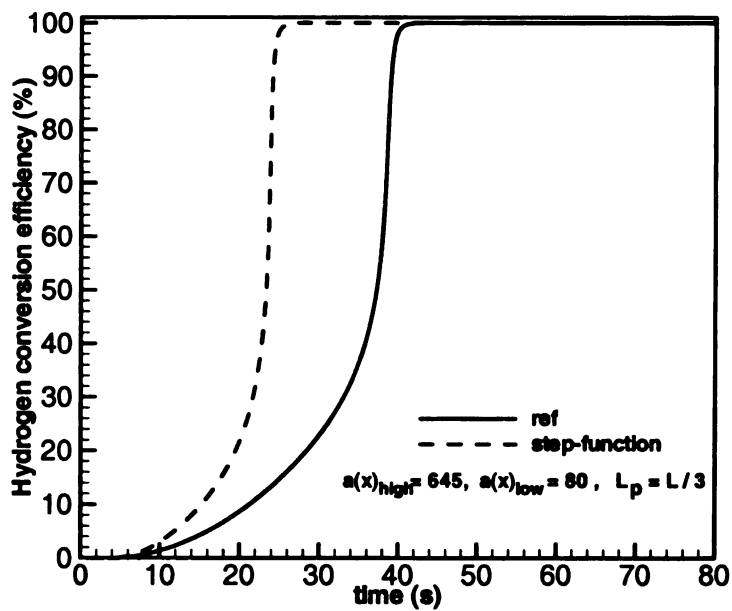


Figure 5.28 The hydrogen conversion for the (homogenous) reference case and the step-function noble metal distribution.

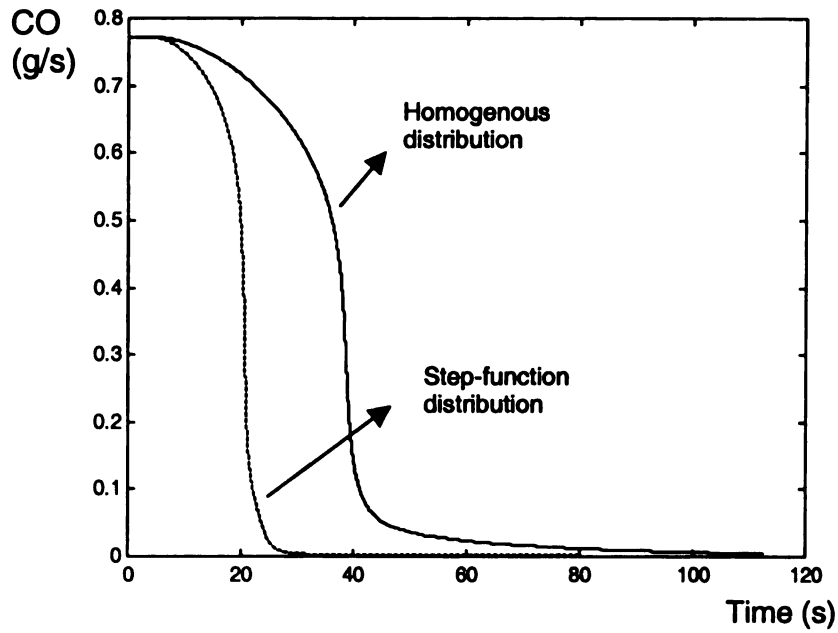


Figure 5.29 The CO-emission in g/s for the (homogenous) reference case and step-function noble metal distribution

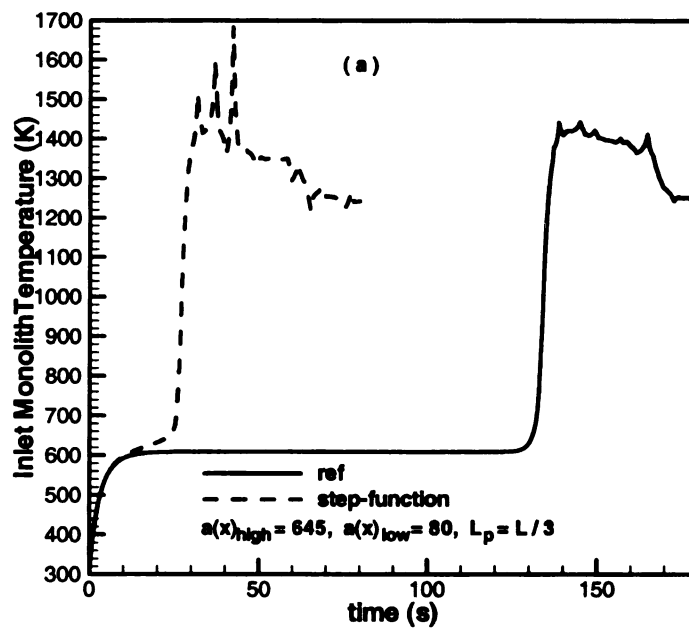


Figure 5.30 Inlet surface temperature for the reference case and the step-function noble metal distribution.

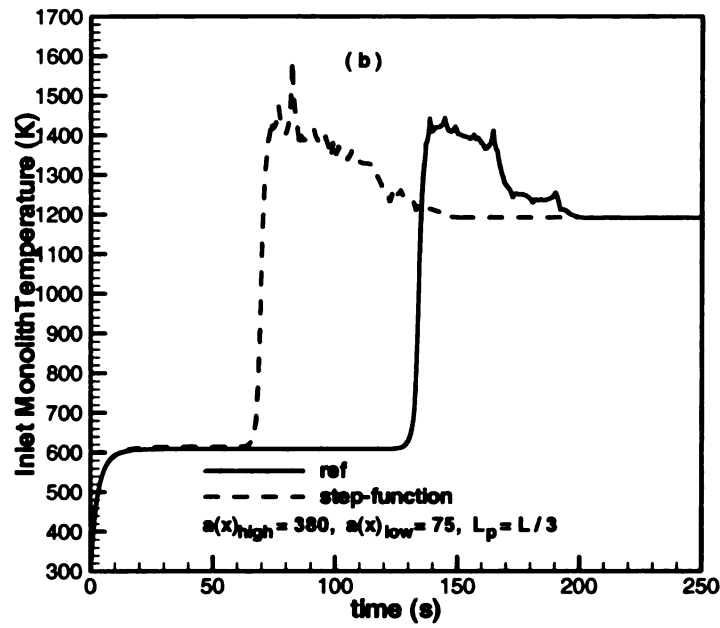


Figure 5.31 The outlet temperature for the reference case and the step-function noble metal distribution.

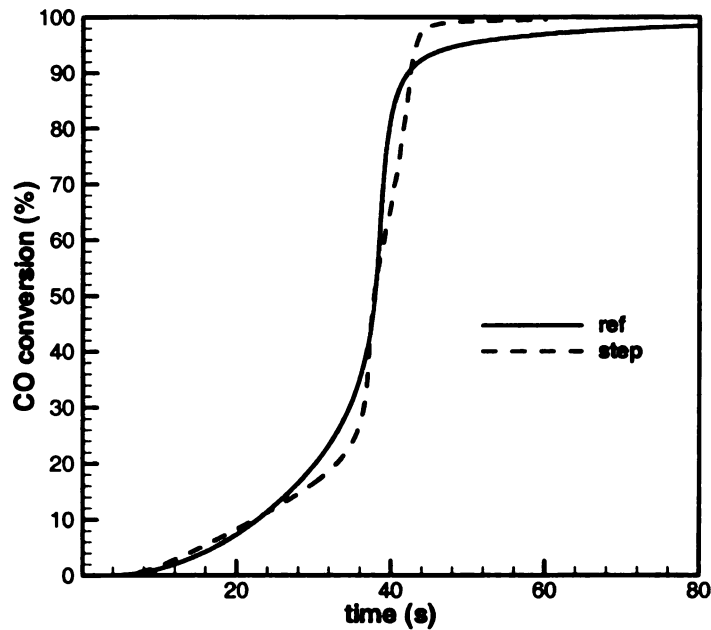


Figure 5.32 The CO-conversion for the reference case and the step-function noble metal distribution.

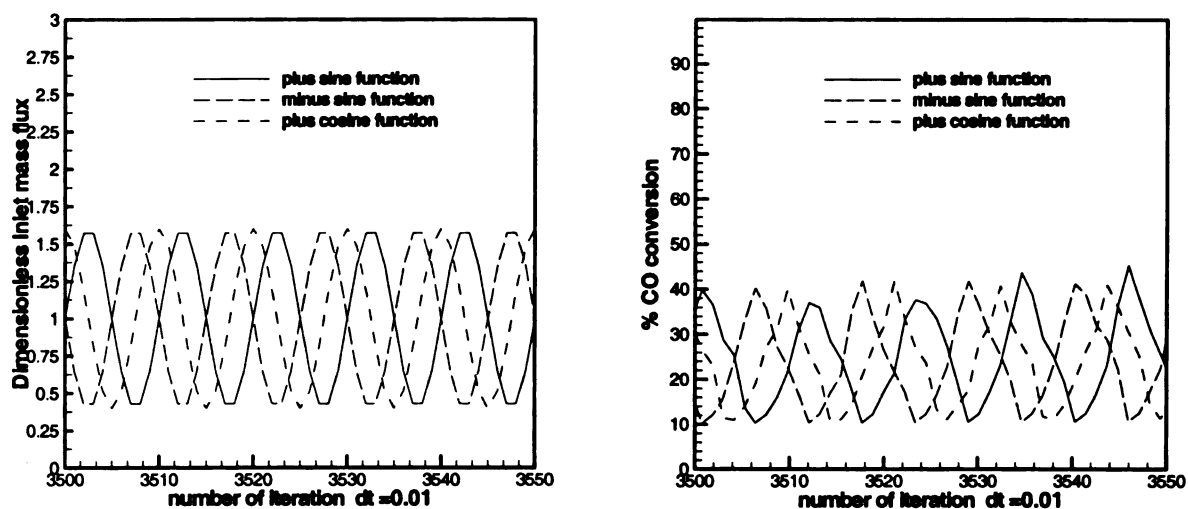


Figure 5.33 The effect of inflow-oscillations on CO -conversion efficiency

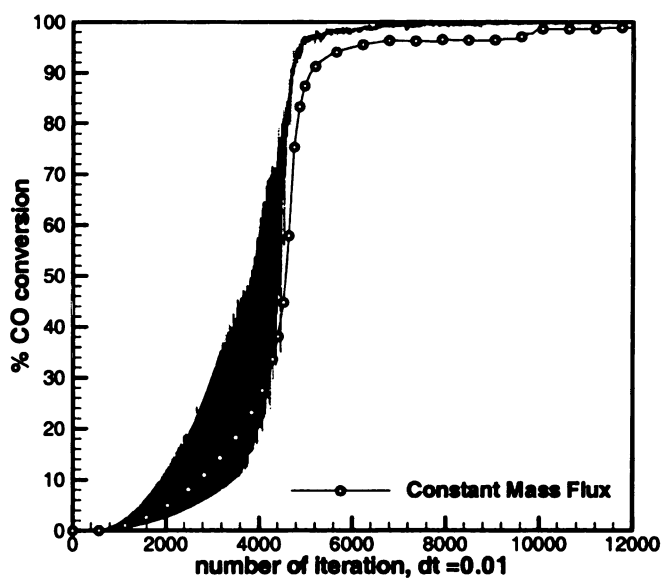


Figure 5.34 CO -conversion efficiency for constant mass flux and time dependent mass flux cases.

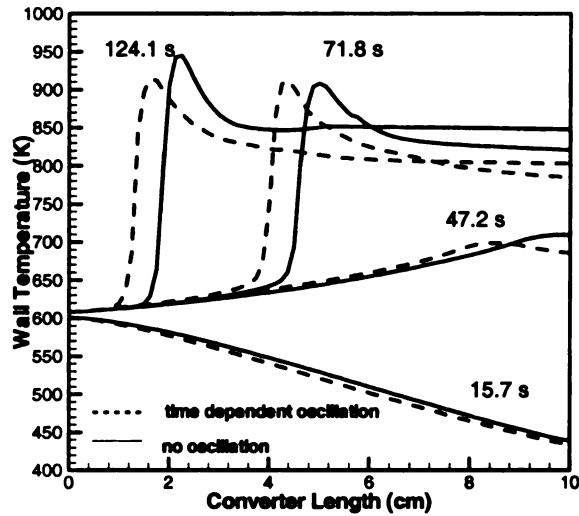


Figure 5.35 Comparison of the monolith wall temperature at different times for the oscillatory and constant inlet mass flux cases.

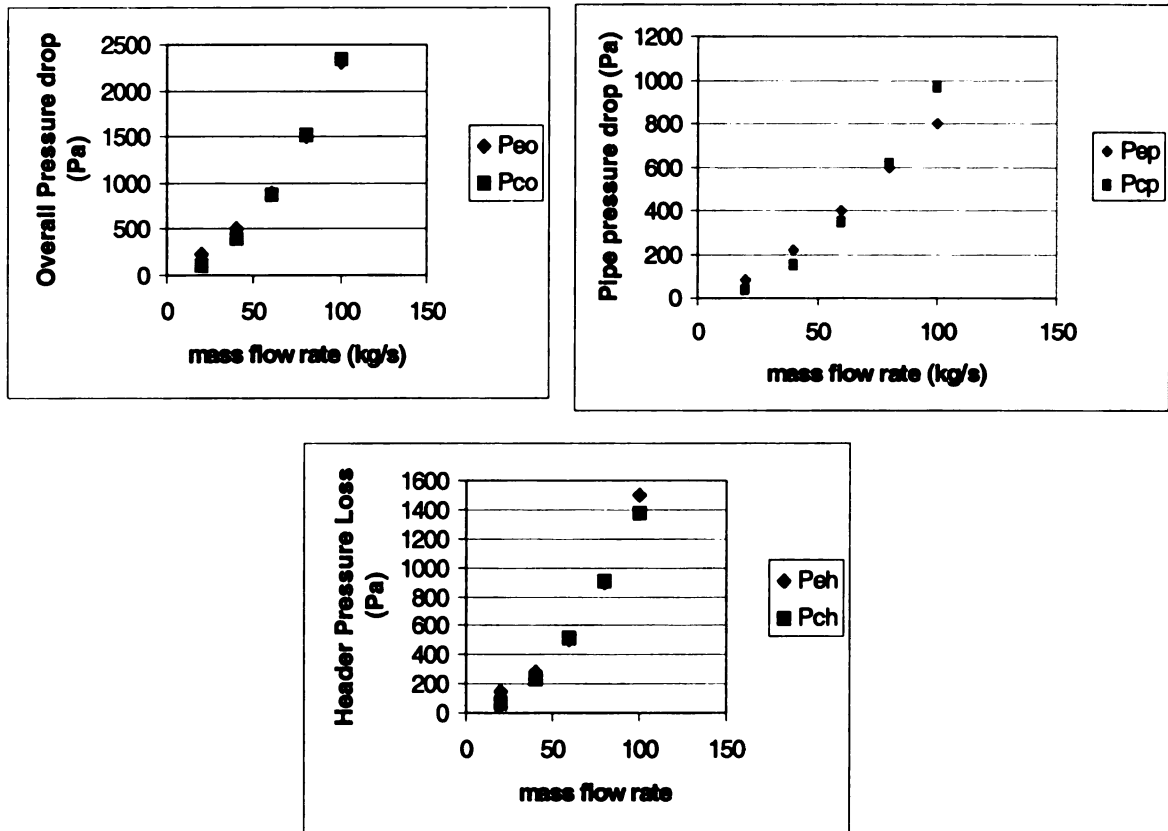


Figure 5.36 Pressure loss for different mass flow rate cases.

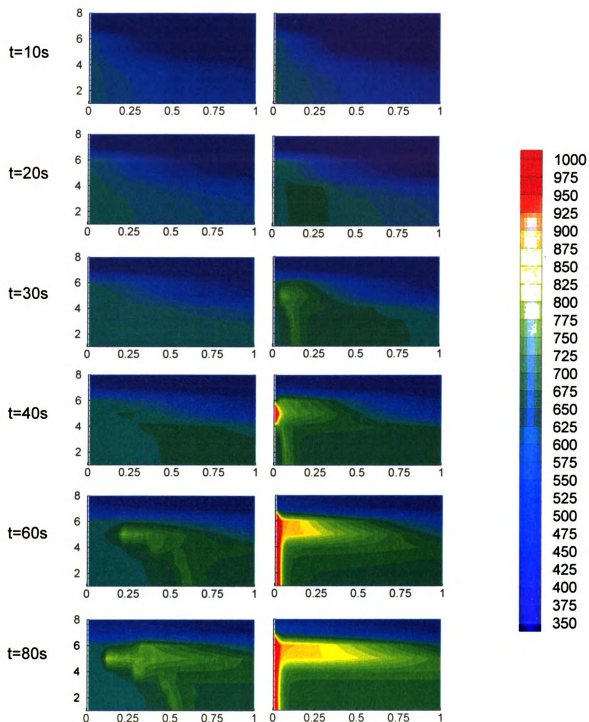


Figure 5.37 Temperature contours for different times of the (homogenous) reference case (left column) and the step-function noble metal distribution (right column)

(images in this figure are presented in color)

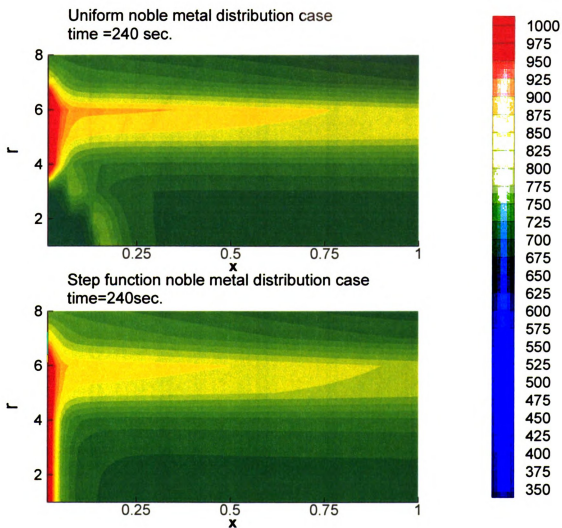


Figure 5.38 Temperature contours of the (homogenous) reference case (left column) and the step-function noble metal distribution (right column) at 240s.

(images in this figure are presented in color)

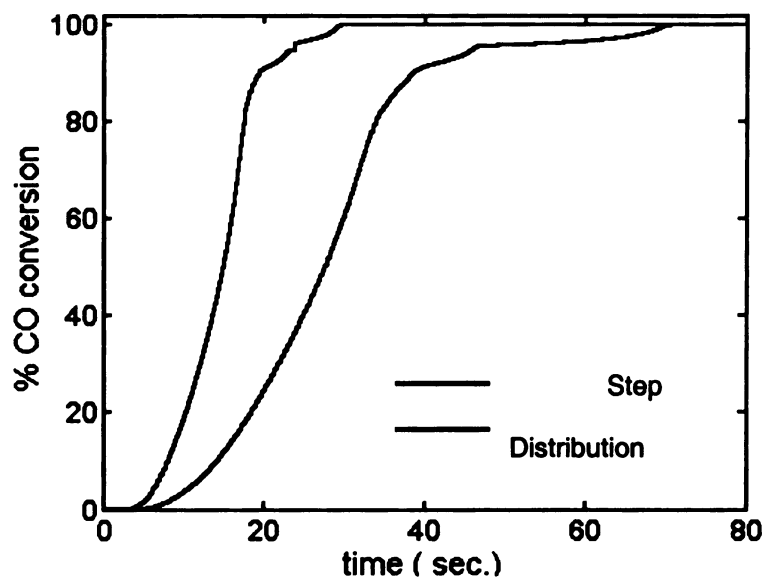


Figure 5.39 *CO*-conversion efficiency curves for step-function and (homogeneous) reference case noble metal distributions for axisymmetric model

Chapter 6

CONCLUSION

The objectives of this study are to investigate the heat transfer, the mass transfer, the chemical reactions and the fluid flow inside the catalytic converter and to develop criteria to improve the conversion efficiency of the catalytic converter, especially at the cold-start regime. This is accomplished by a systematic study of a model by Oh *et al.*[1982] to understand the factors that significantly affect the catalytic converter performance.

First, our one-dimensional model in this study is validated with existing and experimentally verified numerical results of Oh *et al.* Secondly, the effect of the transient terms in the heat and the mass conservation equations of the gas phase on the conversion efficiency are studied. Although there is a difference between the quasi-transient case and the fully transient case results, the quasi-transient approach to model the mass and the energy balance equations for the gas phase gives quite realistic results in terms of the integral conversion efficiency in the cold-start regime.

The effect of geometry is investigated by using different values for the parameters of the cell density, the wall thickness and the converter length. Their

effects on the conversion efficiency curve and the light-off time are studied.

Based on these results our conclusions are

1. the cell density (cd), the wall thickness, the channel radius and the converter length are important design parameters that affect the conversion efficiency and the light-off time;
2. for a given wall thickness, increasing channel radius (i.e. decreasing cd) shortens the light-off time, however this might result in a decrease in the steady state conversion;
3. for a given void fraction, decreasing wall thickness (i.e. increasing cd), shortens the light-off time, however this might result in a decrease in the steady state conversion, as well ;
4. there is an optimum value for the converter length for a given amount of the noble material.

We conclude that the early attainment of high surface temperature (high enough to activate the surface chemistry around 650K) is necessary to have better conversion efficiency.

The study on the effect of the noble metal, Pt , distribution showed that, with higher amount of catalyst, the surface chemistry is activated earlier. This has two important results:

1. The light-off time is an exponentially decreasing function of the noble metal (Pt) concentration.
2. The amount of the catalyst necessary in the monolith around the outlet is much less than the inlet region of the monolith.

Based on these results, a step-function noble metal distribution (Section 5.5.2, Schema 5.1) is proposed. The study in this section has also two important results:

1. For a given amount of the noble metal, the light-off time is shortened by approximately 35% with step-function distribution and therefore the emissions are significantly reduced.
2. The cost of the noble metal catalysts used in catalytic converters can be reduced when using the step-function noble metal distribution while keeping the emissions the same as that of the homogeneous distribution.

The qualitative criterion to choose a step-function distribution based on the noble metal concentration versus light-off time graph is given.

The one-dimensional model is modified to the two-dimensional axisymmetric model to study the effect of the inflow velocity variation on the maximum monolith temperature, by using representative monolith channels stacked in the vertical direction. The step-function noble metal distribution does not change the temperature distribution qualitatively compared to the

homogenous noble metal distribution. However, it speeds up the warming process. The steady state temperature profiles of both cases are very similar.

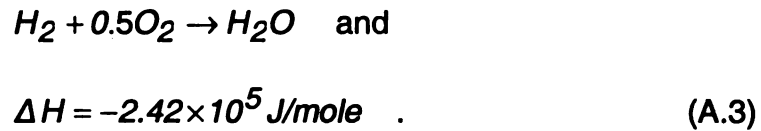
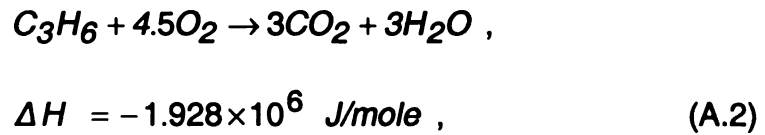
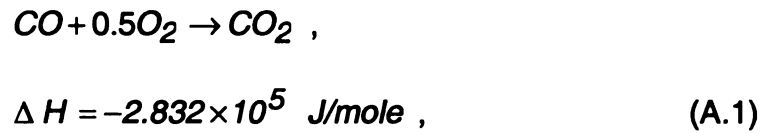
The results of the flow oscillation study show that the oscillatory nature of the inlet mass flux has an effect on the conversion efficiency during the warm-up period. It is shown that the *CO* conversion efficiency at the converter exit oscillates as a result of the inlet mass flow rate oscillation. However, the mechanism relating these two oscillations is still not clear. A further study in this area could provide useful information on how to control the inlet exhaust flow oscillations so that better conversion efficiency can be achieved during the warm-up period.

APPENDICES

APPENDIX A

CHEMISTRY MODEL

In the present study, the chemistry model of Oh et al. [1982] is used. The chemical reactions and their heat of reactions for the model are



The specific rates R_i (rates per unit Pt surface area) for the oxidation of CO , C_3H_6 and H_2 can be expressed as functions of solid phase concentrations $C_{s,i}$ and temperature T_s :

$$R_{CO} = k_1 C_{s,CO} C_{s,O_2} / G \quad (A.4)$$

$$R_{C_3H_6} = k_2 C_{s,C_3H_6} C_{s,O_2} / G \quad (A.5)$$

$$R_{H_2} = k_1 C_{s,H_2} C_{s,O_2} / G \quad (A.6)$$

where

$$G = T_s \left(1 + K_1 C_{s,CO} + K_2 C_{s,C_3H_6} \right)^2 \times \left(1 + K_3 C_{s,CO}^2 C_{s,C_3H_6}^2 \right) \times \left(1 + K_4 C_{s,NO}^{0.7} \right) \quad (A.7)$$

$$k_1 = 6.699 \times 10^9 \exp(-12556/T_s)$$

$$k_2 = 1.392 \times 10^{11} \exp(-14556/T_s)$$

$$K_1 = 65.5 \exp(961/T_s)$$

$$K_2 = 2.08 \times 10^3 \exp(361/T_s)$$

$$K_3 = 3.98 \exp(11611/T_s)$$

$$K_4 = 4.79 \times 10^5 \exp(-3733/T_s)$$

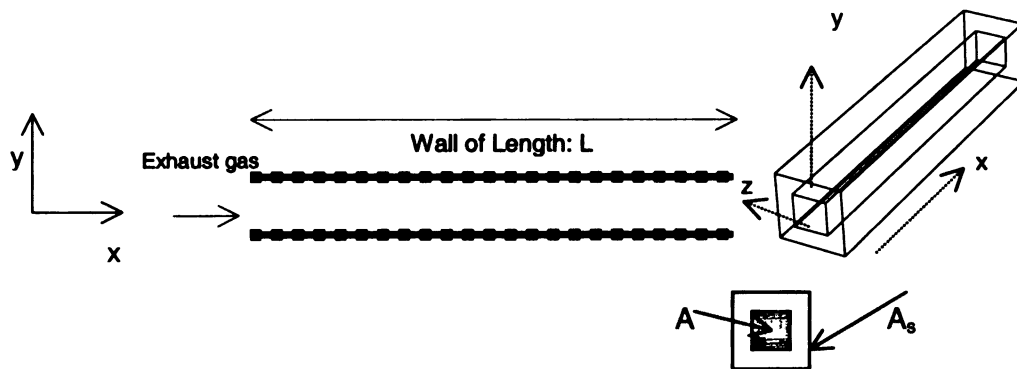
From the stoichiometry, the reaction rate for oxygen must satisfy

$$R_{O_2} = 0.5 R_{CO} + 4.5 R_{C_3H_6} + 0.5 R_{H_2} \quad (A.8)$$

APPENDIX B

BALANCE EQUATIONS

The exhaust gas is considered as a multi-component mixture. It consists of unburned hydrocarbons, combustion products and air. There is no mass transfer through monolith channel walls. The energy and mass balance equations can be written for the solid and gas phase of each component of the exhaust gas for an individual channel. The exhaust gas diffuses through and is adsorbed on the channel walls. If the surface temperature is high enough, surface chemical reaction takes place over the channel surfaces by the help of catalytic noble metal platinum, *Pt*. Schema B.1 shows the control volume for this problem.



Schema B.1 Schematic for the one -dimensional study.

The Material Balance for the Gas-Phase of the Species i :

The mass balance equation for the exhaust gas component i is derived for the given control volume from the fundamental balance equations. The chemical reactions in gas phase are neglected. For simplicity, we will include only one spatial direction:

$$\frac{d(m_{i,cv})}{dt} = [\dot{m}_i^r A]_x - [\dot{m}_i^r A]_{x+\Delta x} + \dot{m}_i^{\sigma} \Theta \quad (\text{B.1})$$

where Θ is the bulk volume and A is the void area perpendicular to the flow direction. The total cross section area is the sum of the void area and the solid wall area, $A_{total} = A + A_s$. $m_{i,cv}$ is the total mass amount of species i within the bulk volume, i.e. $\dot{m}_{i,cv} = \rho_i(\epsilon\Theta)$. \dot{m}_i^r is the mass flux, i.e. $\dot{m}_i^r = \rho_i v_i$, where ρ_i is the density and v_i is the total velocity of species i . And \dot{m}_i^{σ} is the rate of the volumetric mass adsorption of the species i . After replacing these definitions in Equation (B.1) and dividing each term by the bulk volume Θ and taking the limit $\Delta x \rightarrow 0$ gives:

$$\frac{d(\epsilon\rho_i)}{dt} = \frac{\partial}{\partial x}(\epsilon\rho_i v_i) + \dot{m}_i^{\sigma} \quad (\text{B.2})$$

The species velocity, v_i , can become a quite complicated expression that takes into account different modes of diffusion, such as the ordinary diffusion associated with concentration gradients, the thermal diffusion resulting from temperature gradients, the pressure diffusion resulting from pressure gradients,

and the forced diffusion resulting from unequal body forces per unit mass among the species.

Mass average bulk velocity can be defined as

$$V_b = \sum \left(\frac{m_i}{m_b} v_i \right) , \quad (\text{B.3})$$

and diffusion velocity is defined as

$$v_{i,diff} \equiv v_i - V_b \quad (\text{B.4})$$

therefore, $v_i \equiv V_b + v_{i,diff}$.

Using this relation in Equation (B.2) and dividing by void fraction ε gives

$$\frac{d\rho_i}{dt} + \frac{\partial}{\partial x} [\rho_i V_b] - \frac{\partial}{\partial x} [\rho_i v_{i,diff}] = \frac{\dot{m}_i'''}{\varepsilon} . \quad (\text{B.5})$$

The third term in Equation (B.5) is expressed by Fick's Law

$$(\rho_i v_{i,diff}) = D_{i,k} \frac{\partial \rho_i}{\partial x} , \quad (\text{B.6})$$

where $D_{i,k}$ is the mass diffusivity coefficient of the species i into the mixture k with units of length squared per unit time. It includes the combined effect of all previously mentioned modes of diffusion.

$$\frac{d\rho_i}{dt} + \frac{\partial}{\partial x} [\rho_i V_b] - \frac{\partial}{\partial x} \left[D_{ik} \frac{\partial}{\partial x} \rho_i \right] = \frac{\dot{m}_i''}{\varepsilon} \quad (\text{B.7})$$

To simplify and to express the above equation in terms of the mole fractions, the following expression is also used in Equation (B.7).

$$\rho_i = \frac{m_i}{m_{\text{tot}}} \rho_g = C_{g,i} \frac{MW_i}{MW_g} \rho_g \quad (\text{B.8})$$

Here, ρ_g and MW_g are the density and the molecular weight of the exhaust gas, MW_i and $C_{g,i}$ are the molecular weight and the molar fraction of the exhaust gas component i .

$$C_{g,i} \left(\frac{\partial \rho_g}{\partial t} + \frac{\partial}{\partial x} (\rho_g \mathbf{V}) \right) + \rho_g \frac{\partial C_{g,i}}{\partial t} + \rho_g \mathbf{V} \frac{\partial C_{g,i}}{\partial x} = \frac{\partial}{\partial x} \left[\rho_g D_{ik} \frac{\partial C_{g,i}}{\partial x} \right] + \frac{MW_g}{MW_i} \frac{\dot{m}_i''}{\varepsilon} \quad (\text{B.9})$$

The large bracketed term is equal to zero because of the continuity of the exhaust gas flow. Here the assumption is that the diffusion coefficient is an isotropic property. The bulk velocity inside the channel can be expressed in terms of the pipe velocity using the integral form of the mass conservation equation written for the exhaust pipe and inside the converter.

$$\rho_p V_p A_p = \sum_{\text{channel number}} \rho_{b,x} V_{b,x} A_x$$

Since $A_{total} = \frac{A_p}{\text{number of channells}}$ we have

$$\rho_p V_p A_{total} = \rho_{b,x} V_{b,x} A_x = \rho_g V A$$

So, we have

$$V = \frac{\rho_p V_p}{\rho_g \varepsilon} \quad (\text{B.10})$$

since $\varepsilon = \frac{A}{A_{total}}$.

In the equation

$$\varepsilon \rho_g \frac{\partial C_{g,i}}{\partial t} + \rho_p V_p \frac{\partial C_{g,i}}{\partial x} = \varepsilon \rho_g D_{ik} \frac{\partial^2 C_{g,i}}{\partial x^2} + \frac{MW_g}{MW_i} \dot{m}_i'' \quad (\text{B.11})$$

we define \dot{m}_i'' , rate of volumetric molar adsorption of species i as

$$\dot{m}_i'' = k_{m,i} S (C_{s,i} - C_{g,i}) \frac{MW_i}{MW_g} \rho_g \quad (\text{B.12})$$

where $k_{m,i}$ is the particle to fluid mass transfer coefficients (m/s), S is the specific surface area, and $C_{s,i}$ is the molar fraction of the adsorbate at the monolith wall surface. Dividing each term in Equation (B.11) by ρ_g gives

$$\varepsilon \frac{\partial C_{g,i}}{\partial t} + \frac{\rho_p V_p}{\rho_g} \frac{\partial C_{g,i}}{\partial x} = \varepsilon D_{ik} \frac{\partial^2 C_{g,i}}{\partial x^2} + k_{m,i} S(C_{s,i} - C_{g,i}) \quad (\text{B.13})$$

The Material Balance for the Solid Phase of the Species i :

The species *i* disappears in the exhaust gas because of the diffusion into the catalytic wall surfaces due to adsorption. It is assumed that whatever disappears from the gas phase is consumed with the surface chemistry on the converter channel walls. Note that the gas state chemistry is ignored in our model.

$$[\dot{m}_{\text{consumed by reaction}}] = [\dot{m}_{\text{adsorbed}}] \quad (\text{B.14})$$

The adsorption term is defined as Equation (B.12).

$$MW_i a(x) \tilde{R}_i(\bar{C}_s, T_s) = \frac{MW_i}{MW_g} \rho_g k_{m,i} S(C_{g,i} - C_{s,i}) . \quad (\text{B.15})$$

Further simplification in Equation (B.15) gives

$$a(x) \tilde{R}_i(\bar{C}_s, T_s) = \frac{\rho_g}{MW_g} k_{m,i} S(C_{g,i} - C_{s,i}) . \quad (\text{B.16})$$

The Energy Equation for the Gas Phase of the Species i:

Energy balance for the control volume of the exhaust gas is derived using the heat fluxes through the perpendicular areas to the flow direction in and out of the control volume and the heat transfer from or to the surrounding monolith walls.

$$\frac{d(E_{g,cv})}{dt} = [\dot{Q}_g A]_x - [\dot{Q}_g A]_{x+\Delta x} + \dot{Q}_{gas\ to\ solid} A_{surface} \quad (B.17)$$

There is no volumetric heat generation term. The adsorption reactions are associated with the monolith walls. The radiation heat transfer is not included. An analysis similar to the analysis of the material balance for the species is done to obtain the final form of the thermal energy balance equation. After replacing expressions for

$$E_{g,cv} = m_g C_{p,g} T_g = (\rho_g \epsilon \Theta) C_{p,g} T_g,$$

$$\dot{Q}_{gas\ to\ solid} = h A_{surface} (T_s - T_g),$$

$$\text{and } \dot{Q}_g = \frac{\dot{m}_g C_{p,g} T_g}{A} = (\rho_g \epsilon v) C_{p,g} T_g$$

in Equation (B.17) and dividing by control volume $\epsilon \Theta$ and taking the limit $\Delta x \rightarrow 0$ gives

$$\frac{\partial(\rho_g C_{p,g} T_g)}{\partial t} + v \frac{\partial(\rho_g C_{p,g} T_g)}{\partial x} = h \frac{S}{\epsilon} (T_g - T_s). \quad (B.18)$$

Here, h is the inter-phase transfer coefficient, $A_{surface}$ is the circumference area, T_g , T_s are the temperatures corresponding to the gas and solid phases, and v is the exhaust gas velocity. The term $C_{p,g}$ is the specific heat for the gas. The transport of the energy between the two phases is represented by a potential temperature difference. Therefore, the last term on the right hand side also appears in the solid-phase energy balance equation. To simplify Equation (B.18) further, the derivative of each term is written in an open form. Here the specific heat coefficient $C_{p,g}$ is assumed to be a constant value:

$$C_{p,g} \left\{ \left(T_g \frac{\partial(\rho_g)}{\partial t} + \rho_g \frac{\partial(T_g)}{\partial t} \right) + v \left(T_g \frac{\partial(\rho_g)}{\partial x} + \rho_g \frac{\partial(T_g)}{\partial x} \right) \right\} = h \frac{S}{\varepsilon} (T_g - T_s) \quad (B.19)$$

The flow within a monolith channel is fully developed (see the Order of Magnitude Analysis at the end of this appendix) and therefore, the term $\frac{\partial v}{\partial x}$ is zero. So, to add this term to the left hand side of Equation (B.19) does not change the equality. After rearranging terms in Equation (B.19), we get

$$C_{p,g} \left\{ T_g \left(\frac{\partial \rho_g}{\partial t} + v \frac{\partial \rho_g}{\partial x} + \rho_g \frac{\partial v}{\partial x} \right) + \left(\rho_g \frac{\partial T_g}{\partial t} + \rho_g v \frac{\partial T_g}{\partial x} \right) \right\} = h \frac{S}{\varepsilon} (T_g - T_s) . \quad (B.20)$$

On the left hand side, the terms within the first parenthesis is the continuity equation and therefore zero. The final form of the energy balance for the gas phase becomes:

$$C_{p,g}\rho_g\left(\frac{\partial T_g}{\partial t} + v\frac{\partial T_g}{\partial x}\right) = h\frac{S}{\varepsilon}(T_g - T_s) \quad (\text{B.21})$$

The Energy Equation for the Solid Phase of the Species i :

We can write the energy balance on the channel walls. The net energy change of the walls is the result of the heat transferred by the conduction and convection and the endothermic reaction on the monolith surface.

$$\frac{d(E_{s,cv})}{dt} = \dot{Q}_s A_s|_x - \dot{Q}_s A_s|_{x+\Delta x} + \dot{Q}_{gas\ to\ solid} A_{surface} + \dot{Q}_{reaction} \Theta \quad (\text{B.22})$$

where

$$E_{s,cv} = m_s C_{p,s} T_s = \rho(1-\varepsilon)\Theta C_{p,s} T_s \quad (\text{B.23})$$

and the wall area of conduction is $A_s = (1-\varepsilon)A_{total}$.

\dot{Q}_s'' represents the rate of heat flux in W/m^2 . $\dot{Q}_{reaction}''$ represents the rate of heat release per unit volume, in W/m^3 , by the surface chemical reactions on the channel walls.

The conduction terms are defined by Fourier's conduction Law:

$$\dot{Q}_s'' \Big|_m = \lambda_m \frac{\partial T_s}{\partial m} \quad (B.24)$$

The term $(\dot{Q}_{gas\ to\ solid} A_{surface})$ is defined in page 112. Using these expressions in Equation (B.22) and dividing by the control volume, Θ , and taking the limit $\Delta x \rightarrow 0$ gives the equation

$$\frac{\partial((1-\varepsilon)\rho_s C_{p,s} T_s)}{\partial t} = (1-\varepsilon) \left\{ \lambda_x \frac{\partial^2 T_s}{\partial x^2} \right\} + hS(T_g - T_s) + a(x) \sum_{i=1}^3 (-\Delta H)_i \bar{R}_i(\bar{C}_s, T_s) \quad (B.25)$$

Here, $(1-\varepsilon)$ is the porosity coefficient representing the amount of the solid volume, ρ_s is the wall density, $C_{p,s}$ is the specific heat constant for the wall, λ_m is the conduction coefficient corresponding to direction m , $a(x)$ is the active catalytic surface area of the wall and the parameters in the last term is explained in Section 2.1.2. The wall density, ρ_s , is constant. However, the specific heat constant of the walls, $C_{p,s}$, is a function of the surface temperature distribution and therefore a function of time:

$$C_{p,s} = 1.071 + 1.56 \times 10^{-4} T_s + 3.435 \times 10^{-4} T_s^{-2} \quad (\text{B.26})$$

Using the chain rule for the time derivative term gives

$$\frac{\partial((1-\varepsilon)\rho_s C_{p,s} T_s)}{\partial t} = (1-\varepsilon) C_{p,s}^M \frac{\partial T_s}{\partial t}, \quad (\text{B.27})$$

$$\text{where } C_{p,s}^M = \left[1.071 + 2 \times 1.56 \times 10^{-4} T_s + 3.435 \times 10^{-4} T_s^{-2} \right]. \quad (\text{B.28})$$

The final form of the energy balance for the solid phase becomes

$$(1-\varepsilon)\rho_s C_{p,s}^M \frac{\partial(T_s)}{\partial t} = (1-\varepsilon) \left\{ \lambda_x \frac{\partial^2 T_s}{\partial x^2} \right\} + hS(T_g - T_s) + a(x) \sum_{i=1}^3 (-\Delta H)_i \tilde{R}_i(\bar{C}_s, T_s). \quad (\text{B.29})$$

In the calculations of the present study, the results show that the overall effect of having constant or the variable $C_{p,s}$ is not very significant.

The Dimensionless Form Of The Balance Equations:

In this section, dimensionless form of the balance equations are derived. These forms of the equations are going to be used for the order of magnitude analysis and calculations. The characteristic values used for the non-dimensional form are defined as follows. The converter length L , the radius R_h , the velocity v , time $\frac{L}{v}$, the inlet gas concentration of species i , $C_{g,i}^{inlet}$, and the inlet gas

temperature T_g^{inlet} . Each term in Equation (B.13) is non-dimensionalised by the characteristic values described above. The dimensionless form of the mass balance equations for the gas-phase of the species i becomes

$$\frac{C_{g,i}^{inlet} \partial \check{C}_{g,i}}{t_c \partial \check{t}} + v \frac{C_{g,i}^{inlet} \partial \check{C}_{g,i}}{L \partial \check{x}} = D_{ik} C_{g,i}^{inlet} \frac{\partial^2 \check{C}_{g,i}}{L^2 \partial \check{x}^2} + k_{m,i} \frac{S}{\varepsilon} (\check{C}_{s,i} - \check{C}_{g,i}) C_{g,i}^{inlet} \quad (B.31)$$

Simplifying the above equations using the expressions for S and $k_{m,i}$, we obtain

$$\frac{\partial \check{C}_{g,i}}{\partial \check{t}} + \frac{v t_c}{L} \frac{\partial \check{C}_{g,i}}{\partial \check{x}} = \frac{t_c D_{ik}}{L^2} \frac{\partial^2 \check{C}_{g,i}}{\partial \check{x}^2} + \frac{Sh_{\infty} t_c D_{ik}}{R_h^2} (\check{C}_{s,i} - \check{C}_{g,i})$$

The mass balance equation for the solid phase equation, Equation (B.16), is simplified using the same characteristic parameters to get

$$a(x) L \tilde{R}_{co}(\bar{C}_s, T_s) \frac{\tilde{R}_i(\bar{C}_s, T_s)}{\tilde{R}_{co}(\bar{C}_s, T_s)} = \frac{\rho_g}{MW_g} k_{m,i} SL (C_{g,i} - C_{s,i}) \quad (B.32)$$

$$\check{a}(x) \tilde{R}_{co}(\bar{C}_s, T_s) \tilde{R}_i(\check{\bar{C}}_s, \check{T}_s) = \frac{\rho_g}{MW_g} k_{m,i} SL C_{g,i}^{inlet} (\check{C}_{g,i} - \check{C}_{s,i}) \quad (B.33)$$

The energy balance for the gas phase equation, Equation (B.21), becomes

$$C_{p,g} \rho_g \left(\frac{\partial \check{T}_g}{t_c \partial \check{t}} + \frac{v}{L} \frac{\partial \check{T}_g}{\partial \check{x}} \right) = h \frac{S}{\varepsilon} (\check{T}_g - \check{T}_s) \quad (B.34)$$

$$\frac{\partial \tilde{T}_g}{\partial \tilde{t}} + \frac{v t_c}{L} \frac{\partial \tilde{T}_g}{\partial \tilde{x}} = \frac{h St_c}{\epsilon C_{p,g} \rho_g} (\tilde{T}_g - \tilde{T}_s) \quad (\text{B.35})$$

By a similar analysis of the energy balance equation for solid phase, Equation (B.29) gives

$$\rho_s C_{p,s}^M \frac{T_g^{inlet} \partial \tilde{T}_s}{t_c \partial \tilde{t}} = \left\{ \frac{\lambda_x T_g^{inlet}}{L^2} \frac{\partial^2 \tilde{T}_s}{\partial \tilde{x}^2} \right\} + \frac{h S}{(1-\epsilon)} T_g^{inlet} (\tilde{T}_g - \tilde{T}_s) + \frac{a(x)}{(1-\epsilon)} \sum_{i=1}^3 (-\Delta H)_i \tilde{R}_i(\bar{C}_s, T_s) \quad (\text{B.36})$$

The Order Of Magnitude Analysis

The order of magnitude analysis is necessary to be able to make some simplifications over the equation set we have. Schema B.1 shows the directions, control volumes and surfaces for this problem.

From Equation (B.13)), the mass balance equation in general form is

$$\begin{aligned} \frac{\partial C_{g,i}}{\partial t} + \left(u \frac{\partial C_{g,i}}{\partial x} + v \frac{\partial C_{g,i}}{\partial y} + w \frac{\partial C_{g,i}}{\partial z} \right) &= D_{ik} \left(\frac{\partial^2 C_{g,i}}{\partial x^2} + \frac{\partial^2 C_{g,i}}{\partial y^2} + \frac{\partial^2 C_{g,i}}{\partial z^2} \right) \\ &+ k_{m,i} \frac{S}{\epsilon} (C_{s,i} - C_{g,i}) \end{aligned} \quad (\text{B.37})$$

In order to check the order of magnitude of each term, the equation is re-written in form

$$\frac{C_{g,j}}{\Delta t}; u \frac{C_{g,j}}{\Delta x}; v \frac{C_{g,j}}{\Delta y}; w \frac{C_{g,j}}{\Delta z} = D_{ik} \left(\frac{C_{g,j}}{\Delta x^2}; \frac{C_{g,j}}{\Delta y^2}; \frac{C_{g,j}}{\Delta z^2} \right) ; k_{m,j} \frac{S}{\varepsilon} (C_{s,j} - C_{g,j}) \quad (\text{B.38})$$

Divide each term by $C_{g,j}$ to get

$$\frac{1}{\Delta t}; \frac{u}{\Delta x}; \frac{v}{\Delta y}; \frac{w}{\Delta z} = D_{ik} \left(\frac{1}{\Delta x^2}; \frac{1}{\Delta y^2}; \frac{1}{\Delta z^2} \right) ; k_{m,j} \frac{S}{\varepsilon} \left(\frac{C_{s,j}}{C_{g,j}} - 1 \right) \quad (\text{B.39})$$

For the Poiseuille flow through ducts, study of Shah and London [1971] shows that regardless of the duct shape, the entrance length can be correlated by the following expression:

$$\frac{L_{\text{entrance}}}{D_h} \approx 0.5 + .005 Re_{D_h} \quad (\text{B.40})$$

The nominal values for the velocity in the channel is around 10 m/s and the diameter of the channel is around 0.0606cm. With these values, typical Reynolds Number is around 120 and the entrance length for this flow is

$$L_{\text{entrance}} = 1.1 \times D_h = 0.066 \text{ cm} .$$

Since the transition to turbulence occurs at about $Re \approx 2300$, the type of the flow in this study is laminar and fully developed for $x > L_{\text{entrance}}$. The velocity becomes purely axial, that is $v = w = 0$.

$$\frac{1}{\Delta t}; \frac{u}{\Delta x} = D_{ik} \left(\frac{1}{\Delta x^2}; \frac{1}{\Delta y^2}; \frac{1}{\Delta z^2} \right) ; k_{m,j} \frac{S}{\varepsilon} \left(\frac{C_{s,j}}{C_{g,j}} - 1 \right) \quad (\text{B.41})$$

The order of magnitude of D_{ik} is around 10^{-4} . The mass diffusivity coefficient between the bulk gas stream and the catalyst surface is estimated from the Sherwood number for fully developed laminar flow with constant wall heat flux in the monolith channel (Shah [1971]):

$$k_{m,j} = \frac{Sh_{\infty} D_i}{2 \times R_h} \approx \frac{3.}{2 \times .0606 \times 10^{-2}} D_i \approx 2475 D_i [m/s] \quad (B.42)$$

The geometric surface; $\frac{S}{\epsilon} = \frac{2}{R_h} \approx 3300 m^{-1}$, therefore the last term on the right side, becomes a number around 800. If we check the magnitude of each term, depending on their nominal values given in Table B.1, some terms can be neglected for the purpose of simplification. The simplified version of the species conservation equation reduces to

$$u \frac{\partial C_{g,j}}{\partial x} = k_{m,j} \frac{S}{\epsilon} (C_{s,j} - C_{g,j}) \quad (B.43)$$

Here, the storage term and the diffusion of the species along the axial and other directions are neglected. The convection term is balanced with the inter-phase material balance.

Table B.1 Nominal values for the order of magnitude analysis

$C_{g,i}$	$C_{s,i}$	u (m/s)	$\Delta x, \Delta y, \Delta z$ (m)	Δt	$D_{ik} \times 10^4$ (m ² /s)
0.0004 5 .02	0.00045 .02	10	N=243 .000413sq1.7d- 7 N=81 .00125sq1.5d-6	.01	.0895-5.186



$\frac{1}{\Delta t}$	$\frac{u}{\Delta x}$	$\frac{D_{ik}}{(\Delta x)^2}$	$k_{m,i} \frac{S}{\varepsilon}$
≈ 100	$\approx 8000 - 24200$	$\approx 64 \times 10^4 D_{ik}$ ≈ 64	$\approx 816.75 \times 10^4 D_{ik}$ $\approx 816 \left(\frac{C_{s,i}}{C_{g,i}} \right)$

BIBLIOGRAPHY

1. Ball, D. J. [1992] "Distribution of Warm-Up and Under-floor Catalyst Volumes," SAE Paper No. 922338.
2. Baruah, P.C., Benson, R.S and Gupta, H.N. [1978] "Performance and emissions predictions for a multi-cylinder spark ignition engine with catalytic converter," SAE Paper 780672.
3. Bejan, A. [1984] Convection Heat Transfer, John Wiley & Sons, New York
4. Bella, G., Rocco, V., Maggiore, M., Stella, F. and Succi, F. [1991] "Automotive catalytic converter performance evaluation: a computational approach," ATA Ingegneria Automotoristica, Vol. 44, pp.242.
5. Benjamin, S. F., Clarkson, R. J., Haimad, N. and Girgis, N. S. [1996] "An experimental and predictive study of the flow field in axisymmetric automotive exhaust catalyst systems," SAE Paper 961208.
6. Benjamin, S. F., Roberts, C.A. [2000] "Warm up of an automotive catalyst substrate by pulsating flow: a single channel modeling approach," International Journal of Heat and Fluid Flow, Vol 21.
7. Bird, R. B., Stewart, W. E. and Lightfoot, E. N. [1960] "Transport Phenomena," John Willey, New York, pp505.
8. Burch, D.S. and Biel, J.P. [1999] "SULEV and off-cycle emissions benefits of a vacuum-insulated catalytic converter," SAE Paper 1999-01-0461.
9. Byrne, H. and Norbury, J [1994] "Stable Solutions for Catalytic Converter," SIAM J.Appl. Math, Vol 54, No3, pp.789-813.

10. Bissett, E.J. and Oh, S.H. [1999] "Electrically heated converters for automotive emission control: determination of the best size regime for the heated element," Chemical Engineering Science, 54, pp 3957-3966.
11. Chen, D. K. S. [1993] "A Numerical Model for Thermal Problem in Exhaust Systems," Vehicle Thermal Management Systems Conference, Columbus, OH.
12. Chen, D. K. S., Bissett, E. J., Oh, S. H., and van Ostrom D. L. [1988] "A three-dimensional model for the analysis of transient thermal and conversion characteristics on monolithic catalytic converters," SAE Paper 880282.
13. Clarkson, J.R. [1995] "A theoretical and experimental study of automotive catalytic converters," PhD thesis, Coventry University, UK.
14. Cundari, D. and Nuti, M. [1991] "A One-Dimensional Model for Monolithic Converter: Numerical Simulation and Experimental Verification of Conversion and Thermal Responses for Two-Stroke Engine," Piaggio V.E. S.p.A. Res&Devpt., 910668.
15. Day, J.P., and Socha, L.S [1991], "The design of automotive catalyst supports for improved pressure drop and conversion efficiency," SAE Paper 910371
16. Dulieu, C.A, Evans, W.D,J., Larbey, R.J., Verrall, A.M., Wilkins, A.J.J. and Povey, J.H. [1977] "Metal supported catalysts for automotive applications," SAE Paper 770299
17. Engler, B. H. et al. [1993] "Reduction of Exhaust Gas Emissions by Using Hydrocarbon Adsorber Systems," SAE Paper No. 930738.

18. Flytzani-Stephanopoulos, M., Voecks, G. E. and Charrng, T. [1986] "Modelling of heat transfer in nonadiabatic monolith reactors and experimental comparisons of metal monoliths with packed beds," Chem. Eng. Sci., Vol. 41, pp.1203.
19. Heck, R. H., Wei, J. and Katzer, J. R. [1976] "Mathematical modeling of automotive catalysts," AIChE J. Vol. 22, pp.477
20. Hegedus, L.L., Oh, S.H. and Baron, K. [1977] "Multiple Steady States in an isothermal integral reactor : The catalytic oxidation of Carbon monoxide over platinum-alumina," A.I.Ch.J., 23 pp.632-642.
21. Heimrich, M. J. et al. [1991] "Electrically-Heated Catalysts for Cold-Start Emission Control on Gasoline and Methanol-Fueled Vehicles," ICE-Vol. 15, Fuels, Controls and After-treatment for Low Emissions Engines, ASME.
22. Hellman, K. H. et al. [1991] "Evaluation of Different Resistively Heated Catalyst Technology," SAE Paper No. 912382.
23. Hellman, K.H., Bruetsch, R. and Tallent, W. [1989] "Resistive Materials Applied to Quick Light off Catalyst," SAE Paper 890799.
24. Jasper, T.S., Robinson, K. and Cuttler, D.H. [1991] "Substrate effects on catalyst light off: Their influence on catalyst design and performance," Worldwide Engine Emissions Standards and How to Meet Them, ImechE Seminar.
25. Jeong, S. and Kim T. [1997] "CFD Investigation of the 3-Dimensional Unsteady Flow in the Catalytic Converter," SAE paper No:971025.
26. Kaiser, F.W. and Pelters, S. [1991] "Comparison of metal supported

catalyst with different cell geometries," SAE Paper 910837.

27. Kim, J.Y., Lai, M.C., Li, P., and Chui, G. [1992] "Modeling diffuser monolith flows and its implications to automotive catalytic converter internal flow," SAE Paper 921093.
28. Kuo, J.C.W., Morgan, C.R. and Lassen, H.G. [1971] "Mathematical modeling of CO and HC catalytic converter systems," SAE Paper 710289.
29. Kummer, J.T. [1980] "Catalysts for automobile emission control," Proc. Energy Combust. Sci., Vol. 6.
30. Lacin F. and Zhuang, M. [2000] "Modeling and Simulation of Transient Thermal and Conversion Characteristics for Catalytic Converters," SAE 2000-01-0209.
31. Lacin, F. and Zhuang, M. [2001] "Catalytic Converter and Method of Use Thereof," Provisional Patent Application, Nov. 7.
32. Lai, M.-C., Kim, J.-Y., Cheng, C.-Y., Chui, G. and Pakko, J. D. [1991] "Three-dimensional simulations of automotive catalytic converter internal flow," SAE Paper 910200.
33. Lee, S.T. and Aris, R. [1977] "On the effect of radiative heat transfer in monoliths," Chem. Eng. Sci., Vol.32, pp827-837.
34. Lemme, J. S., Givens, W. R. and Sekella, T. C. [1974] "Flow through catalytic converters -- An analytic and experimental treatment," SAE Paper 740243.
35. Li, P., Chui, G. and Pakko, J. D. [1991] "A numerical study of automotive catalytic converter internal flow," the 4th International PHOENICS User

Conference, CHAM Ed., pp.189.

36. Matkowsky, B.J. and Sivashinsky, G.I. [1979] "An asymptotic Derivation of Two Models in Flame Theory Associated with the Constant Density Approximation," SIAM J.Appl. Math, Vol 37, No3, pp.686-699.
37. Mondt, J. R. [1993] "Exhaust After-treatment Subsystems," The Challenge of Future Passenger Car Emissions Standards TOPTEC, Society of Automotive Engineers, Warrendale Pa.,
38. Moore, W. R. and Mondt, J. R. [1993] "Predicted Cold Start Emission Reductions Resulting from Exhaust Thermal Energy Conservation to Quicken Catalytic Converter Light-off," SAE Paper No. 931087.
39. Nishizawa, K., Masuda, K., Horie, H. and Hirohashi, J. [1989] "Development of improved metal supported catalyst ", SAE Paper 890188
40. Nonnenmann, M. 1990] "New high performance gas flow equalizing metal supports for automotive exhaust gas catalyst, " SAE Paper 900270.
41. Nonnenmann, M. [1985] "Metal supports for exhaust gas catalysts," SAE Paper 850131.
42. Oh, S. H. and Cavendish, J. C. [1982] "Transients of Monolithic Catalytic Converters: Response to a Step Change in Free-stream Temperature as Related to Controlling Automobile Emission," *Ind. Eng. Chem. Prod. Res. Dev.*, Vol. 21, pp.29-37.
43. Petzold, L. [1983] "Automatic selection of methods for solving stiff and non-stiff systems of ordinary differential equations," SIAM, Sci. Stat. Comput., Vol4, No1.

44. Psyllos, A. and Philippopoulos, C. [1992] "Modeling of monolith catalytic converters used in automotive pollution control," *Appl. Math. Modeling*, Vol,16, pp484.
45. Schweich, D., and Leclerc, J.P [1990] "Flow, heat and mass transfer in a monolithic catalytic converter," 2nd International Conference on Catalyst and Automotive Pollution Control, Brussels.
46. Schweich, D. [1995] "Laboratory data for three-way catalytic converter modeling," *Catalysis and Automotive Pollution Control III* Vol. 96, pp.55.
47. Shah, R.K. and London, A. L. [1971] "Laminar Flow Forced Convection Heat Transfer and Flow Friction in a Straight and Curved Ducts-A summary of Analytical Solutions," Technical Report No.75, Department of Mechanical Engineering Stanford University, Stanford, CA.
48. Shen, H., Shamim, T. and Sengupta, S. [1999] "Performance Analysis and Design Optimization of Catalytic Converters," proceedings of the 36th Heat Transfer and Fluid Mechanics Institute, pp. 133-143.
49. Sherony, D.F. and Solbrig, C.W. [1970] "Analytical Investigation of Heat and Mass Transfer Friction Factors in a Corrugated Duct Heat or Mass Exchanger," *Int. J. Heat Mass Transfer*, 13, p1455.
50. Siemund, S., Schweich, D., Leclerc, J. P. and Villermaux, J. [1995] "Modeling three-way monolithic catalytic converter: comparison between simulation and experimental data," *Catalysis and Automotive Pollution Control III* Vol. 96, pp.887.
51. Subramanian, B. and Arma, A. [1985] "Reaction kinetics on a commercial three-way catalyst: the CO-NO-O₂-H₂O system," *Ind. Eng. Chem. Prod. Res. Dev.*, Vol. 24, pp. 512-516.

52. Subramanian, B. and Varma, A. [1984] "Reactions of CO , NO , O_2 and H_2O on three-way and Pt/Al_2O_3 catalysts," *Frontiers in chemical engineering, Proceedings of the International Chemical Engineering Conference*, 1, pp.231.
53. Terres, F. et al. [1996] "Electrically Heated Catalyst-Design and Operation Requirements," SAE Paper No. 961137.
54. Voltz, S. E., Morgan, C. R., Liederman, D. and Jacob, S. M. [1973] "Kinetic study of carbon monoxide and propylene oxidation on platinum catalysts," *Ind. Eng. Chem. Proc. Res. Dev.*, Vol 12, pp.295.
55. Weltens, H. Bressler, H., Terres, F., Neumaier, H. and Rammoser, D. [1993] "Optimization of catalytic converter gas flow distribution by CFD predictions," SAE Paper 930780.
56. Wendland, D. W., [1993] "Automobile Exhaust-System Steady-State Heat Transfer," SAE Paper No. 931085.
57. Wendland, D. W., and Matthes, W.R. [1986] "Visualization of automotive catalytic converter internal flows," SAE Paper No. 861554.
58. Wendland, D.W., Matthes, W.R., and Sorrell, P.L [1992] "Effect of header truncation on monolith converter emission control performance," SAE Paper 912372.
59. Wendland, D.W., Sorrell, P.L. and Kreucher, J.E [1991] "Sources of monolith catalytic converter pressure loss," SAE Paper 912372.
60. Whittenberger, W.A, Kubsh, J.E. [1990] "Recent Development in Electrically Heated Metal Monoliths," SAE Paper 900503.

61. Yamamoto, H., Kato, F., Kitagawa, J. and Machida, M., [1991] "Warm-up characteristics of thin wall honeycomb catalysts," SAE Paper 9110611.
62. Jeong, S. and Kim, T. [1997] "CFD investigation of the 3-Dimensional Unsteady Flow in the Catalytic Converter," SAE Paper 971025.

MICHIGAN STATE UNIVERSITY LIBRARIES



3 1293 02327 0972